Università degli Studi di Milano - Bicocca
Scuola di Dottorato
Department of Materials Science

Doctorate in Materials Science and Nanotechnology XXXI cycle

Modeling of 3D heteroepitaxial structures by continuum approaches

Doctorate Thesis of:

Marco Albani

Tutor:

Prof. Leonida Miglio

Registration number:

736650

Coordinator:

Prof. Marco Bernasconi

Academic year 2017/2018

Contents

Introduction **5**

1 Semiconductor heteroepitaxy **9**

1.1 Heteroepitaxial growth on planar substrates 9

1.1.1 Growth modalities 10

1.1.2 Growth techniques 12

1.1.3 Ge/Si prototypical system for SK growth 13

1.1.4 An analytical model for island growth: the ATG instability 14

1.1.5 Technological applications 15

1.2 Heteroepitaxy in nanowire structures 16

1.2.1 The vapour-liquid-solid technique 17

1.2.2 Core/shell structure 18

1.3 Selective area epitaxy 19

2 Modeling the kinetic crystal growth **21**

2.1 Introduction to crystal faceting 21

2.2 Continuum modeling of kinetic growth by phase-field 24

2.2.1 Faceting by orientation dependent incorporation dynamics 28

2.2.2 Competing regimes driving the crystal faceting 32

2.2.3 Applications to pillared structures 35

2.3 Modeling the kinetic growth of vertical nanomembranes 37

2.3.1 Introduction to SAE growth of GaAs nanomembranes 37

2.3.2 Experimental details 39

2.3.3 Kinetic model details 39

2.3.4 Simulation results and comparison with experiments 42

2.4 Conclusions 53

3 Elasticity in core/shell nanowires by finite element method **55**

3.1 Continuum elasticity for semiconductor heteroepitaxy 55

3.1.1 Mechanical equilibrium 59

3.2 Finite element method 60

3.2.1 Weak formulation 60

3.2.2 Galerkin method 61

4 Bending in core/shell GaP/InGaP wurtzite nanowires **63**
4.1 Introduction 63
4.2 Experimental 65
4.2.1 Materials and methods 65
4.2.2 SEM, TEM and EDX characterization 65
4.3 Elastic continuum predictions 68
4.3.1 Modeling core/shell nanowire bending 69
4.3.2 Comparison between simulations and experiments 70
4.3.3 Comprehensive analysis of nanowire bending 71
4.4 Conclusions 75

5 Elastic strain relaxation in Ge/GeSn core/shell nanowires **77**
5.1 Introduction 77
5.2 GeSn growth issues 79
5.2.1 Equilibrium solubility of Sn 79
5.2.2 Ge/GeSn core shell nanowires: experimental details 79
5.3 Strain tunability by core/shell nanowires 80
5.4 Core diameter and strain relaxation 87
5.5 Conclusions 90

6 Heteroepitaxial growth of islands on patterned substrates **91**
6.1 Introduction 91
6.2 Phase-field model for island growth 93
6.2.1 Wetting energy and critical thickness 98
6.2.2 Computational details 100
6.3 Results and discussion 100
6.3.1 Island growth into the pit 100
6.3.2 The role of the growth conditions 104
6.3.3 Pattern geometry 108
6.3.4 Material properties 110
6.3.5 3D simulation results 113
6.4 Island stacking 114
6.5 Conclusions 117

Conclusions **119**

List of publications **123**

Acronyms **124**

Acknowledgements **125**

Bibliography **127**

Introduction

Semiconductors are the main building block for a variety of devices in our life. The semiconductor industry, in the last decades, has evolved by following the Moore's law [1]. According to that, the improvements in performances and functionality have been enabled by a continuos miniaturization process of the building blocks of the devices. This goal has been achieved basically due to the refinement of the fabrication processes, thanks to the improvement of patterning and lithographic techniques that nowadays can control the top-down formation of nanostructures even below 10nm in size [2]. However, this incredible innovation process is going to reach an end in the next years, as the miniaturization is getting too close to the atomistic size [3], which hinders the development of smaller devices. Therefore, alternative ways to evolve the current technologies have to be exploited [4]. In particular, since the size cannot play any more a major role, the interest of the scientific and industrial research is for three-dimensional heterostructures, such as FinFETs, gate-all-around or vertical transistors [5, 6]. The 3D character of these structures allows to introduce novel properties, which depend for instance on the high surface-to-volume ratio, on the possibility to induce or relax strain on a micro- or nano-scale, on local fluctuations of alloy composition or on quantum confinement effects. Nanowires [7] are the most representative example as, thanks to their peculiar one-dimensional shape, they enable a huge variety of applications, ranging from electronic, to optoelectronic, to the integration in biological systems.

Bottom-up approaches are currently being studied for the growth of 3D nanostructures. Indeed, if compared to top-down techniques, they allow for the development of more regular surfaces, with a lower defectivity. This becomes of crucial importance when the ratio between surface and volume is strongly unbalanced toward the former, and for instance it can enable peculiar transport phenomena, as for the quasi-ballistic phonon transport [8]. However, this approach makes the growth of 3D nanostructures extremely challenging. Indeed, it is reasonable to assume that a structure that develops with a high surface-to-volume ratio is unstable on an energetic point of view, essentially due to the high surface energy cost. Moreover, the control of the growth direction is no more set by the substrate orientation, as for planar growth, but may be influenced by several conditions.

In this Thesis, to deal with the complex 3D growth dynamics, we develop a modeling technique that can reproduce and interpret the vertical growth of nanostructures [9]. This first involves the exploitation of a peculiar modeling which can tackle both thermodynamic and kinetic contributions. In the literature, the main approach used to simulate the epitaxial growth of semiconductors relies on thermodynamic arguments [10, 11]. In particular, the

evolution of the structures at a nano- and micro-scale is considered to be determined by the redistribution of adatoms on the surface. This dynamics, often modeled as a surface diffusion process, is driven by the thermodynamic principle of free energy minimization [12, 13]. The free energy of the system, in a first approximation, is given by the surface energy. This is generally orientation dependent, and therefore tends to drive the formation of faceted crystals, which minimize both the surface area exposed, as weighted by the surface energy density corresponding to each facet of the crystal. This is the most used model to interpret the growth dynamics of crystals at a nano- and micro-scale and is well represented by the geometrical theory developed by Wulff [14]. However, as we will explicitly show in this Thesis, this interpretation of the growth dynamics does not apply to the development of vertical nanostructures. Indeed, intuitively, the thermodynamic approach tends to favor the formation of structures with a low surface-to-volume ratio, in order to minimize the cost of the dangling bonds at the surface. Therefore, a new approach, that we will identify as kinetic, has to be adopted to model the peculiar growth of 3D nanostructures. In the literature [15, 16], the kinetic regime has been already studied with respect to the growth of semiconductor crystals. The advancement that we introduce is the possibility to combine kinetic and thermodynamic contributions to study an intermediate growth regime, which is necessary for the simulation of vertical nanomembranes and 3D fin-like structures in general.

The simulation of the vertical growth is not just challenging for the identification of a proper model, but it requires also a dedicated approach for the numerical solution of the evolution dynamics. Indeed, when dealing with crystal morphologies which develop vertically with respect to the substrate surface, an implicit description [10] of the system geometry has proved to be very effective, with respect to standard explicit approaches where the surface profile is traced by means of a function. In particular, in this Thesis, we exploit a phase field (PF) model to simulate the growth on GaAs nanomembranes, based on a finite element method for the solution of the evolution equations. The phase-field description consists in a continuous function φ, that is used to distinguish between the solid ($\varphi = 1$) and the vacuum ($\varphi = 0$). The surface between them is therefore represented by an interface region, where φ goes smoothly form 1 to 0. The PF model is simulated thanks to the AMDiS C++ toolbox [17, 18], which includes the description of the function φ on a mesh, that is needed by the FEM approach. A peculiar feature of AMDiS is the possibility to use an adaptive mesh, instead of a uniform grid. This allows to increase the mesh definition only where it is needed by the evolution problem, resulting in a computational performance improvement. Another strong advantage of this phase-field approach is the possibility to handle real 3D simulations, a features which is highly welcomed when the aim is to simulate 3D nanostructures in a reliable way.

For the development of devices, it is often required to build heterostructures which combine different semiconductors, for instance for optoelectronic applications where a p-n junction is required [19]. Furthermore, the heteroepitaxial growth can be exploited also to transfer some structural material properties, such as the hexagonal lattice structure, from a material to another [20]. These possibilities are particularly exploited in core/shell nanowires. These consist in the growth of a nanowire, made of a single material and identified as "core",

by dedicated growth techniques as the vapor-liquid-solid or the selective area epitaxy [21]. Then, a second growth step is performed by depositing a second type of semiconductor all around, obtaining by heteroepitaxy a film with a cylindrical symmetry called "shell".

The heteroepitaxial growth, both on planar substrates and on 3D nanostrucutres, can lead to elastic deformations in the crystal lattice [22]. This occurs due to the different bulk lattice parameter of the materials involved in the growth. As a result, as it has been widely studied for planar film growth, the lattice structure is deformed in order to accommodate the lattice mismatch, or a plastic relaxation is achieved through defects, which are usually detrimental for the applications. In this Thesis, we focus on the core/shell nanowire system and we provide a detailed characterization of the strain relaxation mechanisms. In particular, we study the bending of GaP/InGaP nanowires and we correlate this phenomenon with the partitioning of the elastic deformation within the nanostructure. Moreover, we investigate the role of the elastic relaxation in Ge/GeSn core/shell nanowires. In this latter case, the role of Sn composition in the alloy is fundamental for the opto-electronic applications. Therefore we study which is the impact of strain relaxation in the incorporation of Sn atoms, going beyond the equilibrium solubility limit for the GeSn alloy. The elastic relaxation is studied by a continuum elasticity approach, profiting of numerical solution for the strain distribution performed by finite element method, which can handle the simulation of the 3D structure, improving the reliability of the elastic analysis

The evolution of nanostructures can be driven also by the combined effect of surface energy and elastic energy contributions [23, 24]. One of the most studied examples of this is the heteroepitaxial growth of islands on planar substrates. Since the first analytical model by Asaro-Tiller-Grinfeld [25, 26] and Srolovitz [27], it is known that when a semiconductor is deposited on a substrate with a different lattice parameter, the growth dynamics can deviate from the simple flat geometry leading to the growth of 3D structures, which enable an enhanced strain relaxation with respect to the flat configuration, still by minimizing the surface energy cost of the system. For technological applications it is fundamental to control the spatial distribution and the size-uniformity of the islands, for instance to exploit them as quantum dots for optoelectonics applications. To this purpose, in the literature several approaches have been investigated by theory and experiments [28–31]. However, a comprehensive understanding of the role of the growth conditions in ordering the growth is still missing.

In this Thesis, we propose a phase-field model which combines the description for the surface diffusion dynamics and the finite element characterization of the strain field [32] to study the ordered growth of islands. In particular, we choose the prototypical system where Ge islands are grown on a Si substrate and we focus on two different ordering techniques: the growth on a pit-patterned substrate and the vertical stacking of islands. The advantage of the phase-field model based on finite element method is the possibility to exactly solve the evolution equations of the system, without the need of higher order approximations and with the possibility to precisely consider the effect on the elastic relaxation which is provided by the substrate morphology.

The Thesis is organized as follows. In Chapter 1 we provide a general overview of the

heteroepitaxial systems and growth techniques that we are going to consider in the following chapters. In Chapter 2, we present the phase-field model that we have developed, which includes the kinetic contributions required to simulate the vertical growth of nanostructures and represents a significative advancement with respect to the existing literature models. After an initial discussion of the main features of the kinetic growth regime, we apply the modeling to the study of the growth of GaAs 3D fins, by investigating the material properties and the growth parameter in close comparison with the experimental evidences. In Chapter 3, we describe the static continuum model which is used to simulate the elastic relaxation in core/shell nanowires. The first application of this model is presented in Chapter 4 for the study of the bending of core/shell GaP/InGaP nanowires. Then, in Chapter 5, we focus on the original characterization of Ge/GeSn nanowires, investigating for the first time in the literature the possible correlation between strain relaxation and Sn incorporation in nanowire structures. In Chapter 6 we present our implementation of the phase-field model for surface diffusion to include also the elastic energy calculations. This enables the study of the heteroepitaxial growth of islands first on pit-patterned substrates and then in vertically stacked arrays. Finally, the conclusions of the results obtained in this Thesis are drawn.

Chapter 1

Semiconductor heteroepitaxy

Semiconductors represent nowadays a class of material with a variety of applications. First of all, they are the basis of the common electronic devices, but are also fundamental for solar energy applications and solid state lightning. The most peculiar property of semiconductor is that, differently from metals, their band structure has an energy gap between the valence and conduction levels. This gap ranges from fractions of eV of to 5-7 eV, above which the materials are classified as insulators. By exploiting specific techniques, such as doping, heterointegration and alloying a variety of features can be developed, enabling a large set of different applications. Nowadays, however, we are reaching the limit of the Moore's law [1], which states that the innovation of the electronics is due to the miniaturization process. Therefore, new technologies have to be developed, enabling a further improvement of the semiconductor exploitation, profiting for instance of new degrees of freedom in engineering new devices, as it is for the case of three-dimensional structures.

1.1 Heteroepitaxial growth on planar substrates

Epitaxy refers to the growth of a mono-crystalline film on a mono-crystalline substrate. Heteroepitaxy is a specific kind of epitaxy, where the material composing the film is different from the one of the substrate. In particular, the main property that characterizes the heteroepitaxy is the lattice parameter of the crystal structures involved in the growth.

In a general picture of the system, the profile evolution is due to the motion of the surface atoms. This can occur in two main conditions: deposition, where the number of atoms on the film continuously increases, and annealing, in which there is no additional material supply and the surface atoms, thanks to the high temperature of this process, can rearrange, lowering the energy of the system. Adatoms on the surface can move in two separate ways: by exchanging with the surrounding environment or by diffusing on the surface. In this Thesis, we will focus on this latter mechanisms, presenting different models for the surface diffusion dynamics.

1.1.1 Growth modalities

The different structural properties between the materials involved in the heteroepitaxial growth can produce various growth modes. To give an interpretation, based on the thermodynamics principles, for the different modalities, it is possible to focus on two main properties: the surface energy densities and the difference between the lattice parameters (lattice mismatch). The former quantifies the energy cost to create a unit surface, considering both the orientation and the reconstruction of the surface. The latter determines the elastic energy cost required to accommodate (by an expansion or a compression) the lattice parameter of the film to the one of the substrate, in order to achieve a pseudomorphic growth.

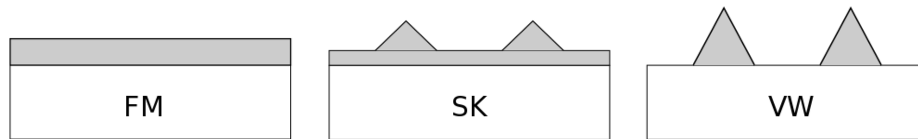

Figure 1.1: Scheme for the growth modalities in an heteroepitaxial system. FW describes the Franck-van der Merwe modality, with the wetting layer formation, but with no island. SK shows the Stranki-Krastanow case, where it is possible to observe both a wetting layer and the islands. VW represents the Volmer-Weber growth, in which islands grow without any wetting layer. Colors distinguish between the two different materials.

There are three main growth modes that can be distinguished in heteroepitaxy [33, 34]: the Frank-van der Merwe (FM) [35], the Stranski-Krastanov (SK) [36] and the Volmer-Weber (VW) [37].

Frank - van der Merwe

The FM growth is characterized by a 2D layer-by-layer arrangement of atoms above the substrate surface. This condition is driven by a specific balance between the surface energies of the system. If γ_{film} is the surface energy density for the deposited material, γ_{sub} the one for the substrate and γ_{int} the one for the film/substrate interface, it is possible to deduce the energetic condition that favors a FM growth. Indeed if $\gamma_{film} + \gamma_{inf} < \gamma_{sub}$ it means that, in order to minimize the surface energy, the system tends to cover the substrate surface by a flat layer made by the deposited atoms. This allows to lower the surface energy density of the system by changing the energy cost to expose a unit surface from the value of γ_{sub} to $\gamma_{film} + \gamma_{int}$. The free surface remains flat, as this is the optimal condition to minimize the exposed area.

From the elastic point of view, a relatively low lattice mismatch ($< 2\%$) is required. This means that the elastic energy stored by the system is not high enough to change the dynamics of the growth, which is essentially driven by the minimization of the surface energy. Nevertheless the elastic energy stored in the film could lead to the formation of defects, as for example misfit dislocations at the film/substrate interface, in order to accommodate the lattice mismatch between the two material. This occurs if the energy required to generate a defect is compensated by the elastic relaxation provided by the defect. In this case the

growth is no more pseudomorphic.

Volmer - Weber

The VW modality is characterized by a 3D growth. The deposited material does not cover the entire surface of the substrate, but generates from the very beginning some isolated islands on the surface. This behavior could be explained again in terms of surface energy densities. Indeed, if $\gamma_{film}+\gamma_{int} > \gamma_{sub}$ it is energetically more favorable to keep the substrate surface uncovered. This justifies why, in the VW mode, the deposited material doesn't cover the entire substrate surface, but it rearranges into isolated islands. The shape of these islands is then driven by the minimization of the surface and interfacial energies.

Moreover, VW growth can be promoted also by an elastic relaxation mechanism. If the lattice mismatch is relatively high ($> 8\%$), the formation of a flat layer above the substrate can't provide an efficient relaxation of the elastic energy. Indeed the in-plane directions, which are parallel to the substrate plane, would have a compression equal to the lattice mismatch, while the only relaxation could act tetragonally toward the free surface. On the contrary, islands efficiently enhance the reduction of the strain energy. This is mainly due to the additional lateral free surfaces that the 3D island geometry can expose. Additionally, part of the strain can be transferred from the islands to the substrate, profiting of its compliance properties.

Stranski - Krastanov

The SK growth could be interpreted as an intermediate regime between the two described before, as it presents both growth mechanisms: layer-by-layer growth and island formation. In the initial stages of the growth, deposited material covers the substrate creating a flat film called wetting-layer. This behavior can be motivated only by a surface energy balance: if $\gamma_{film} + \gamma_{int} < \gamma_{sub}$ the most convenient arrangement for the atoms impinging on the substrate is to cover its surface. Then, strain effects start to play a non negligible role in the growth. Indeed, if the lattice mismatch is between 2% and 8% (or in other words among the previously described regimes) the wetting-layer (WL) configuration becomes unfavored because the gain obtained from the surface energy balance is overcompensated by the elastic energy cost for the pseudomorphic film growth. Therefore, once the film reaches a critical thickness which relies on the properties of the material (lattice misfit, surface energy and eventually intermixing at the film/substrate interface), the system starts to develop 3D islands, which enhance the strain relaxation by the lateral free surfaces. However, differently from the VW, in between islands the substrate is still covered by the wetting-layer. The stability and the size of islands depend on the balance between the elastic relaxation and the surface energy, or in other words on the values for the lattice mismatch and the surface energy of the deposited material. In particular, the larger is the ratio mismatch/surface energy, the smaller are the islands.

Growth kinetics

Beside this simple thermodynamic description of the principal growth modes for heteroepitaxy, it is worth to mention the role of kinetics. In particular an important parameter which describes the growth kinetics is the ratio between diffusivity, which can be controlled by the temperature, and the deposition rate. Whether this ratio is high, adatoms can diffuse toward the local minimum of the surface chemical potential. Therefore the growth is essentially driven by the minimization of the free energy and it leads to the thermodynamic behavior discussed previously. On the contrary, for high deposition rates the diffusion of adatoms is slowed down by the incoming of new material, which can enhance the growth rate of the surface. For instance, in this condition, a SK growth could evolve into a FM one because adatoms can't rearrange to form islands, but are quickly incorporated in a flat layer nearly as in a stick-where-you-hit regime. This causes an increase in the elastic energy, due to the absence of any effective relaxation mechanisms. However, when a critical thickness is reached, the system can nucleate defects, as misfit dislocations, which reduce the elastic strain. Thus the system can proceed in a layer-by-layer growth as the elastic driving force for islanding is suppressed by the plastic relaxation mechanism.

1.1.2 Growth techniques

The growth techniques that we will consider in this Thesis are based on Chemical Vapor Deposition (CVD) and on Molecular Beam Epitaxy (MBE) [34]. In the CVD, the substrate surfaces is exposed to a controlled vapor environment composed by the precursors gases, as for instance $H_2-SiH_4-GeH_4$ for the growth of SiGe alloys [38]. A chemical reaction at the surface, favored both by the high temperature of the process and by the kinetic energy of the gas molecules impinging on the substrate, transfers the atoms to the growing crystal. The growth is mainly controlled by the pressure of the gases, which sets the deposition rate, and most importantly by the relative pressure ratio between the different precursors. The chemical process at the surface can be favored also by the reaction of the different precursors, which is again controlled by the relative pressures. Typically CVD can achieve a high deposition rate, in far-from-equilibrium conditions, and it is often used for the industrial production. A special case of CVD is the metalorganic CVD (MOCVD), which involves metalorganic gases as precursors. This technique can be used for III-V and II-VI semiconductors and it is capable of growing InP and GaAs with a high purity [34]. In some cases, the decomposition of the precursors can be enhanced by a plasma reactor where the reactive species, as radical or ions, are created directly in the gaseous phase. As a result, they are more reactive when impinging on the crystal surface. Due to the high kinetic energy that these particles can acquired from the plasma phase, low-energy plasma enhanced CVD (PECVD) is usually exploited for experiments [39].

The main difference of MBE [40] is that it is a technique based on a ultra high vacuum condition ($p \simeq 10^{-9}\,\mathrm{Pa}$). The material is deposited by a collimated flux of atoms, directed to the surface. This atomic beam is produced by a Knudsen evaporation cell, where the solid or liquid phases of the material involved in the growth are evaporated by exploiting

a locally high temperature. The uniform deposition over the substrate surface is favored by the spinning of the sample under the evaporation cell. The peculiarity of this growth technique is the precise control on the deposition: it is possible to reach very low rates, up to fractions of monolayer (ML) $10^{-1} - 10^{-2}$ ML/s. The deposit of different species on the same substrate can be obtained by using multiple evaporation cells. The relative composition can be finely tuned by controlling the deposition flux and time for each cell. For instance, MBE has enabled the growth of multi-quantum wells with a nearly monolayer thickness of the different layers involved in the growth.

When an atom reaches the surface, it can diffuse towards the most stable site. This motion is permitted by the high temperature ($T \simeq 500 - 800\,°\mathrm{C}$) of the substrate that is generally used for CVD and MBE growth. This favors the hopping of a surface adatom from a bonding site to another. The flow of material on the surface has to be considered as the net motion of atoms, taking an average of the path of every single atom, as in a random walk description. The diffusion length of an atom is not infinite, therefore it cannot reach the position with the global energy minimum, but can explore only a limited number of configurations in the part of surface nearby. Moreover the deposition flux contrasts the diffusion: if an adatom is covered by a new deposited layer, it becomes a bulk atom, with a higher number of bonds than a surface atom, and as a consequence its mobility becomes negligible.

1.1.3 Ge/Si prototypical system for SK growth

The most studied system for heteroepitaxy on planar substrates is based on the growth of Ge on Si(0 0 1) substrates. An advantage of studying the Ge/Si system is that SiGe is an ideal alloy, therefore Ge and Si can be mixed in any ratio without any polarity effect. Moreover the use of a Si substrate is a major advantage in order to integrate the heteroepitaxial growth with the actual technologies.

Both Si and Ge have the same diamond crystallographic structure, but they have a different lattice parameter a, in particular $a_{\mathrm{Ge}} = 5.65\,\text{Å}$ and $a_{\mathrm{Si}} = 5.43\,\text{Å}$ [23] and the lattice mismatch is: $\frac{a_{\mathrm{Si}} - a_{\mathrm{Ge}}}{a_{\mathrm{Ge}}} = 3.99\%$.

The effect of this lattice mismatch is a compression of the Ge film grown on Si, because it has to match exactly the lattice spacing of the Si underneath. This results in a pseudomorphic tetragonal distortion of the Ge cell, forced to expand in the vertical direction as a response to the compressive state in the substrate plane.

From ab-initio calculations [41, 42], it has been shown that also the surface energy density γ of these two materials is different. In particular $\gamma_{\mathrm{Ge}} < \gamma_{\mathrm{Si}}$, therefore the system prefers to cover all the Si free surface with a Ge film, lowering the surface energy. Considering both the lattice mismatch and the different surface energies, it is possible to conclude that the Ge/Si system follows the SK growth modality [24]. The WL increases up to a critical thickness, which is of $2 - 3$ ML for pure Ge over Si. At this point the elastic contribution overcomes the surface energy one, favoring the formation of 3D islands, as sketched in Fig. 1.2, instead of continuing the growth of the flat WL [43]. These islands allow for a better relaxation of the elastic energy stored in the film, since they can expand in more directions than only in

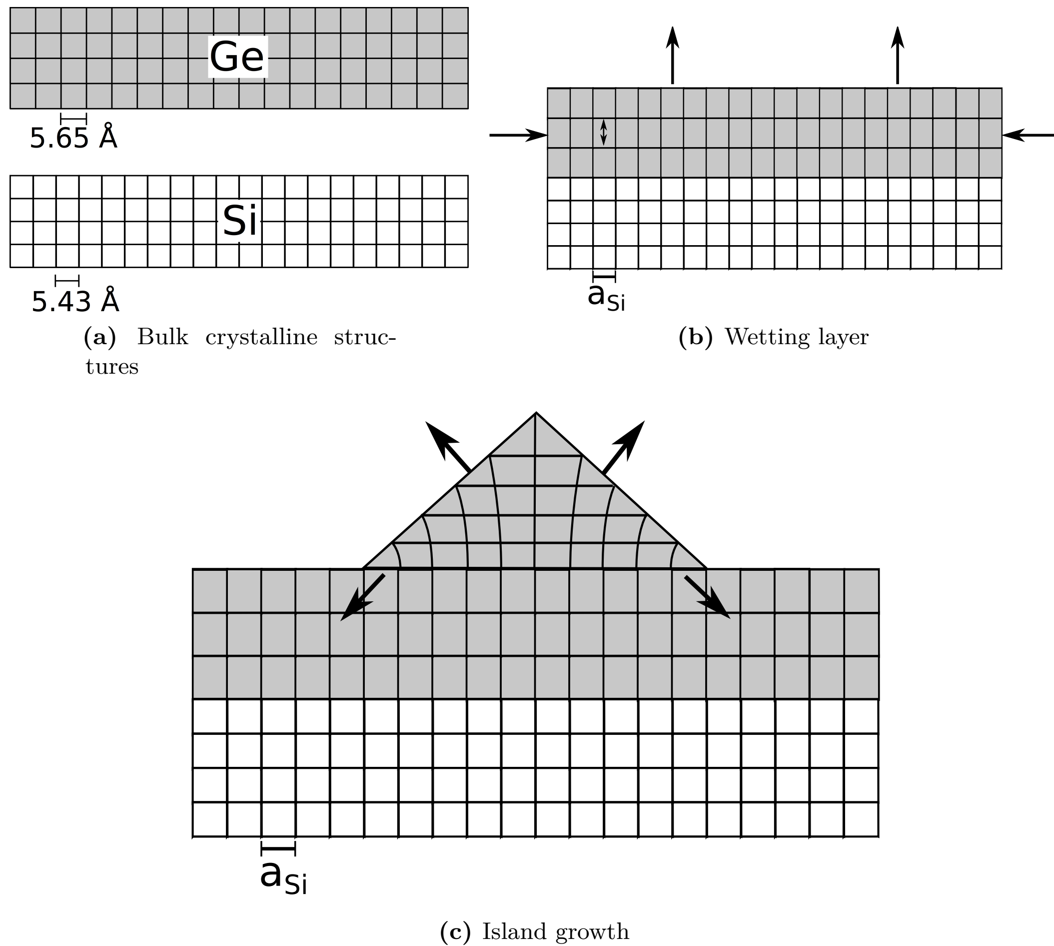

(a) Bulk crystalline structures

(b) Wetting layer

(c) Island growth

Figure 1.2: Scheme for the Stranski-Krastanow growth in the Ge/Si system. Panel (a) represents the bulk structures, showing the greater lattice parameter for the Ge. Panel (b) shows the tetragonal distortion of the wetting layer, that is in a stressed condition. The system, to release the elastic energy, grows a 3D structure, here represented by a triangular island.

the vertical one. This process is fully spontaneous, driven by self-assembly, with no external driving force. The size of these islands is nanometric and depends, as the critical WL thickness, on the alloy composition deposited over Si. In particular higher Si concentrations in the film produce bigger islands, up to a hundred of nanometers wide. This can be justified by considering the lower lattice mismatch [23]. In the following chapters we will neglect all effects related with composition and focus only on a pure Ge film.

1.1.4 An analytical model for island growth: the ATG instability

The instability of a flat film growing in a SK modality was historically modeled by Asaro and Tiller [25], Grinfeld [26] and Srolovitz [27]. In particular, they proposed an analytical description for the evolution of a island instability for a semi-infinite film which is in an elastically stressed condition. Despite the limitations of this linear theory, it is still used as a reference for the description of the growth dynamics [44], particularly for the initial stages of the growth, when there is no interaction between the free surface and the substrate [45]. The theory is based on a cosine-like perturbation of the flat surface, defined as a function of

the position $h(x)$. The evolution dynamics is assumed to be driven by the minimization of the free energy of the system, which is made of an elastic and a surface contributions. The former quantifies the elastic energy stored in the film, which is responsible for the tendency to grow island. Indeed, the island shape, or in the ATG case a perturbation of the profile with a high aspect-ratio (AR or height-to-base ratio), introduces more free surfaces in the system, allowing for an enhanced relaxation of the strain stored in the film. On the contrary, the surface energy term accounts for the energetic cost of creating new free surfaces, and therefore tends to flatten the surface profile. The main result of the ATG theory is that a minimum size for the wavelength of the perturbation is required, in order to make the growth of island favored by the energy balance of the surface and elastic contributions. This critical wavelength is defined as $\lambda_c = 2\pi\gamma/U_\varepsilon$ where γ is the surface energy density and $U_\varepsilon = 2E/(1-\nu^2)\varepsilon_m^2$ quantifies the elastic energy density, with E the Young modulus, ν the Poisson ratio of the film and ε_m the lattice mismatch. Another useful quantity predicted by the ATG theory is the wavelength $\lambda_{ATG} = 3/4\lambda_c$ characterized by the fastest growth rate. Indeed, this is an useful reference to estimate in a first approximation the size of the islands observed in a SK growth mode.

1.1.5 Technological applications

Islands grown by heteroepitaxy, thanks to their confinement properties, can be used as quantum dots for optical applications [46–48]. This requires a specific control on the island sizes, as it determines the optical wavelength to which the quantum dots are sensitive. An example of materials suitable for optical applications are the InAs grown over GaAs [23]. If compared to infrared detectors based on two-dimensional InAs barriers, the quantum dots can detect an optical radiation independently from its direction, thanks to the spacial symmetry of a dot. Another optical application is for solid state lasers [49], which use quantum dots to generate a specific wavelength. In this case the heteroepitaxial technique is useful also to build the resonance cavity [50].

The possibility to create islands buried in a Si film is fundamental for the Dot-FET transistors [51]. The strain differences, given by the strain field of the Ge buried islands, increase the carrier mobility, in particular for the e^- in the case of n-doped Si, and the maximum working frequency of the device.

Taking advantage of the magnetic properties of the quantum dots, it is possible to develop new devices for data storage [24]. Ge islands, embedded in oxides, have become of primary importance for device applications thanks to their ability to store charges for a long time, even at room temperature. Moreover the charge carriers in a MOS transistor can control the conducting channel between source and drain, which is useful in memory devices [52]. Magnetic quantum dots are also fundamental for electronic devices based on spin transport.

Particularly for optoelectronic applications, the possibility to control the positioning and size-uniformity of quantum dots is very important [50, 53], for example in single photon emitters for optical communications [54, 55]. Indeed, a detector can't be based on a single dot, but has to take advantage of many of them at the same time, otherwise the collected

or emitted signal would be too weak. To have a coherent behavior from all of them, the quantum dot array must be ordered. The heteroepitaxial growth on patterned substrates is a viable path to achieve an ordered array of nanostructures by self-assembly.

In general, a pattern consists in creating regions on the surface with specific properties, that can enhance the nucleation of islands [56]. This can be achieved thanks to nano-lithography, which enables a control up to the nanometer scale of the substrate geometry. The shape given to the substrate may consist of pits, with a specific shape and size and a well controlled spacial ordering [29], or mesa [57] and stripes regularly distributed on the surface.

1.2 Heteroepitaxy in nanowire structures

Semiconductor nanowires (NW) can be defined as filamentary crystals with a diameter of the order of few nanometers, and a length from hundred of nanometers to microns [7, 58, 59]. Their historical origin can be assigned to the studies of whisker growth made by a vapor-liquid-solid technique, presented in a work by R. S. Wagner [60]. Indeed, starting from this technique, in the early 1990s Hitachi scientists developed the growth of III-V nanowhiskers [61, 62]. This can be considered as the first example of nanowire growth, as a good positional and directional control of the structures was achieved and the first pn heterojunction was obtained by nanowhiskers. In a short period, the research topic on nanowhiskers and nanorods became of great interest in the scientific community [63]. This is demonstrated by the exponential growth of the research papers on the nanowire topic, which has shortly reached thousands of publications per year. Indeed, the nanowire approach has opened many research fields, which include nanowire electronics, photonics, energy conversion and storage, up to interfaces for living cells. The unique one-dimensionality is what makes nanowires so interesting if compared to nanocrystals in general, offering the possibility to overcome many problems that seem to be unavoidable by the thin film growth techniques. One of the main examples is the capability, enabled by nanowires, to integrate optically active semiconductor, such as III-Vs, on Si, which could drive the development of photonics applications merged with the current electronic technology. The key issue to achieve this result is to find a solution for the large lattice mismatch between group IV and III-V materials, which hinders the development of defect free heterostructures in planar configurations. The optical applications of nanowires were introduced by the demonstration of semiconductor nanolasers, by exploiting ZnO nanowires [64]. This initial idea was then extended to other semiconductor materials, ranging from the UV to the IR frequencies [65]. The possibility to develop a coherent light source with a nanometric footprint has implications in the integration of photonic circuits, of miniaturized sensors, as imaging probes with a high spatial resolution and in general for devices with a low power consumption. Nanowires can be used also for thermoelectrics, as for instance it has been shown that the thermal conductivity of Si can be reduced from the bulk value of 150 down to 8 W/m K thanks to the strong phonon scattering at the sidewalls of the nanowire structure [8]. This could have strong implications for the waste heat recovery and for power generation

applications. Another emerging topic is based on the interfacing of semiconductor nanowires with living cells. Nanowires can be used as transistors or subwavelength optical guides and their cross sections, being much smaller than the typical cell size, guarantees minimal invasiveness [66–68]. For example, applications include the interfacing with DNA, proteins, delivery of small molecules to stem cells, for a controlled stem cell differentiation or for the detection, inhibition and stimulation of the propagation of the neuronal signal [69].

Displays technologies and solid-state lighting nowadays profit of the long-durability and high efficiency of semiconductor light-emitting diodes (LED) [70]. However, there is a variety of applied research fields that require a further miniaturization of the multicolor light sources, as it is for the integrated optoelectronic and nanophotonics systems, for high resolution micro-displays and for high density optical information storage. To this purpose, nanowire-based LED are a promising solution, starting from the first example of GaAs pn-junction up to the more recent demonstration as longitudinal and coaxial heterostructures [71, 72]. Nanowires have also enabled the development of multicolor LED by combining different n-type materials, as GaN (UV), CdS (green light) and CdSe (near-infrared) on the same p-type Si substrate, which is the best solution for an efficient integration with the existing technologies [73]. Still, there is room for developing the nanowire technology by improving the efficiency, minimizing the nonradiative recombination phenomena, and by exploiting environmentally friendly materials.

A similar situation applies to the solar cells world, where there is still the need for inexpensive, but high efficiency photovoltaic devices in order to improve the large scale energy conversion from solar light. One of the main advantages of nanowires is the possibility to offer long absorption path lengths combined with short distances for the collection and transport of charge carries, together with a strong light capture in high density nanowire arrays [19].

Lithium batteries are used in most of our electronic devices. For portable electronics, it is crucial to control the energy per volume and per mass that can be stored in the battery, while for power applications such as for electric vehicles a large energy density is required for improving the range of electric cars, but at the same time a high power is needed to maximize the performances. To address these challenges, once again the nanowire geometry is promising, as it can improve the density of lithium stored in the electrode materials of the batteries. The main problem arises due to the volume expansion that occurs when inserting large amounts of lithium in the electrolyte, eventually causing the mechanical degradation of the device due to strain. This can be efficiently accommodated by the NW geometry [74], which thanks to the high surface-to-volume ratio provides large active surfaces, accelerating the charge-discharge times, and enable a high packing density, if compared to bulk materials.

1.2.1 The vapour-liquid-solid technique

The most common technique to grow semiconductor nanowires is the vapor-liquid-solid (VLS). A liquid phase, usually corresponding to a metal nanodroplet, gathers and decomposed the precursors which are present in the vapor phase, and makes them precipitating in the form of a solid nanowire. The metal which is most commonly used to catalyze the growth

is gold, which has the advantage that it does not oxidize and it is a stable catalyst even at sizes down to few nanometers. Moreover, it works for many materials, ranging from group IV, to III-V to oxides. The growth kinetics of this technique has been investigated in details for a classic Au/Si VLS system profiting of real time observations of the growth via ultra-high-vacuum transmission electron microscopy (TEM) [75]. In the initial stages, a thin AuSi liquid shell is observed around the Au particle as soon as the Si precursor is introduced in the growth chamber. Once the alloying process is complete, the supplied Si results in the nucleation of a solid phase, due to the precipitation of the supersaturated liquid phase. The VLS growth tends to proceeds by a layer-by-layer dynamics, with a nucleation process which occurs at the triple-point junction between the solid, the liquid and the vapor. At the triple junction the formation of an additional small facet can be observed, dependent upon the contact angle of the droplet and related to the nucleation process [76]. The direction along which the nanowire grows is not a fixed property of the material, but it is dependent on the growth conditions. Indeed, for example, it has been shown that the hydrogen atoms that bound to the surfaces of the sample can change the growth direction during growth [77], basically by altering the surface energy balance which drives the stationary shape of the catalytic droplet. In some specific cases, as for the growth of GaN nanowires, it has been reported that the growth direction can be selected by changing the substrate, as it is related to the heteroepitaxial relationship between the GaN crystal and the substrate surface [78]. The crystal structure of the growing nanowire is another property which is influenced by the growth conditions [79]. For instance, III-V nanowires often exhibit a randomly distributed sequence of wurtzite/zinc-blende polytypism. In particular, the growth of different phases can be controlled by changing the temperature or the diameter of the nanowire [80], which is set by the size of the droplet. The control of the nanowire positioning and growth orientation, which are crucial for the application in ordered arrays, can be achieved by using lithographic techniques, which can drive the positioning of the droplet which establish where the nanowire growth occurs. Conventionally, VLS is applied to (111) surfaces for group IV semiconductors, or the (111)B for III-V, which allows for a growth perpendicular to the substrate surface.

One of the main drawbacks of the gold-catalyzed growth is that when Au atoms are incorporated in semiconductors, as for Si and Ge, they can create deep level traps and scattering centers [81]. This issue can be avoided by exploiting self-catalyzing techniques, in which the material of the droplet is also used to fabricate the semiconductor crystal, as it is for the Ga assisted growth of GaAs nanowires [21, 82].

1.2.2 Core/shell structure

Core/shell nanowires correspond to the formation of a radial heterostructure on a nanowire. This is generally achieved by hindering the axial growth, which has produced the formation of the core structure, and by promoting a nearly 2D epitaxy on the nanowire side facets, generating the so called shell of the nanowire. In the case of VLS growth, this result can be achieved by crystallizing or removing the droplet. In the case of Ga-catalyzed growth, for instance, it is possible to stop the Ga supply while increasing the As one and

reducing the growth temperature. In the case of Au droplet, it can be crystallized by an increase of the precursor flow or a reduced temperature or it can be removed, trying to reduce the possible contamination source represented by Au, by ex-situ etching techniques, for example with a Iodine solution [83]. Once the catalyst has been removed, the precursor gases can react all over the surface, promoting the axial growth as well as the radial one, which thanks to the higher surface can collect also an higher volume of material. The most natural application of the core/shell structure is to develop an heterojunction, with an high interface area. This is exploited for instance in the optical applications for solar cells, where one of the advantages of nanowires is to have a higher surface that can capture the incoming light [84].

Furthermore, the core/shell configuration has also a structural role, as the substrate required for the growth of the active layer for the applications is here represented by the core. With respect to planar substrates, core/shell nanowires can profit of efficient mechanisms for the strain relaxation, as we will describe in Chapter 5, and they could be compared to the growth on thin substrates, or more in general on substrates with a high elastic compliance. Core/shell nanowires can also enable the transfer of the crystal structure from the core to the shell, applied for instance to grow in the wurtzite (WZ) phase some semiconductors which would otherwise grow with a cubic crystal strucure [20, 83, 85].

1.3 Selective area epitaxy

Another technique which allows for the growth of nanowires is the selective area epitaxy (SAE) [86, 87]. The main difference with the VLS method is the absence of a catalyst droplet on the top of the nanowires during growth. Indeed, the growth dynamics relies only on the preferential formation of crystal facets. Depending on the growth conditions, different facets are formed on the surface of the growing crystal and their relative area is related to the corresponding growth rates. The conditions that lead to the growth of nanowires correspond to the case of a fast growing facets, e.g. the (1 1 1)B for III-V semiconductors, and slower growth front perpendicular to the fast one, e.g. $\langle 1\,1\,0 \rangle$ facets [88]. The parameters window to achieve this type of growth is often limited in temperature and partial pressure of the precursors [87]. In particular, a growth temperature higher than the congruent one for III-V is required to prevent the formation of droplets during growth [89]. Moreover, the choice of the substrate surface is limited, as the normal to the substrate should coincide with the growth direction of nanowires.

This growth requires a fundamental ingredient, which is selectivity. Indeed, in principle, just by tuning the growth conditions one would achieve a growth of the whole substrate surface, without the mono-dimensionality which is typical of nanowires. Therefore, it is fundamental to restrict the growth process to some small portions of the substrate surface, which represent the basis of nanowires. This can be achieved by creating a mask made by an amorphous film, generally SiO_2 or SiN_x on the substrate by lithographic techniques. In particular, the amorphous layer can be deposited by radio-frequency sputtering, plasma-enhanced chemical vapor deposition, or thermal oxidation. Then some circular openings

are created in this layer by using electron-beam lithography and wet-chemical etching, so that the growth of the crystal is allowed only in these regions, but not on the amorphous surface. The size of the opening can control the width of the structures that grow, and this technique offers also a control on the positioning of the nanostructures, achieved thanks to the lithographic patterning of the mask.

The SAE is not limited to the growth of nanowires, but can be applied to achieve a bottom-up growth of several types of nanostructures. For example, the growth of quantum dots with a precise control of the position and for different substrates orientation has been studied for GaN [90], GaAs [91] and SiGe [92], with the aim of developing optoelectronic, photovoltaic and photo-electrochemical applications. The shape of the openings in the amorphous layer can be also be extended in one direction, developing lines of finite extension. This enables the growth of horizontal nanowires, or more generally this leads to the growth of fin-like structures [93]. This type of nanostructures are studied, for example, for the possible applications in the FinFET technology [94, 95] or for silicon-integrated photonics [96, 97]. Recently, SAE has been exploited also to growth nanomembranes structures [98–103], which extend vertically from the substrate forming quasi-two-dimensional structures. This latter case will be analyzed in details in Chapter 2, with particular attention to the growth dynamics which leads to such a peculiar growth mode.

Chapter 2

Modeling the kinetic crystal growth

The growth of vertical nanostructures is one of the most active topics in materials science. This is motivated by the need of novel technologies that can go beyond the innovation process exploited so far by the miniaturization of planar devices. For instance, the possibility to use a 3D nanostructure has enabled the development of Fin-FET technologies, of nanowires-based applications or of micro-pillars technologies. Among all these areas, the growth of vertical nanomembranes, characterized by a lower symmetry with respect to nanowires, is the one that still needs a complete understanding of the growth dynamics. In this Chapter, we propose a novel modeling approach to tackle the 3D growth of nanostructure, with particular attention to the peculiar kinetic conditions that lead to a vertical growth.

2.1 Introduction to crystal faceting

The most distinctive feature of a crystal is its faceting, both on a macroscopic scale and on a nanoscale [104]. In this latter case, since the surface-to-volume ratio is higher, the faceting can play a crucial role in determining the material properties, and therefore it is important to control facets in view of possible applications. The understanding of the crystal faceting has been widely studied in the literature, since the 19th century. The most remarkable study is the one by G. Wulff in the 1901 [14] where he proposed the well known geometric construction. It allows to determine the faceting from the definition of the surface energy density of the crystal, and in particular for the possible orientations of the surface, as sketched in Fig. 2.1 in 2D. The construction consists in plotting in polar coordinates the surface energy density γ as a function of the surface orientation $\hat{\mathbf{n}}$. Then, at each point of this curve, the tangential plane is drawn, which corresponds to a line perpendicular to $\hat{\mathbf{n}}$ for the 2D construction. The inner envelop of this system of planes identifies the surface of the crystal. Notice that this construction provides the geometry, but it is size independent and in principle can be re-scaled to any length. The key assumption, on which the Wulff construction is based, is the minimization of the surface energy of the system [105]. Therefore, the crystal morphology obtained following this construction is

called as equilibrium crystal shape (ECS). The resulting shape can be interpreted as the optimal balance between the tendency to expose the facets with the minimum energy density and the total surface area of the crystal. The thermodynamic assumptions that are required by the definition of the ECS [106, 107] make it a reliable tool to inspect the faceting of finite crystals in annealing conditions or, more generally, in close-to-equilibrium growth processes, such as at high temperatures or at slow growth rates. This implies that the material which is supplied by external sources to the crystal can be incorporated in the position which guarantees the minimum increase of the total energy of the system. This means that the evolution pathway is composed only by the minimum energy configurations for the different volumes of the growing crystal.

However, when considering growth processes, it is more likely to have out-of-equilibrium conditions, that in principle can alter the crystal faceting with respect to the ECS predicted by the energy minimization. In these cases, a more reliable modeling of the crystal faceting can be provided by a different geometrical construction, called kinetic crystal shape (KCS) [12, 108, 109]. This is obtained by explicitly considering the motion of the facets of the crystal, which is done by assigning a growth velocity $v = v(\hat{\mathbf{n}})$ to each surface plane. This morphology can be obtained geometrically also by considering the Wulff construction, but using the $v(\hat{\mathbf{n}})$ in place of $\gamma(\hat{\mathbf{n}})$, as it is shown in Fig. 2.1.

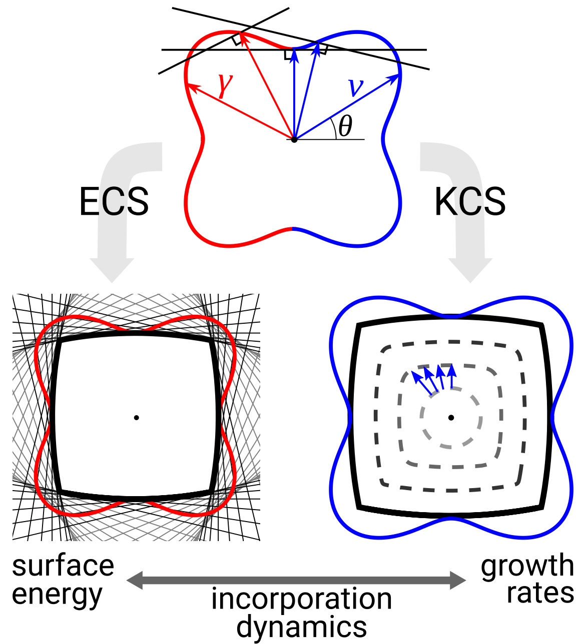

Figure 2.1: Schematics of the Wulff construction for the ECS, starting from a γ-plot, and the KCS, starting from a v-plot. The geometric construction is the same for both cases and it is sketched for the ECS only. An illustrative growth sequence for the evolution of a circular seed to the KCS is illustrated by the dashed profiles and it is obtained by moving points accordingly. (from Ref. [110])

The geometrical constructions considered so far are defined as scale-independent. This means that, to determine the crystal shape of particles with different volumes, it is sufficient to scale the geometrical shape to have the prescribed volume. Even if this could apparently be an advantage of these techniques, making them extremely flexible, as a major drawback

both ECS and KCS can't provide any information on the kinetic pathways. In particular, the ECS just describes the minimum energy configuration, while the KCS provides an evolution of the growth front, but only under stationary conditions. However, it is more likely the case that the initial seed for the crystal growth has a different shape if compared to the stationary one, reached at later stages of the evolution. Therefore, the initial stage when the relative extension of the facets is changing to adapt to the prescribed stationary shape cannot be described neither by ECS nor by KCS. A first approximation of this dynamics can be achieved by tracing the evolution of the surface planes according to the prescribed velocity $v(\hat{\mathbf{n}})$, as in the so called Borgstrom construction [111], shown by the dashed profiles in Fig. 2.1(b). Just by geometric arguments, it is found that the slowest growth front tends to increase their surface area at the expenses of the fastest one, up to closing and expelling them out of the growing profile, provided that they are not included in the KCS.

In principle, the ECS can be considered as an intrinsic property of the material for a specific set of growth conditions such as temperature, pressure of the precursors and surface reconstruction. Therefore, the ECS can be determined just by computing the surface energy of all the possible facets of the crystal, for instance by ab-initio simulations. On the contrary, the estimation of the growth velocities required by the KCS construction is more complex and requires a direct comparison with the experiments. Indeed, the growth rates of the facets result from the combination of intrinsic properties of the crystal structure at the surface, related for instance to the incorporation sites, but also from the growth process, which involves the reactants, the distribution of the species in the surrounding environment, the chemical reactions at the surface and possible side reactions, such as etching and passivation, and finally by the sticking coefficient of the surface [104]. This higher complexity of the parameter space for the KCS construction introduces a variability between ECS and KCS.

To be more precise, KCS and ECS can be interpreted as the two limiting cases in growth conditions driven by kinetics or thermodynamics, respectively. The thermodynamic regime is achieved when the surface diffusion prevails over the external supply of material. This allows for a full redistribution of material on the surface toward the minimum energy configuration. Conversely, the kinetic growth regime implies a short-range diffusion length, possibly limited by the fast material supply that hinders the diffusion. Therefore, the material cannot rearrange on the surface toward the minimum energy configuration.

In between these two extremes, an intermediate regime is still possible, characterized by both the diffusion and the incorporation dynamics. This condition was firstly formalized by J.W. Cahn and J.E. Taylor in Ref. [15], and derived by mathematical assumption in Ref. [11]. The main feature of this approach is to consider that atoms, when deposited on the surface, need a finite time before being incorporated into the crystal lattice. In the meanwhile, they can diffuse on the surface, eventually migrating on different facets. Since the incorporation is affected by the lattice structure at the surface, often it is an orientation-dependent property.

In Ref. [112], C. Stöcker and A. Voigt investigated the effect of an isotropic kinetic term on the faceting, in annealing conditions, of crystal surfaces caused by strongly anisotropic

surface free energies. Later, Rätz et al. in Ref [113] introduced an anisotropic kinetic term, dependent on the facet orientations. It is the goal of this Chapter to extend such study to the case of a growing crystal, showing how faceting can change from ECS to KCS by controlling the incorporation kinetics. To this purpose, a phase-field (PF) approach [10, 114] is exploited, as detailed in the Section 2.2. Simulation results are first reported for a few test cases in Section 2.2.1, showing in a systematic way how the crystal faceting may occur because of anisotropies in the incorporation dynamics. Then, in Section 2.2.2, the competition between anisotropic surface energy and/or growth rates and the incorporation dynamics is investigated. More specifically, we show the possibility to account for intermediate morphologies that recover the ECS and the KCS as limiting cases. Finally, an application to morphologies observed in experiments is reported in Section 2.2.3 to validate the method and illustrate its capabilities.

2.2 Continuum modeling of kinetic growth by phase-field

The kinetic regime for the growth of faceted crystals is here investigated by using the model presented by Cahn and Taylor in Ref. [15]. The numerical implementation is then performed by exploiting the phase-field approach, as described in Ref. [113]. In the following, we will describe the setup of the model, with particular attention to the physical meaning of the different mathematical operators.

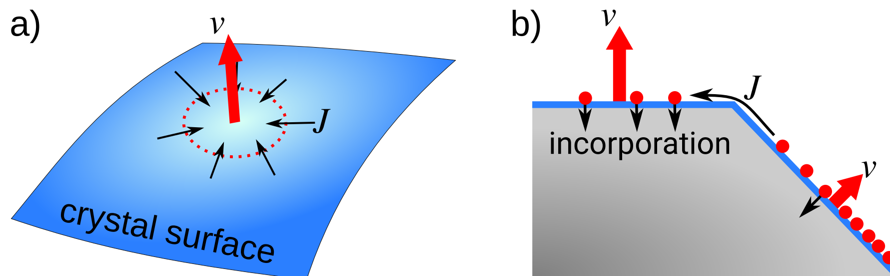

Figure 2.2: Schematics of the growth model. (a) The normal velocity v of the surface profile is due to the local material accumulation by the surface material flow J. (b) The surface evolution can be limited by the adatom incorporation on the surface. Adatoms can diffuse on the surface due to gradients in the chemical potential, for instance due to different adatom concentrations.

Generally, the growth of a crystal is achieved by the net transfer of material from a surrounding phase, mainly a vapor or a liquid, to the lattice structure of the crystal itself. This phenomenon is mediated by the crystal surface, which stays in between the two phases. On the surface, adatoms can diffuse, interact or desorb before the incorporation into the crystal lattice occurs [115, 116]. In order to provide a description for this process, we have to focus on the adatom dynamics. As we want to deal with a mesoscopic scale, we choose to adopt a continuum description of the system. Therefore, we cannot follow the trajectory of the single adatoms, or more in general of the mobile species, but we can infer just on their density N. The temporal evolution of the adatom density at each point $\mathbf{x}$ of the surface can be determined by considering a continuity equation. This includes the external material

supply from the vapor or liquid phase, here identified as a deposition flux F, and a sink of material that accounts for the incorporation of adatoms into the crystal lattice with a rate v, which describes the motion of the crystal surface as due to the material incorporation. With these terms, the continuity equation is

$$\frac{\partial N}{\partial t} = \nabla_{\rm s} \cdot [M \nabla_{\rm s} \mu] + F - v. \tag{2.1}$$

where M is the adatom mobility, μ is the local adatom chemical potential and the operator $\nabla_{\rm s}$ is the gradient along the surface. The diffusion of adatoms on the surface, according to the Onsager linear law, follows the gradient of the chemical potential on the surface: $\mathbf{J} = -M\nabla_{\rm s}\mu$. The external material supply, in general, depends on the local surface orientation, $F = F(\hat{\mathbf{n}})$, as it can be determined by a directional deposition flux, or it can be related to the solidification properties of each facet in the case of a liquid-to-solid transformation, or even to the different reactions at the surface of a gaseous precursor. Here, for the sake of simplicity, the mobility is considered isotropic, and no explicit desorption dynamics is modeled, considering that its effect is implicitly included in the modeling of the net material supply.

The second important dynamics that has to be defined in order to have a complete picture of the growing system is the incorporation process. The attachment/detachment of adatoms into the lattice is quantified by the velocity v as it implies a motion of the surface front due to the additional material which is incorporated in the structure, as sketched in Fig. 2.2(b). In a first approximation [11, 117, 118], the incorporation rate can be considered as proportional to the difference between the chemical potential of the adatom phase and the chemical potential $\mu_{\rm eq}$ on of the crystal phase, at each point on the surface:

$$v = (\mu - \mu_{\rm eq})/\tau, \tag{2.2}$$

where τ is a kinetic coefficient setting the timescale of the attachment/detachment process. By considering a physical interpretation of this equation, the coefficient τ corresponds to the adatom lifetime before being incorporated. As this process depends on the local incorporation sites present on the surface, this coefficient $\tau = \tau(\hat{\mathbf{n}})$ can depend of the surface orientation. The equilibrium chemical potential is defined as the functional variation of the free energy G ($\mu_{\rm eq} = \delta G$) with respect to the change in the surface profile, which corresponds to the material incorporation. In this model, we limit the description to the surface energy, neglecting for instance elastic contributions to the chemical potential. Therefore, $\mu_{\rm eq} \sim \nabla_{\rm s}\xi$, with $\xi = \nabla(r\gamma(\hat{\mathbf{n}}))$ the Cahn-Hoffmann vector (r the magnitude of vector $\mathbf{r} = r\hat{\mathbf{n}}$)[119, 120]. If we considered a simplified 2D system, this can be rewritten as $\mu_{\rm eq} \sim \kappa(\gamma + \gamma''(\theta))$, with κ the profile curvature, γ the surface energy density and θ the local orientation of the surface.

Following Ref. [15], we assume quasi-stationary conditions for the adatom density, which is equivalent to imposing that $\partial N/\partial t \approx 0$. Then, the continuity eq. (2.1) can be combined with the attachment/detachment eq. (2.2) in a coupled system for two equations and two

unknown variables:

$$\begin{cases} v = \nabla_{\rm s} \cdot [M \nabla_{\rm s} \mu] + F \\ \mu = \mu_{\rm eq} + \tau v \end{cases} \tag{2.3}$$

which allows to describe the profile evolution that results from the adatom incorporation dynamics. As it is evident by looking at the second equation, the chemical potential μ for the adatom phase includes both the thermodynamic contribution $\mu_{\rm eq}$, which accounts for the crystal structure energetics, and the kinetic term, which is implicitly proportional to the velocity v. In the thermodynamic regime, characterized by an infinitely fast incorporation time $\tau \to 0$, the chemical potential of the adatom phase becomes equal to the one of the atoms which are already incorporated in the crystal, $\mu \to \mu_{eq}$. In this case, the diffusion of adatoms is driven directly by the surface energy differences. Therefore, the morphology of the crystal would evolve to the ECS in the case where the material supply is negligible, or to a KCS when the adatom mobility can be considered as null if compared to the material supply.

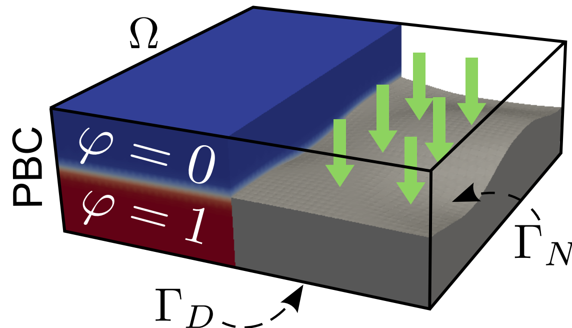

Figure 2.3: Schematics of the geometry representation in the phase-field model. On the right the explicit system geometry and on the left its representation by means of the phase-field function φ in the domain Ω. Boundary conditions periodic (PBC), Dirichlet (Γ_D) and Neumann (Γ_N) are marked too. The green arrows represent the deposition flux.

This implicit problem for the chemical potential μ and the profile evolution v cannot be solved analytically for a generic 3D profile [10, 11, 121]. Therefore, a numerical approach is required to handle this type of model. In particular, a phase-field approach is ideal to efficiently deal with the numerical solution of this problem, with the advantage of considering any morphology, with no specific limitation on the crystal shape and topology. This is made possible thanks to the implicit description, sketched in Fig. 2.3, of the system by the the phase-field function φ, set equal to 1 within the crystal and 0 outside. The surface profile is nominally located at the $\varphi = 0.5$ iso-line in 2D or iso-surface in 3D (as shown in following plots). This function is initialized in the simulation domain Ω with the function $\varphi(\mathbf{x}) = 0.5[1 - \tanh(3d(\mathbf{x})/\epsilon)]$ with d the signed-distance between the point $\mathbf{x}$ and the surface profile and ϵ a parameter setting the width of the diffused-interface, corresponding to the surface region. The velocity v, describing the evolution of the crystal surface, is then expressed as a variation with time of φ, so that eq. 2.3 becomes:

$$\begin{cases} \dfrac{\partial \varphi}{\partial t} = \nabla \cdot [M(\varphi)\nabla\mu] + F|\nabla\varphi| \\ g(\varphi)\cdot\mu = \mu_{\text{eq}} + \epsilon\tau(\hat{\mathbf{n}})\dfrac{\partial\varphi}{\partial t} \end{cases}, \tag{2.4}$$

where $g(\varphi) = 30\varphi^2(1-\varphi)^2$ is a stabilizing function [122–124] and $M(\varphi) = M_0(36/\epsilon)\varphi^2(1-\varphi)^2$ is the mobility function. This is particularly required to limit the evolution to the surface, i.e. in the diffused-interface, so to reproduce a surface diffusion, neglecting any bulk contribution to the mass transport.

As demonstrated in Refs. [10] and [125], the equilibrium chemical potential for the general case of anisotropic γ is:

$$\begin{aligned} \mu_{\text{eq}} = -\epsilon\nabla\cdot[\gamma(\hat{\mathbf{n}})\nabla\varphi] + \frac{1}{\epsilon}\gamma(\hat{\mathbf{n}})B'(\varphi) + \\ -\nabla\cdot\left[\left(-\frac{\epsilon}{2}|\nabla\varphi|^2 + \frac{1}{\epsilon}B(\varphi)\right)\nabla_{\nabla\varphi}\gamma(\hat{\mathbf{n}})\right], \end{aligned} \tag{2.5}$$

where $\nabla_{\nabla\varphi}$ is the gradient defined with respect to the $\nabla\varphi$ direction. In order to numerically handle strong anisotropy conditions, the Willmore regularization [10] is also implemented. This corresponds to introducing a small corner rounding [126], due to an energy cost for the curvature at the corners. This is modelled by adding an additional term to μ_{eq} in eq. (2.5):

$$\mu_W = \beta\left[-\nabla^2\kappa + \frac{1}{\epsilon^2}B''(\varphi)\kappa\right], \tag{2.6}$$

with $\kappa = -\epsilon\nabla^2\varphi + (1/\epsilon)B'(\varphi)$, and β a coefficient to set the strength of the rounding. By including this regularization, the system of partial differential equations to be solved has now a sixth order, but still can be solved numerically through the implementation for the PF approach [127].

In order to set the anisotropic functions $F(\hat{\mathbf{n}})$, $\gamma(\hat{\mathbf{n}})$ and $\tau(\hat{\mathbf{n}})$ in a reliable way, we follow Refs. [127, 128], and use the generic continuum function:

$$f(\hat{\mathbf{n}}) = f_0 + \sum_i f_i(\hat{\mathbf{n}}\cdot\hat{\mathbf{m}}_i)^w \cdot \Theta(\hat{\mathbf{n}}\cdot\hat{\mathbf{m}}_i) \tag{2.7}$$

with the baseline value f_0 and maxima (or minima if $f_i < 0$) at the assigned orientations $\hat{\mathbf{m}}_\mathbf{i}$, with height (depth) set by f_i and width w. In the following, we set f_0=1 for $F(\hat{\mathbf{n}})$ and $\gamma(\hat{\mathbf{n}})$, while it is 0 for $\tau(\hat{\mathbf{n}})$. w is chosen to exclude any overlap between the different peaks: it is set to 50 for $F(\hat{\mathbf{n}})$ and $\gamma(\hat{\mathbf{n}})$, and to 100 for $\tau(\hat{\mathbf{n}})$. Outward-pointing vectors are only considered thanks to the Heaviside function Θ, thus permitting to treat systems without inversion symmetry. The choice of $\tau_0 = 0$ means that all the facet orientations that we do not consider have an instantaneous incorporation dynamics, therefore they tend to incorporate and to grow faster.

The numerical solution of eq. 2.4 is obtained by Finite Element Method (FEM) with the AMDiS toolbox [17, 18]. The integration scheme for the time evolution is semi-implicit, and the mesh is adaptive, with a finer refinement in the diffuse-interface where the critical evolution of the PF function occurs. For the 2D simulations we use $\epsilon = 0.05$, while for the

3D we set $\epsilon = 0.2$. Neumann boundary conditions, corresponding to a zero flux dynamics, are imposed on the boundaries of the simulation domain Ω.

In the following, we present dimensionless parameters for F, γ, τ and M. This allows to focus on the relative weight of the different terms of the model. If the experimental time and size scales have to be matched, a unit measure analysis returns the following scaling of the simulation parameters: $[F_0] = [l][t]^{-1}$, $[\gamma_0] = [e][l]^{-2}$, $[\tau_0] = [t][e][l]^{-4}$, $M_0 = [l]^6[e]^{-1}[t]^{-1}$ with respect to the length $[l]$, time $[t]$ and energy $[e]$ units.

2.2.1 Faceting by orientation dependent incorporation dynamics

The first point that has to be addressed for a full characterization of the kinetic growth model is the capability of reproducing a crystal faceting by considering an anisotropic incorporation $\tau(\hat{\mathbf{n}})$. All the other parameters, in particular the surface energy $\gamma(\hat{\mathbf{n}}) = \gamma_0$ and material supply $F(\hat{\mathbf{n}}) = F_0$ are considered as isotropic, thus they should drive the profile evolution toward a spherical shape, or a circle in 2D.

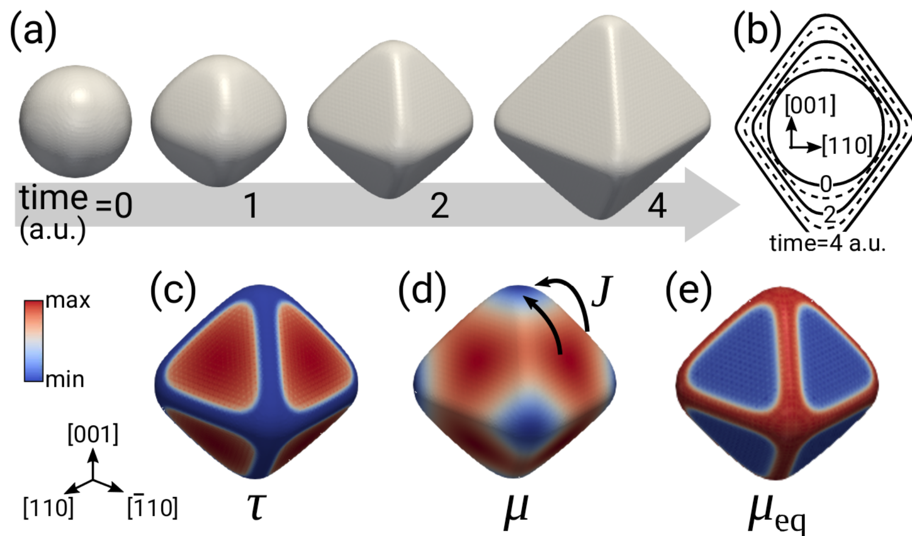

Figure 2.4: (a) Growth simulation of a {111} faceted shape with the kinetic incorporation term. (b) Time evolution of cross-section profiles. Color map for (c) the incorporation time τ, (d) the chemical potential μ and (e) the equilibrium chemical potential μ_{eq}, corresponding to the surface curvature. $\tau_{111} = 20$ and $M_0 = 0.1$. (from Ref. [110])

With these assumptions, in Fig. 2.4, the growth of an octahedral crystal is studied. The initial shape is set as a spherical nucleus, to ensure that no faceting is induced due to the initial state of the system. The incorporation time $\tau(\hat{\mathbf{n}})$ is set with maxima along the $\langle 1\,1\,1 \rangle$ orientations, as it is shown in the color map in panel (c) for the profile corresponding at t=2. As a consequence of this anisotropy, the adatom chemical potential μ is maximum at the center of the $\{1\,1\,1\}$ facets, where the incorporation is lower and a higher density of adatoms is collected. On the intermediate regions, the adatom incorporation is faster, being $\tau(\hat{\mathbf{n}})$ lower, therefore the μ is also minimum, corresponding to a lower adatom density. The distribution of the chemical potential on the surface is made evident in panel (d). Another difference can be noted between the edges and the vertexes. These are the absolute minima

of the chemical potential. This allows for the fastest incorporation on these regions, which is strictly required to keep straight facets, preventing a significant corner rounding. The most interesting fact, that comes out from the comparison of the color maps, is that the adatom chemical potential is opposite with respect to the equilibrium one μ_{eq}. This is proportional to the surface curvature, as γ is isotropic, and would drive the evolution toward a global rounding of the particle. This tendency is still active at the edges, where the kinetic term becomes lower and hence the evolution by curvature minimization is effective, leading to a rounding of the edges. As it is made evident by the cross-section profiles in Fig. 2.4(b), the rounding is more pronounced at the facet vertexes, where the curvature is maximum, while the edges are sharper, as the wider angle between the adjacent facets already provides a lowering of the local curvature.

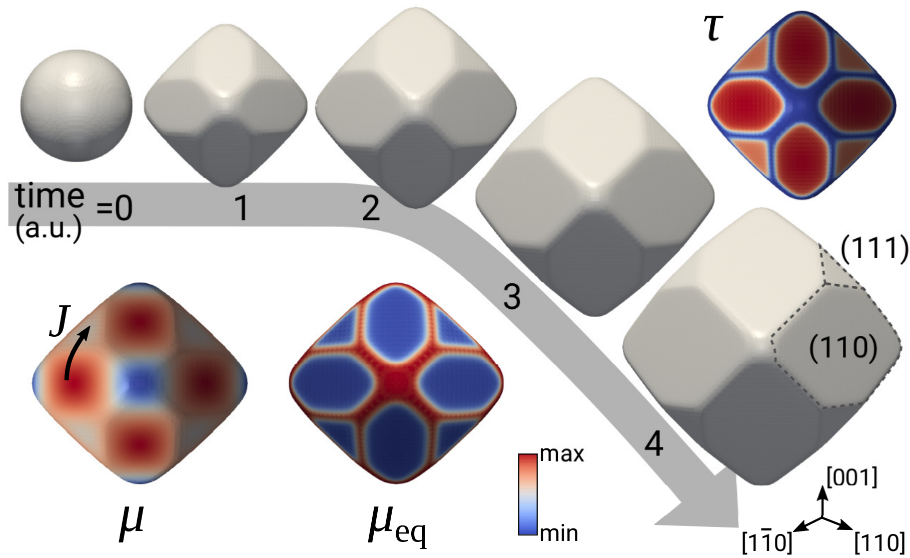

Figure 2.5: Growth simulation of a faceted shape with competing {110} and {111} facets, with τ = 20 and 16 respectively. Color maps show the the incorporation time τ, the chemical potential μ and the equilibrium chemical potential μ_{eq} on the surface. M_0 = 0.1 . (from Ref. [110])

The basic mechanisms analyzed so far apply also to the case where different facets, with different incorporation times, are considered. However, while the polyhedron bounded only by {1 1 1} facets has a growth dynamics which is equivalent to a KCS construction with assigned growth velocities for the facets, the existence of different sets of facets turns out to produce a new growth dynamics. Indeed, the difference in τ makes the facets compete for the collection of the material which is incoming on the surface. The first example of this type of growth dynamics is reported in Fig. 2.5, where both {1 1 1} and {1 1 0} planes are included in the simulation, as they are local maxima in the $\tau(\hat{\mathbf{n}})$ function. In particular, we have chosen that $\tau_{111} < \tau_{110}$, as shown by the color map. As it is expected, in the initial stages both facets tend to appear on the crystal morphology. Indeed, they correspond to slower growing front with respect to the intermediate orientations, which grow faster leading to the vertexes and edges formation. However, since {1 1 0} tend to accumulate more adatoms than the {1 1 1} due to the higher τ, a net material transfer from {1 1 0} to {1 1 1} is observed. This results in a lateral expansion of the {1 1 0} due to a faster growth velocity

of the {1 1 1}. This is shown also in the color map for the chemical potential μ, which is lower on the {1 1 1}, maximum on the {1 1 0} and minimum on the edges and vertices. As in the previous case, the equilibrium chemical potential μ_{eq} would drive the opposite evolution toward the rounding of the shape, as it is maximum on the edges and vertices which have the highest surface curvature. This demonstrates that also in this case the faceting of the crystal is purely determined by kinetics, and not by the surface energy minimization.

The magnitude of the material exchange between facets depends on the relative difference in incorporation times, which corresponds to a different tendency to accumulate adatoms on the surface. This is made evident in Fig. 2.6, where the faceting during growth of a circular 2D profile is studied by considering local maxima of τ in both {1 0} and {1 1} directions. The crystal evolution is compared for two different ratios of the incorporation times, for a case where τ_{10} is just 10% greater than τ_{11} and another where it is two times larger. In the former case, both {1 0} and {1 1} facets coexist, returning an octagonal shape with {1 0} segments extending slightly more than {1 1} ones. In the latter case, the evolution is different as the growth rate of the {1 1} facets is enhanced by the adatom transfer from the slow {1 0}, so that this reduces in size up to its disappear, or at least it is not distinguishable from the rounding of the corners of the resulting {1 0}-bounded shape.

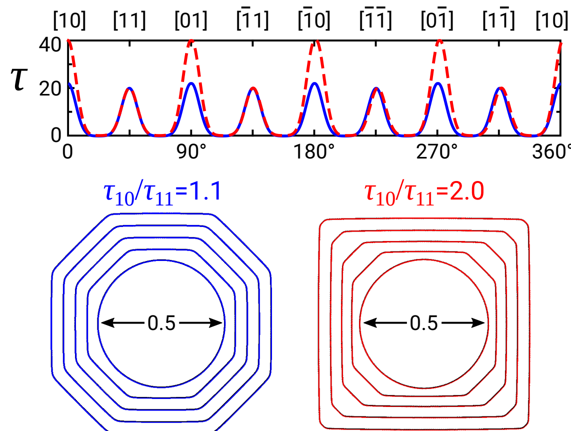

Figure 2.6: Comparison of the shape evolution from circular to faceted shape for different τ_{10}/τ_{11} ratios, by using the anisotropy functions shown in the top panel. (from Ref. [110])

The competitions between facets discussed so far closely resemble the principles of the KCS. Indeed, the hierarchy of incorporation times roughly corresponds to the hierarchy of the facet growth rates. However, there is a big difference between the two approaches. At variance from the KCS construction, the facet velocities are not constant during the growth, by they are dynamically assigned by the redistribution of material on the surface, and in particular by the exchange between adjacent facets. This process is enabled by the surface diffusion, which is mediated by the diffusion coefficient which limits the diffusion length of adatoms. This property can have an important effect on the faceting dynamics as the material transfer between facets can be effective only if the length scale of the system is comparable with the diffusion length.

This is made evident in Fig. 2.7, where the effect of changing the size of the system or

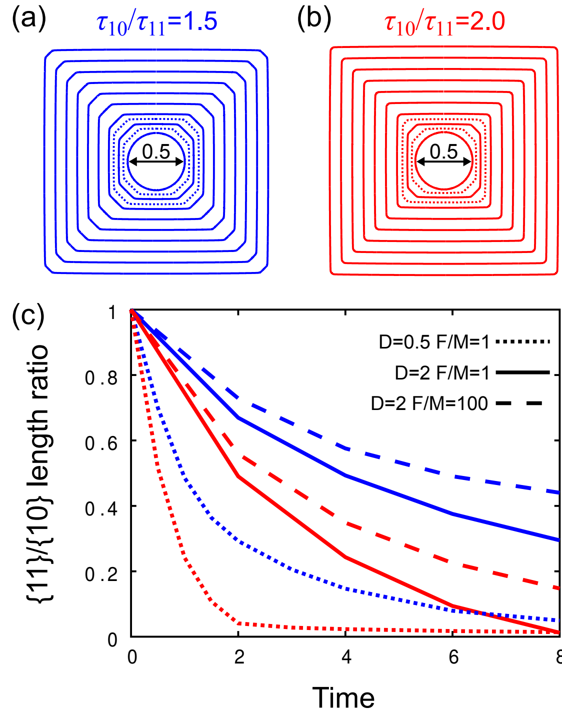

Figure 2.7: (a-b) Time evolution of the surface contours for two different τ_{10}/τ_{11} ratios. (c) Plot of the $\{1\,0\}/\{1\,1\}$ area ratio for two sets of τ (blue as in panel (a), red as in panel (b)) for different diameters D of the initial shape and F_0/M_0 ratios. (from Ref. [110])

of reducing the surface mobility is studied for the faceting driven by $\{1\,0\}$ vs. $\{1\,1\}$ facets, comparing two different ratios between the incorporation times. These are illustrated in panels (a) and (b), where the time evolution of the same initial circular shape is reported. As it has been already discussed, the facets with an higher τ, i.e. the $\{1\,0\}$, tend to prevail on the faceting of the structure. In particular, in the evolution of panel (a), the material transfer toward $\{1\,1\}$ is stronger so that they quickly shrink and disappear, and the resulting shape is a $\{1\,0\}$-faceted square. On the contrary, in panel (b), the material transfer is slower due to a smaller difference in the incorporation times. Therefore, $\{1\,1\}$ facets persist for a longer time. A better understanding of these processes can be achieved by comparing directly the evolution over time of the ratio between $\{1\,0\}$ and $\{1\,1\}$ surface areas, as shown in Fig. 2.7(c). In both cases, the trend for the $\{1\,1\}$ shrinkage is exponential, with a lower velocity for the case of a smaller τ ratio. Indeed, as the facet size decreases, the same volume of material from the $\{1\,0\}$ is spread over a smaller $\{1\,1\}$ area, resulting in a faster increment of the growth rate.

Another interesting comparison can be made by considering a particle which is four-times larger. In this case, with respect to the previous one for the smaller particle, the trend for the $\{1\,0\}/\{1\,1\}$ ratio grows significantly slower. This can be easily explained by considering that the diffusion cannot cover any more the whole facet area, or at least it takes a longer time. Therefore, the competition between facets is less effective as it is more influenced by the rate of the external material source. This apparently simple property of the model represents a major difference with respect to the KCS construction, which can predict only

a self-similar morphology without taking into account the possibly limited material flow on larger facet areas. A similar behavior is found also in the case of lower mobility, which still influences the diffusion length for the surface transfer of material. As a consequence, when the competition between facets is significantly slowed down, the multifaceted morphology can be considered as metastable, even if the same τ for a smaller particle, or an higher mobility, would quickly make a facet disappear from the crystal morphology.

2.2.2 Competing regimes driving the crystal faceting

The orientation-dependent incorporation times need a surface diffusion dynamics to promote the faceting of the crystal. Moreover, by looking at the eq. (2.3), we can note that in the balance for the chemical potential, the kinetic term has to be larger than the equilibrium chemical potential μ_{eq}. This means that an out-of-equilibrium condition is required to observe such a growth dynamics. This is made evident by the analysis in Fig. 2.8, where different material supplies and incorporation times are considered. In particular, in the top part of the figure (panel (a)), three profiles at different times, but with the same volume, are reported as obtained by changing the magnitude of the external supply of material. A large supply corresponds to out-of-equilibrium conditions, as there are more adatoms on the surface to be incorporated in the crystal. Indeed, in this condition the kinetic term can determine a faceting of the profile. On the contrary, when the incoming material is reduced, the growth is closer to equilibrium and a more rounded shape is obtained, lowering the isotropic surface energy of the system with only a minor influence of the incorporation dynamics. A similar trend is found when changing the magnitude of the incorporation time. Indeed, when the incorporation is slower, the redistribution of material is strongly affected by the incorporation dynamics, thus driving the kinetic faceting. But when the incorporation becomes faster, the differences in the adatom densities become negligible, therefore the material flows according to the minimization of the surface energy. More precisely, the balance between the kinetic and energetic contribution is given by the ratio $\mu_{\text{eq}}/(\tau v) = (\kappa\gamma)/(\tau v)$. Therefore, it depends on the actual profile due to the local curvature κ. Indeed, the high curvature regions tend to be rounded by the surface energy minimization, resulting in a locally smooth profile despite the overall crystal is faceted by kinetics. This can be observed in the intermediate profile of Fig. 2.8(b), where a square-faceted shape is obtained, still with a significant rounding at the vertices. The curvature relates to the local curvature radius as $\kappa = 1/R$, meaning that this property is scale dependent. Therefore, when considering a larger particle, the corner rounding is limited to a smaller region, comparable with the curvature radius which can balance the kinetic tendency to develop a faceted corner. For instance, if the profiles of Fig. 2.8 were considered at an much larger scale, they would present wide faceted areas, with rounded corners limited to a minor region of the crystal.

The competition between thermodynamics, related to the surface energy term, and kinetics, which accounts for the incorporation dynamics, can be illustrated for the more realistic case where anisotropic surface energy is modeled. If we consider the case where the τ maxima coincide with the γ minima, both energy terms concur in the faceting of the profile, with a time scale which is eventually influenced by the incorporation time. Vice

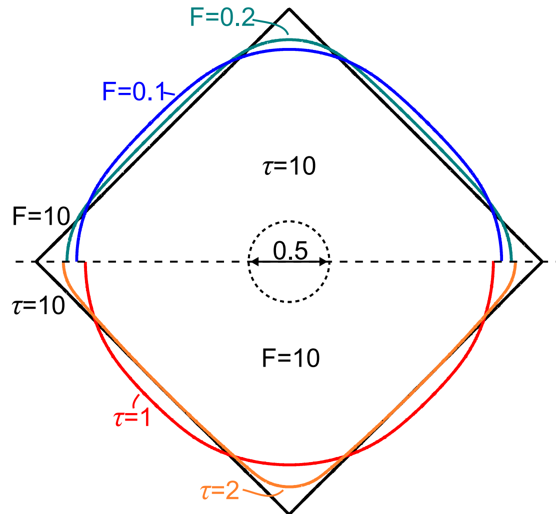

Figure 2.8: Comparison of the out-of-equilibrium conditions needed for the kinetic faceting. (a) profiles obtained for increasing deposition flux, $\tau_{11} = 10$. (b): profiles for increasing τ_{11}, $F_0 = 10$. All the profiles have the same volume, and the initial stage is a circle. $M_0 = 0.1$. (from Ref. [110])

versa, if the expected facets due to γ or τ differ, a competing dynamics can be obtained, where the faceting is determined by the relative strength of the two contributions to the chemical potential μ. To provide an example via PF simulations, we consider a $\gamma = \gamma(\hat{\mathbf{n}})$ with deep minima along $\langle 1\,0 \rangle$ directions dominating the ECS, while τ has maxima in the $\langle 1\,1 \rangle$ directions, where γ has only shallow minima, as it is shown in Fig. 2.9(a). If the τ/γ ratio is small enough, the main driving force is the energy minimization, which redistributes the incoming material according to the surface energy anisotropy. Therefore, the profile tends to the ECS by exposing the most stable $\{1\,0\}$ facets, despite their fast incorporation rate, as shown in Fig. 2.9(b). Vice versa, when the τ/γ ratio is increased, the morphology evolution is driven by kinetic contributions. This reduces the formation of the most stable $\{1\,0\}$ facets in favor of the slower growing $\{1\,1\}$ ones. As a consequence, a rotated $\{1\,1\}$-faceted squared profile is found in the simulation shown in panel (d), even if this requires a higher surface energy than the corresponding ECS morphology. However, it is important to remember that, whether the material supply is interrupted and the surface diffusion dynamics occurs in quasi-equilibrium conditions, the ECS shape is recovered, just with a minor influence of the anisotropic τ in the kinetic pathway toward surface energy minimization.

So far we have just considered orientation-dependent material properties in the definition of the chemical potential. Nevertheless, also the material supply can be anisotropic $F = F(\hat{\mathbf{n}})$. This is true for instance for the KCS modeling, when the faceting is purely determined by an orientation dependent material supply. The advantage of the kinetic model here proposed is the capability of tackling this anisotropic supply combined with the material redistribution dynamics at the surface, as driven by the incorporation times τ. This is shown in Fig. 2.10, where $\tau(\hat{\mathbf{n}})$ and $F = F(\hat{\mathbf{n}})$ are both considered, as sketched in panel (a), under the assumption of isotropic surface energy for the sake of simplicity. The simplest configuration is when maxima in τ coincide with minima of F. In this case both these

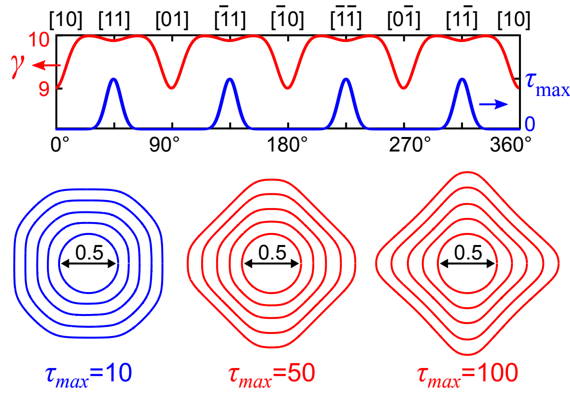

Figure 2.9: Competing role of incorporation time and surface energy anisotropy. For larger τ (center and right) the kinetic faceting dominates over the thermodynamic one resembling the ECS (left). Corner regularization is used with $\beta = 0.05$, while the anisotropy functions for $\tau(\hat{\mathbf{n}})$ and $\gamma(\hat{\mathbf{n}})$ are plotted in the top panel. (from Ref. [110])

contributions drive the same faceting, as it results in panel (b). On the contrary, when the two anisotropies are different, the evolution of the crystal is no more simple to predict. In particular, we set the two anisotropy function as out-of-phase by 45°. In the most unbalanced case shown in panel (c), where the material supply is sufficiently anisotropic, the crystal exposes the facets where the deposition is lower, in a similar way as predicted by the KCS. This is because the fast deposition hinders the material diffusion on the surface, thus making the effect of the kinetic redistribution of material negligible. Only a small trace of diffusion from the $\{1\,1\}$ vertices to the $\{1\,0\}$ facets can be hardly distinguished, but it is still too weak for altering the shape evolution. However, if the F/M ratio is reduced, it is possible to enhance the transfer of material on the surface, before it is incorporated into the bulk phase due to the subsequent deposition. In this condition, a faceting as driven by the incorporation times can become apparent, as described by Fig. 2.10(d). In the initial evolution stages, the $\{1\,1\}$ facets, corresponding to τ maxima, are clearly recognizable despite corresponding to the F maxima, suggesting a kinetic-driven faceting. However, the diffusion length is particularly limited by the additional material supply. This becomes important when the particle grows in size, and the diffusion is no more capable of covering the whole surface. As a result of the reduced material distribution, the anisotropy of the deposition becomes dominant and switches the faceting for the $\{1\,1\}$, driven by the incorporation times, to the $\{1\,0\}$, promoted by the external supply, as it is evident in the later stages of the evolution. Still, a small broadening due to the local diffusion is present at the $\{1\,1\}$ corners, which try to keep the slower incorporating facets. This effect is less apparent when the particle grows in size, as it is limited to the diffusion length. Therefore, we can conclude that the faceting due to orientation-dependent incorporation times τ plays a major role for particle sizes as small as the diffusion length. On the contrary, for larger sizes, the faceting is more likely determined by the anisotropic material supply, as predicted by the KCS theory.

Finally, it is worth noting that the balance between the different contributions driving the faceting holds on a local scale, so that the same growing system may behave differently from one region to the other. This is not unusual if one considers directional deposition [129,

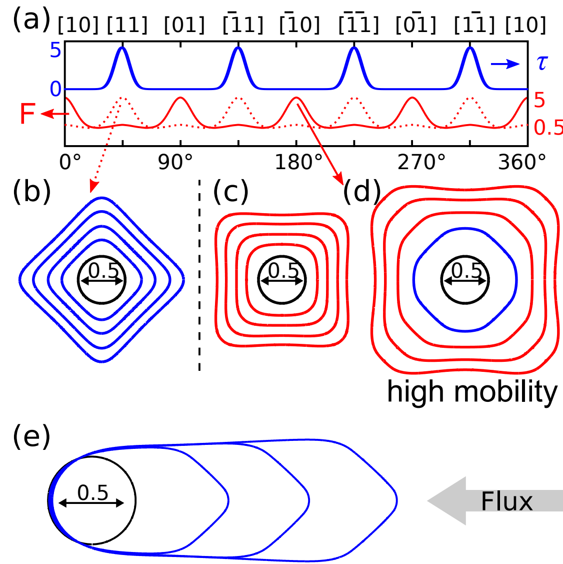

Figure 2.10: Combination of anisotropic incorporation time and material supply. (a) Plot of the $F(\hat{\mathbf{n}})$ and $\tau(\hat{\mathbf{n}})$ anisotropy functions used. (b) Both anisotropies lead to the $\{1\,1\}$ square (M_0=0.001). (c) The flux anisotropy is rotated by 45° (dotted line in panel (a)) and imposes $\{1\,0\}$ faceting (M_0=0.001). (d): the mobility is increased (M_0=0.007), while keeping the opposite anisotropies for flux and kinetics as in (c). (e) The flux $F_0 = 5$ is directed on one side of the crystal, following the arrow. (from Ref. [110])

130] or shielding effects [116, 131] with material supplied only on a certain portion of the crystal and possibly diffusing on other regions. To illustrate this situation, in Figure 2.10(e) the evolution of an initially circular profile with material supply only from the right-hand side is considered. This could resemble, for example, the cross section of a nanowire, where the deposition of the shell is performed selectively on just one side of the sample [132]. As expected, the growth proceeds asymmetrically, with more material accumulation on the right side. Kinetic faceting is obtained there as the deposited material is redistributed on the surface according to the different incorporation times. On the left side, where no material is deposited, a small amount of material flows by surface diffusion under the influence of the thermodynamic driving force that tends to favor the formation of a rounded profile of larger radius, due to the isotropic γ and the additional deposited material. Then, on the same crystal, a morphology faceted by kinetics and one rounded by the surface energy minimization can coexist in peculiar growth conditions.

2.2.3 Applications to pillared structures

In the previous section, we have shown that the kinetic faceting requires an out-of-equilibrium condition, as guaranteed for example by a deposition flux, and does not correspond to the minimum energy configuration. Post-growth, high-temperature processes, such as the annealing, could drive further changes in the crystal shape, still under the influence of the incorporation kinetics (see Ref. [112]), but directed toward the ECS. The model discussed here finds a direct application to several experimental systems where out-of-equilibrium growth conditions return peculiar faceting different from both the ECS and the KCS. To

confirm this, here we show an example of a real experimental system where it is relevant to consider the incorporation dynamics in order to capture the main feature of the growth process.

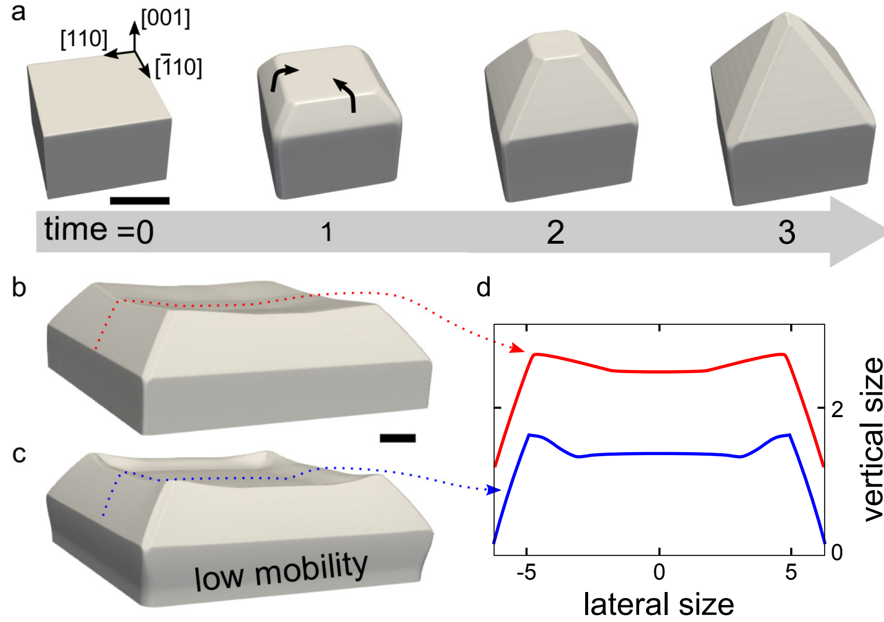

Figure 2.11: (a) Time evolution of a pillar top with competing incorporation times for the top (001) and the lateral {111} and {110}. (b-c) Comparison of the growth on a 4-times larger base for two different mobility coefficients ((c) 10 times smaller). (d) Comparison of the central (110) cross-sectional profiles, shifted arbitrarily in the vertical direction. The flux $F_0^* = 0.5$ is vertical, $\tau_{110} = \tau_{111} = 10$, $\tau_{001} = 1$. The scale bar is 1.5 length units. (from Ref. [110])

In Figure 2.11 we simulate the growth of a faceted crystal by 3D PF simulations. The initial shape is set as a simple parallelepiped, laterally bounded by {1 1 0} planes and terminated by a (0 0 1) top facet. This resembles the actual condition of experiments where the flat substrate is patterned by lithographic techniques before performing the growth. Incorporation times are assumed to be maximum for the {1 1 0} facets and for {1 1 1} planes, with τ_{001} one order of magnitude smaller. This choice is reasonable as a vertical growth is aimed to be simulated. Accordingly, a vertical deposition flux oriented along the $[0\,0\,\bar{1}]$ direction is taken into account. Figure 2.11(a) reports the growth sequence starting from a small base structure. Since the early stages, {1 1 1} facets nucleate and tend to grow larger with respect to the top (0 0 1) surface. This, having a faster incorporation time, tends to collect material from the surrounding surfaces, and it also receives more deposition flux. Therefore it tends to grow faster along the vertical direction, shrinking up to producing a pyramidal tip. This process is not linear in time, similarly to what discussed in Fig. 2.6, as the volume transferred toward the top increases as the lateral surfaces grow in area. Panel (b) shows an intermediate growing stage obtained for the same conditions as in panel (a), but for the initial parallelepiped shape, which is larger than the one in panel (a). Reasonably, the larger sizes lead to a delay of the closure of the {1 1 1} pyramid, requiring a greater amount of material to diffuse onto the (001) top. Moreover, the lateral size of this structure is larger than the diffusion length. As a result, the material transferred from the {1 1 1}

facets to the borders of the top (0 0 1) cannot spread all over the surface area, as it was for the case in panel (a). Therefore, it produces an overgrowth close to the edges of the top facets, producing mounds along the (0 0 1) perimeter. This phenomenon is enhanced in the condition of lower mobility shown in panel (c), where the diffusion length results to be even smaller. This is better compared in panel (d), where the profile is traced in cross-section along the [1 1 0] direction, highlighting as the formation of the mounds is more pronounced as the diffusion length is reduced with respect to the lateral size of the structure. These simulations closely compare with the experiments of micro-crystals growth on pillar-patterned substrates reported in Refs. [116, 133–135] and provide a deeper insight on the possible mechanisms responsible for the observed temperature dependence of the crystal morphology, changing from nearly planar at low temperature to pyramidal at higher temperature. Indeed, the pyramidal shape can be achieved only when the diffusion length is sufficiently long to cover the whole surface of the crystal, which is the case of an high temperature growth. The consistency of the simulation with the experimental evidences, particularly for the correct representation of the overgrowth at the top facet, confirms the importance of considering the present kinetic approach to reproduce the faceting of crystals in particular growth conditions, when both the surface diffusion and the incorporation dynamics play a role.

2.3 Modeling the kinetic growth of vertical nanomembranes

Membranes at the nanoscale are emerging as a new class of nanostructures, applied for instance to the integration of horizontal III-V nanowires [100]. In order to improve the development and the application of these novel nanostructures, it is important to assess which is the growth mechanisms that allows for such an anisotropic growth, leading to the formation of the membrane. In particular, the correlation between the growth dynamics and the substrate patterning could provide a strategic tool to target the growth of nanomembranes (NM). Therefore, in this Section 2.3 we focus on the development of a theoretical model to study this peculiar growth dynamics, with the aim of highlighting the main features of the growth process, which could be useful to guide future growth experiments. For the sake of simplicity, here we focus on an homoepitaxial growth, neglecting any elastic effect on the growth dynamics. A more comprehensive model tackling both surface diffusion and elastic contributions, due to the heteroepitaxial growth, will be discussed in Chapter 6.

2.3.1 Introduction to SAE growth of GaAs nanomembranes

Selective area epitaxy (SAE) is a widely used technique to drive the growth of nanostructures that cannot be obtained by direct-deposition onto a bare substrate. Confinement of the growth within openings defined in the oxide mask, which covers the substrate, by top-down patterning imposes particular constraints on the growth and development of the resulting structures, possibly leading to interesting morphologies. GaAs nanowires have been successfully obtained on (1 1 1)B GaAs and Si substrates by Metal-Organic Chemical Vapor Deposition (MOCVD) [87, 136, 137], by opening apertures in the oxide layer with

widths on the order of 100 nm. By extending the slits in the $\langle 1 1 \bar{2} \rangle$ direction up to several microns, vertical nanomembranes (NMs) are obtained, as reported in the literature for both MOCVD [99, 103] and MBE [98]. These NMs have shown to exhibit exceptional optical properties, as a consequence of their perfect crystal structure and absence of twinning defects [138], a feature that prevents also the occurrence of twinning-driven tilting, as in the case of nanowires [139]. In addition, it was recently demonstrated that these NMs can act as templates for the growth of horizontally aligned InAs nanowires [100]. The approach is wafer-scalable, opening the path towards integration of III-V nanowire networks on a chip, and providing a platform for the realization of advanced concepts in the next generation computing schemes [140].

A scanning electron microscope (SEM) image of a typical array of GaAs NMs is reported in Fig. 2.12. The majority of the NMs is defined by $\{1 1 0\}$ facets with a $(1 1 1)$B faceted top. Small $\{1 1 3\}$ facets are also recognizable at the sides of the top facet. Based on first principle surface energy calculations [141], the absence of $\{1 1 1\}$A facets looks reasonable for the As-rich growth conditions exploited here (V/III ratio $\sim$10), while the absence of $\{1 0 0\}$ facets contrasts with the expectation from the equilibrium Wulff shape of GaAs, as their surface energy should be still favorable. Moreover, the prominent tendency toward vertical growth, yet preserving the narrow cross-section initially enforced by the oxide slit, disagrees with the thermodynamic criterion of surface energy minimization. As we show here, indeed, the growth of the NMs is primarily driven by kinetics. In contrast to equilibrium conditions, the kinetic growth regime is not yet fully understood, as almost nothing is known about the different incorporation dynamics on the crystal facets, even for common low-index facets. Still, these differences greatly affect the evolution of the growing crystals, resulting in facet growth velocities that may vary even by a couple of orders of magnitude.

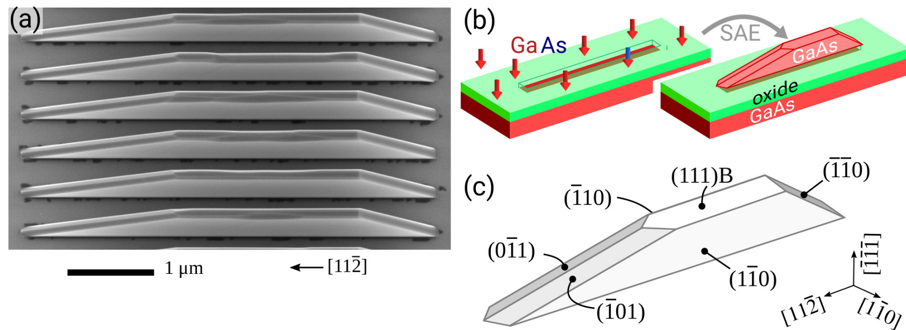

Figure 2.12: Growth of $[1 1 \bar{2}]$-oriented vertical NMs. (a) SEM view of a typical array of NMs grown by Molecular Beam Epitaxy on $(1 1 1)$B GaAs substrate (b) Schematics of the Selective Area Epitaxy procedure. (c) Schematic drawing of a NM shape obtained with the minimal set of $\{1 1 0\}$ facets and the $(1 1 1)$B top facet. (from Ref. [142])

Modeling facet-dependent growth kinetics by exploiting atomistic approaches is extremely challenging, not only due to the lack of microscopic-scale parameters, but also because of severe limitations in both spatial and temporal scales. We have, therefore, devised a "reverse-engineering" strategy, based on continuum modeling, to extract quantitative information about key parameters, such as the incorporation times for the different crystal facets. First, we considered new experiments by performing the growth on circular arrays, as obtained

by rotating the rectangular growth slit around a given center on the (1 1 1)B substrate, similarly to the work of Ref. [101]. Second, we applied a state-of-the-art continuum growth model, incorporating the main kinetic contributions, so that the experimentally-observed morphological changes of the NMs as a function of slit orientation could be compared with simulation results. All the growth experiments and the measurements have been performed by the group of Prof. Fontcuberta i Morral at École Polytechnique Fédérale de Lausanne.

2.3.2 Experimental details

The GaAs nanoscale membranes are grown by MBE. The substrate is prepared with a standard procedure for SAE as in Ref.[98]. First, a layer of 30 nm SiO_2 is deposited onto a 2-inch (1 1 1)B GaAs substrate by Plasma-Enhanced Chemical Vapor deposition (PECVD). The resist, ZEP 5250, is then spin-coated on the SiO_2 layer which in turn is exposed to the electron beam lithography process to define the pattern. The apertures in the oxide are obtained by dry-etching with a mixture of CH_3F/SF_6. The final removal of the resist is carried out by 10 min of oxygen-plasma, followed by acetone and IPA cleaning. Before being grown, each sample is annealed and degassed at 350 °C in ultra-high vacuum conditions. The growth conditions of the nanoscale membranes have been optimized, resulting with the following parameters: temperature between 625 and 635 °C and V/III equivalent beam flux ratio of 10, with a gallium growth rate fixed to the nominal value of 1 Å/s which corresponds to a partial beam equivalent pressure of 2.5×10^{-7} Torr.

2.3.3 Kinetic model details

The continuum model developed by J.W. Cahn and J.E. Taylor in Ref. [15], and presented in the Section 2.2, is exploited to study the growth of the GaAs NMs. This is numerically implemented within the phase-field approach (PF) [10, 113], which is very effective in simulating complex, three-dimensional structures. The crystal morphology is traced implicitly by means of the PF function φ, with value 1 into the crystal and 0 in the surrounding vacuum region, as shown in Fig. 2.13(a). The surface profile, as defined in the following figures, is then identified as the φ=0.5 isoline in the diffuse-interface region (of width ϵ) where φ goes smoothly from 1 to 0. The whole substrate region out of the oxide slit, corresponding to the bottom boundary of the simulation cell, is assumed to be covered by oxide as for SAE, thus resulting in a non-wetting contact condition for the GaAs crystal, according to Young's law (see Fig. 2.13(b)). This is implemented by accounting for the interface energy contribution for the crystal-oxide interface, represented by a boundary of the simulation domain. In principle, the total energy of the system can be written as $G_{tot} = G_{CV} + G_{CS} + G_{CO} + G_{VO}$, where G_{CV} is the free energy of the crystal-vacuum interface that we have considered so far, G_{CS} is the energy of the interface between the growing crystal and the substrate, which in homoepitaxial conditions is equal to zero, G_{CO} is the energy cost of the interface between the crystal and the oxide surface and G_{VO} is the energy of the interface between the oxide surface and the surrounding vacuum environment. According to the Young's law, following the principle of free energy minimization, the contact angle θ at the crystal-oxide interface can be expressed as $\cos(\theta) = \frac{\gamma_{VO}-\gamma_{CO}}{\gamma_{CV}}$, where

$\gamma_{\dots}$ represents the energy density for the corresponding interfaces. These assumptions can be modeled numerically in the PF approach by adding a boundary condition on the oxide surface [143]. In particular, in the following simulations, we have set $\theta = 170°$ on the oxide surface, to hinder the overgrowth of the crystal on the oxide surface. In all other boundaries of the simulation domain, zero-flux Neumann boundary conditions are applied.

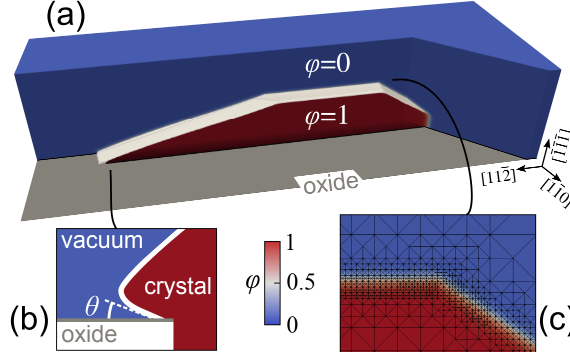

Figure 2.13: PF model used to simulate the growth of NMs. (a) Simulation cell tracing the NM geometry by the φ function, valued 1 in the crystal and 0 in the vacuum. (b) Schematics of the non-wetting contact angle boundary condition for GaAs on the oxide region. (c) Enlarged view of the simulation cell cross-section at a NM vertex showing the adaptively-refined mesh, finer at the diffuse interface in between the crystal and the vacuum phases. (from Ref. [142])

In principle, the GaAs growth needs both Ga and As to proceed. However, here we explicitly consider just the dynamics of Ga adatoms on the surface profile. Indeed, although As is expected to play a role in the growth dynamics [144], we assume that the As supply from the gaseous phase is not a limiting factor in case of high V/III ratio, as for the experiments that will be presented here. The kinetic reaction at the surface between As and Ga is implicitly considered in the effective incorporation rate of Ga into GaAs that we explicitly quantify in the model.

In order to model the orientation-dependent incorporation kinetics, following Ref. [127] we introduce the continuum function

$$\tau(\hat{\mathbf{n}}) = \tau_0 \sum_i \tau_i (\hat{\mathbf{n}} \cdot \hat{\mathbf{m}}_i)^w \cdot \Theta(\hat{\mathbf{n}} \cdot \hat{\mathbf{m}}_i), \tag{2.8}$$

summing the values of the maxima τ_i for the $\hat{\mathbf{m}}_i$ orientations of the crystal facets. In particular, the ones recognized experimentally in the fin structures, i.e. $\{1\,1\,1\}$, $\{1\,1\,0\}$ and $\{1\,1\,3\}$ will be considered. τ_0 is a scaling factor and w controls the width of each maximum. The latter is set equal to 200 in order to control $\tau(\hat{\mathbf{n}})$ independently for each $\hat{\mathbf{m}}_i$ orientation, while avoiding the overlap of different contributions for orientations in between. Opposite facets are distinguished thanks to the signed Heaviside function Θ, permitting to assign different τ values to A- and B-type facets. For all other orientations, i.e. the edges between the facets, $\tau(\hat{\mathbf{n}})$ smoothly falls to 0, thus implying instantaneous incorporation to keep them out of the growing shape.

The set of simulation parameters is defined in order to obtain a good correspondence with the experimental observation. In order to provide a proper resolution for the PF

interface, a value of $\epsilon = 25$ nm is set, and the mesh is locally refined up to ∼5 nm. Moreover, since the facet edges are regions of fast incorporation, they can become very sharp and thus might exceed the mesh resolution. To prevent this numerical issue, a regularization procedure is implemented by temporary raising $\tau(\hat{\mathbf{n}})$ on such critical mesh points. A typical deposition rate of 0.7 Å/s is set for the (1 1 1)B plane with beam incidence at 45°, in the range of our experimental conditions.

Since the dynamics of material redistribution is governed by the relative values of γ, the kinetic factor τ_0, and M_0 [112], by assuming $\gamma = 4.5$ eV/nm^2, as for {1 1 0} facets [141] (the ones dominating the nanomembrane shapes), we set τ_0 and M_0 in order to match the experimental behavior. In order to enforce a growth regime dominated by kinetics, μ_{eq} must be much smaller than the kinetic contribution in μ: this was achieved by setting τ_0 = 0.022 (eV·min)/nm^4 (a factor kT/V_{at} with T the temperature and V_{at} the volume per atom is included). To define M, we consider that homogeneous material distribution within each facet is obtained if the adatom diffusion length λ is of the same order of magnitude of their extension, i.e. $\sim \mu$m. By considering that $\lambda \sim \sqrt{2M\tau}$, we set a value of $M_0 = 1.2{\times}10^8$ nm^6/(eV·min) ($M_0 \sim V_{at}D/kT$, with D the diffusion coefficient). Finally, by a best-morphology-fit procedure, we set $\tau_{110}/\tau_{111B} = 10$ and $\tau_{113}/\tau_{111B} = 2$, as discussed in Section 2.3.4, with $\tau_{111B} = 1$.

Modeling of the deposition flux in an MBE growth

The material supply in the PF model is quantified by the operator $F(\hat{\mathbf{n}})|\nabla\varphi|$ in the evolution Eq. (2.4). $F(\hat{\mathbf{n}})$ is the nominal deposition rate, which is restricted at the crystal surface by $|\nabla\varphi|$, which is non-zero only within the diffused interface region.

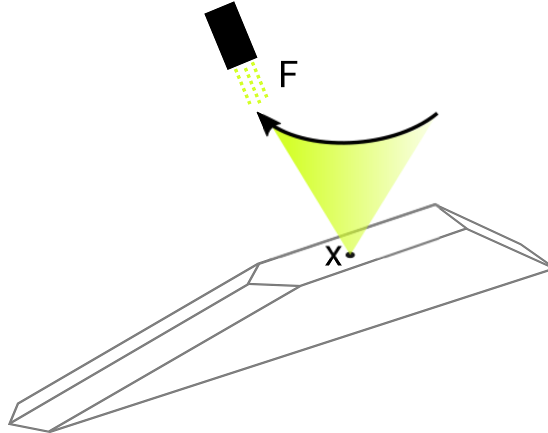

Figure 2.14: Schematics of the distribution of the flux F which rotates with respect to the substrate. A conical flux can be modelled to imping on each point of the surface.

The quantity of material that impinges on the crystal surface is determined both by the properties of the deposition flux and by the orientation of the surface itself [135]. Indeed, in a typical MBE growth, schetched in Fig. 2.14, the distribution of the flux is not uniform on each point of the surface. This is mainly because the flux has a well defined angle with respect to the normal to the substrate. Therefore the projection of the flux on the differently

oriented surfaces corresponds to an orientation-dependent material supply. In addition to that, the substrate holder rotates with respect to the growth chamber during the growth, so that each facet collects the projection of the entire deposition cone which is described by the flux during a rotation period. Therefore, to compute the material which is deposited on each point $\boldsymbol{x}$ of the surface, by considering a full sample rotation, the projection of the flux along the surface normal has to be integrated over all the possible flux orientation:

$$F(\hat{\mathbf{n}}) = \frac{F_0}{2\pi \cos\theta} \int_{\Omega} \hat{\mathbf{r}}(\psi, \theta) \cdot \hat{\mathbf{n}} \, d\psi \tag{2.9}$$

with F_0 the material flux coming out from the MBE source, θ the inclination of the source with respect to the substrate normal (which we set at 45° according to the experimental setup) and Ω the domain of integration for the directions $\hat{\mathbf{r}}(\psi, \theta)$ for the flux, considering a full rotation of the sample, where ψ is the azimuthal coordinate. It is important to notice that, depending on the facet inclination α with respect to the substrate surface, the facet itself may shield part of the incoming flux, during the rotation of the sample. As a consequence, three different cases can be distinguished. When $\alpha < 90° - \theta$ the facets receive material during the whole rotation and $F(\hat{\mathbf{n}}) = F_0 \cos(\alpha)$ by integrating in $\Omega = \{\psi \in [0, 2\pi]\}$. On the contrary, if $\alpha > 90° + \theta$, then no material impinges on the facet due to a self-shielding of the flux and $F(\hat{\mathbf{n}}) = 0$. For the intermediate case, $\Omega = \{\psi \in [\psi^*, 2\pi - \psi^*]\}$ with $\cos\psi^* = \cot(\alpha)\cot(\theta)$, so that the solution of the integral is $F(\hat{\mathbf{n}}) = F_0[\cos(\alpha)(1 - \psi^*/\pi) + (1/\pi)\sin(\alpha)\tan(\theta)\sin(\psi^*)]$.

Flux shielding effects on the NM sidewalls by neighboring structures [131] are not considered. We also neglect Ga supply from the oxide region. The good correspondence between the simulated and experimental crystal morphologies (see Section 2.3.4) justifies these simplifications a posteriori.

2.3.4 Simulation results and comparison with experiments

The vertical growth of GaAs nanomembranes is here investigated by a close comparison between the experimental data and numerical simulation. At first, an initial analysis of the experiments is required to figure out which are the main features of this dynamics, trying to isolate the most peculiar properties of this system. Among these, an initial guess of the possible growth mechanisms is done, in order to have a first guide for the setup of the phase-field model. To this purpose, we focus on the better defined system, where NM are grown in oxide windows extending along the $\langle 1\,1\,\bar{2}\rangle$ direction. The comparison between PF simulations and the corresponding experimental morphologies, even at different deposition times, enables to define the model setup and in particular to estimate the kinetic parameters for the main facets involved in the growth process. Once the model has been successfully applied to the test case, a variety of morphologies can be analyzed. In particular, the experimental growth over a particular substrate, which is patterned by several slits aligned along a circular pattern, provides a wide set of morphologies. The common point is that all the different fin shapes have been achieved with the same growth conditions. Therefore, this represents an ideal case that allows to validate the model by comparing several simulation

result with the SEM data, still with the same set of numerical parameters.

Kinetic growth of $\langle 1\,1\,\bar{2}\rangle$-oriented vertical nanomembranes

The main characteristics of the growth dynamics can be found by analyzing several stages of the growth. As no technique is available for a precise morphological in-situ analysis of the vertical NM, the only choice is to compare different samples with the same pattern and growth condition, but a different deposition time. In this way, a time evolution can be deduced from the SEM images. To this purpose, the reference case of a NM aligned along $\langle 1\,1\,\bar{2}\rangle$ is analyzed. This is mainly because the highest uniformity among fin in the same pattern and, in particular, among samples from different growth can be achieved for this specific orientation.

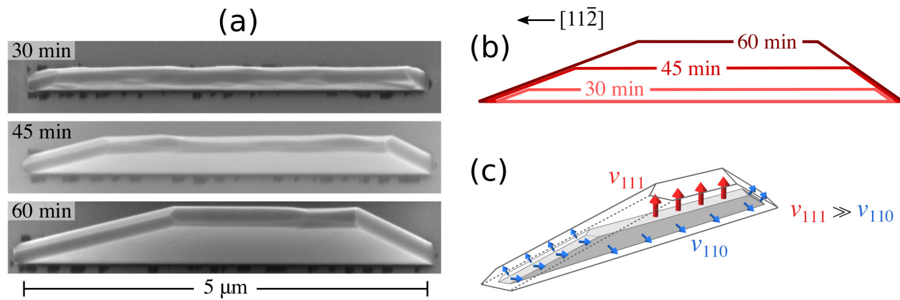

Figure 2.15: Assessing the facet growth rates in $\langle 1\,1\,\bar{2}\rangle$-oriented vertical NMs. (a) SEM perspective views of a single NM grown after 30, 45 and 60 min of GaAs deposition. (b) Lateral profiles drawn for the three stages of panel (a). (c) Schematics of the facet growth by assigning different velocities v for the $\{1\,1\,0\}$ and $(1\,1\,1)$B facets forming the NM. The velocity of the $(1\,1\,1)$B, v_{111B}, is deduced to be much larger than the one of $\{1\,1\,0\}$ facets, v_{110}, according to the experimental findings. (from Ref. [142])

The SEM perspective views resulting from this analysis are reported in Fig. 2.15(a) for 30, 45 and 60 min deposition times. The morphology that develops out of the oxide window, by considering a side view, seems to grow as a trapezoid which shrinks its top base while growing in height. This behavior is sketched in panel (b), for the three times here considered. The first conclusion that we can get from this first simple analysis is that most of the material that is deposited on the fin is transferred toward the top. Indeed, the other fin dimensions, i.e. the width and the length, grow much slower than the height. By looking at the inclination of the facets with respect to the substrate $(1\,1\,1)$B surface, and by considering the main sets of facets for the GaAs crystal, we can deduce that the top growth front is mainly composed by a $(1\,1\,1)$B facet, while the lateral sides are made of $\{1\,1\,0\}$ facets. Two vertical facets are on the main sides, two slanted on the front of the NW and a single slanted one on the back. By a quantitative measurement of the thickness and height variation of the fin, the ratio between the growth velocities for the two set of facets v_{111B}/v_{110}, sketched in panel c, can be even of the order of 50 times. This conclusion was obtained by measuring the facets width from a SEM top view and by reconstructing the fin shape with $\{1\,1\,0\}$ and $(1\,1\,1)$B planes, in order to have the same trapezoidal shape observed experimentally. Such a strong difference is necessary to determine a vertical growth, which

otherwise would lead to a more isotropic, i.e. spherical, shape as we will demonstrate in the following.

The analysis of the geometrical shape of the NM and its time variation highlights the role of the strongly different growth rates for the two main sets of facets. However, this is not sufficient to present a complete picture of the growth dynamics. A faster growth front corresponding to the {1 1 1}B facet is observed also in other cases of GaAs heteroepitaxy [87, 145], especially for the case on nanowires grown by SAE. However, the large difference with the speed of the other set of {1 1 0} observed in the present system still requires a careful explanation. The first try to explain the growth dynamics can be done by considering thermodynamic arguments. This implies to adopt a model based on a close-to-equilibrium dynamics. The material which is deposited on the GaAs surface is able to diffuse according to the tendency toward surface energy minimization [127]. The incorporation times for the diffusing adatoms are considered instantaneous, which means that the adatom phase is locally in dynamic equilibrium with the crystal surface.

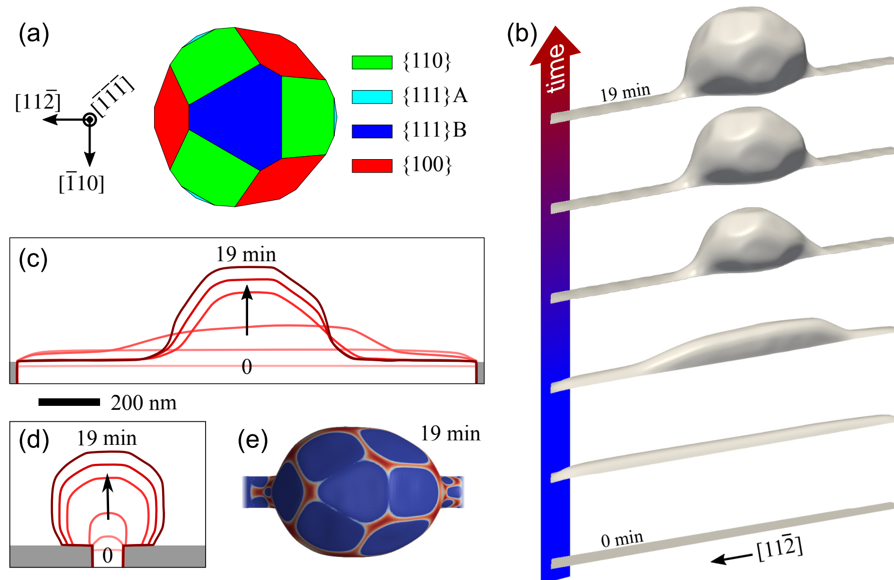

Figure 2.16: Growth by deposition and surface diffusion with anisotropic surface energy, but no incorporation kinetics. (a) Equilibrium Wulff shape according to the surface energy densities. (b) Time evolution for a 1.5 μm long oxide slit for the same deposition conditions and time scale used in the main text. (c) Longitudinal cross section evolution. (d) Transversal cross section evolution. (e) Top view of the rounded crystal structure formed in the latest stage of the simulation in panel (b), with faceting made more evident by color contrast between the planar facets (blue) and their edge regions (red). (from Ref. [142])

A GaAs crystal, in ideal annealing conditions with no material gain or loss, would evolve toward the ECS predicted by the Wulff construction [14]. This guarantees to minimize the anisotropic surface energy by exposing the different facets of the crystal with an area which is approximately inversely proportional to the corresponding energy density. The numerical values for the surface energy density can be obtained from the literature [141, 146] by considering As rich conditions, as the ones required by the experiments here considered. We choose to focus only on low-index facets, neglecting the {1 1 3} family for the sake of

simplicity. The resulting Wulff shape is reported in Fig. 2.16(a), where {1 1 1}B, {1 1 0} and {1 0 0} facets are clearly visible with a nearly equivalent surface area, while {1 1 1}A appear to be smaller. The relative size of the facets is in good agreement with what is expected from the single surface energy densities. Indeed, all the facet families have roughly the same value, apart from the {1 1 1}A which has an higher energy. However, this suggests that the surface energy densities cannot explain the formation of the NM vertical shape, mainly because the area of the different facets is clearly different. Moreover, no {1 0 0} facet is observed on the NM surface, at least with a sufficiently large area to be identified by SEM.

However, to be more precise, the experiments differ from the Wulff shape description for two main features. First, in the experiments there is a source of material, which is not included in the Wulff construction. Moreover, the growth of vertical NM is achieved by exploiting SAE, where the crystal can grow only within an elongated slit. Therefore, in principle it is not yet excluded that a thermodynamic model could properly reproduce the growth. Indeed, it could be that faceting is still driven by the differences in the surface energy densities, but the vertical growth is promoted by the source of material from the top, as in MBE, and by the lateral constraint imposed by the SAE in the oxide slit. However, this hypothesis is rejected by the results of the simulation reported in Fig. 2.16(b-d). In this case, the model accounts for the anisotropic surface energy, for the MBE distribution of the deposition flux and for the contact angle condition between the GaAs crystal and the oxide surface. The inital stage could resemble the one of a NM, where material collects into the oxide window up to its complete filling. However, as the deposition continues, a rounded shape is developed in the center of the oxide window. This shape presents also a significant overgrowth on the oxide, which is energetically balanced by the possibility to reduce the surface area by tending to a rounded morphology. The crystal shape, during the growth dynamics, exhibits a faceted geometry determined by the surface energy anisotropy. The faceting tends to converge to the one predicted by the equilibrium Wulff shape as the shape becomes more rounded, with a minor trace of the elongation guided by the oxide windows underneath. This is made more evident by comparing the Wulff shape in Fig. 2.16(a) with the top view of the latest evolution stage shown in panel (e). Therefore, it is possible to conclude that a pure thermodynamic growth regime is not sufficient to reproduce the NM growth dynamics, even if the surface anisotropy and the SAE in the oxide slit are considered. Indeed, the tendency to minimize the surface free energy leads to the formation of a rounded shape, collecting the material in the center and excluding the possibility to enable a vertical growth.

The material deposition in a MBE growth, in principle, could favor a vertical growth, as the top facets receive more material than the vertical lateral ones. However, it is not reasonable to explain the strong difference observed in the growth velocities just by the directionality of the deposition. An additional feature has to be introduced in the modeling to account for the significant difference in material incorporation which is observed between facets, with the idea that the growth has to be controlled by kinetic effects. Actually, literature studies [87] for nanowire growth by MOCVD already suggested that the As incorporation may be slower on {1 1 0} surfaces, inducing a lore growth rate with respect to

{1 1 1}B.

To overcome the modeling limitations of the thermodynamic description in reproducing the fin growth, we have to apply the kinetic contribution of the model, described in detail in Section 2.2. This enables to study the faceting dynamics as a result of the competition between deposition, diffusion and incorporation dynamics at the surface. This is achieved via the PF approach, which is well suited to simulate any morphological evolution, still considering the localized heteroepitaxy by SAE. Differently from a simple geometrical construction, as the one sketched in Fig. 2.15(c), in the present model the faceting is not imposed as an a-priory assignment, i.e. by imposing constant growth velocities to the facet planes. The faceted shape results spontaneously from the anisotropic properties of the material. The crucial simulation parameter to be set in this kinetic description is τ, the adatom lifetime before incorporation in the crystal, which in principle depends on the facet properties. Since the {1 1 0} and {1 1 1}B facets are the main ones recognized in experiments, we assume in a first approximation that the τ function has maxima on these two facets, while for all the other surface orientations it goes smoothly to zero, limiting the assumption for the adatom lifetime to the main facets. Based on the theory of kinetic crystal shapes, we expect that the facets with a lower incorporation time tends to grow faster, resulting in a shrinkage of their area with time. According to the analysis of the SEM data, we have already recognized that the growth velocity of the {1 1 0} is slower than the one for the {1 1 1}B . Therefore, we have to set $\tau_{110} > \tau_{111B}$ in order to favor the relative growth rate of the latter. In particular, the value of $\tau_{110} = 10\tau_{111B}$ is estimated by means of a best-fit procedure between the experimental morphologies and the simulation results. For the sake of simplicity, no surface energy anisotropy is considered in the model, meaning that all orientations are equivalent for the surface energy density. Indeed, as shown before, the surface energy minimization does not lead to the proper faceting, which could be achieved relying only on the tendency to growth facets driven by the kinetic contribution to the chemical potential.

The first case considered for the PF simulations is the growth of a vertical NM along $\langle 1 1 \bar{2} \rangle$-oriented slit. The time evolution sequence is reported in Fig. 2.17(a). The initial profile is set as an initial parallelepiped that fills the oxide window just below the oxide edge, before activating the crystal-oxide interaction. The oxide slit is set to be $1.5\times0.1\ \mu\text{m}^2$, mimicking the experimental pattern. The subsequent material supply enables the vertical growth of the NW which exposes a spontaneous faceting. The morphology is defined by the whole set of {1 1 0} facets, laying above the substrate surface, and by the (1 1 1)B facet on the top since the initial stages of the evolution. During the vertical growth, the trapezoidal shape observed in experiments is recognized in the simulation. The initial wide (1 1 1)B facet is reduced by the slanted {1 1 0} while growing vertically. Finally, the triangular shape bounded just by {1 1 0} facets is obtained, in agreement both with the simple geometrical description and with the experimental observation.

The mechanism responsible for the vertical growth can be better understood by looking at the adatom chemical potential at the surface, which is reported in Fig. 2.17(b). During the whole growth process, the absolute minimum of the chemical potential lies on the top

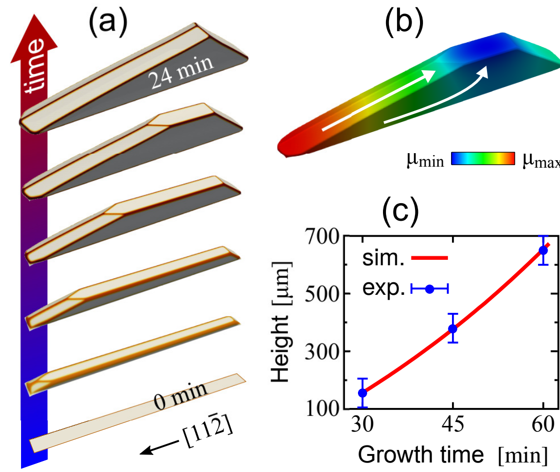

Figure 2.17: PF simulation results for vertical NMs. (a) Growth sequence of a NM in a 1.5 μm slit oriented along [11-2]. The deposited material tends to diffuse from the lateral {1 1 0} facets to the top (1 1 1)B, according to the gradient of the chemical potential μ, which is represented in the color map in panel (b). The white arrows sketch the flow of material on the surface. (c) Comparison of the NMs height between simulation (red line) and experimental data points, retrieved by SEM images, in the case of a 5 μm slit. The error bar represents the uncertainty in the measurements. (from Ref. [142])

(1 1 1)B surface. This corresponds to the facet with the fastest incorporation dynamics. Therefore material tends to flow from the other regions toward the top, as indicated by the arrows in Fig. 2.17(b), as for a Fick diffusion dynamics driven by a gradient of adatom density on the surface, which is induced by the different incorporation dynamics. However the growth speed of each facets does not depend directly on its incorporation time, but on the material supply provided by the neighbor facets. By assuming that desorption is negligible at the MBE growth temperature of 625 - 635 °C [147], the whole material supplied to the fin crystal is able to redistribute on the surface. Since its area becomes larger due to the vertical growth, more material can be collected from the deposition flux. As a result, the growth rate is not constant with time. In particular, the area of the {1 1 0} facets increases with respect to the one of the (1 1 1)B ones, therefore a larger volume of material is first deposited on the {1 1 0} and then transferred to the fin top. This behavior is highlighted by looking, in Fig. 2.15(c), at the plot over time of the fin height. The trend of the curve appears to grow exponentially, and the arbitrary time scale of the simulation was tuned to match the experimental one. This latter was measured by considering three different vertical NM grown for different times, and the error is related to the uncertainty to determine the height from the SEM images. The exponential trend, being recognized also in experiments, confirms the correct modeling of the non-constant growth rates that would be predicted by looking just at the incorporation times, but neglecting the material repartition between adjacent facets. Moreover, this comparison allows us to set a realistic timescale for the simulation, that will be applied with the same scaling for all the following numerical results of this section 2.3.4.

Once the main parameters have been tuned to properly reproduce the experiments, simulations can be applied to study the effect of the growth conditions on the evolution

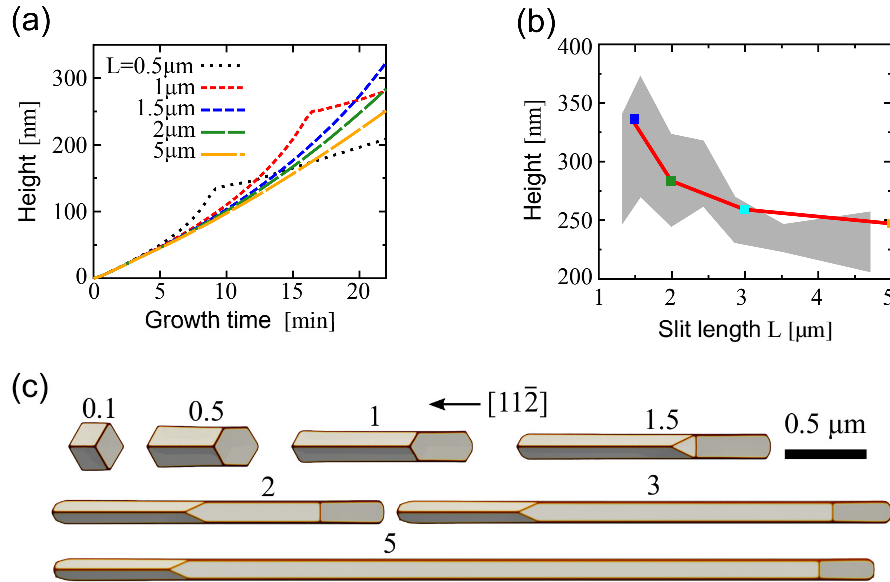

Figure 2.18: Comparison of the nanomembranes height for different lengths of the oxide slit. (a) Evolution in time of the NM height. The sudden variation in the slope observed for the cases of 0.5 and 1 μm corresponds to the disappearance of the top (1 1 1)B facet. (b) Comparison between the fin height predicted by simulations and the corresponding range of heights measured experimentally after 30 min deposition (grey band). (c) Top view of the simulated profiles (at 22 min) for the different labelled lengths. (from Ref. [142])

dynamics. For instance, here we inspect the growth by changing the length of the oxide slit, from 0.5 μm to 5 μm, while keeping the same width of 100 nm. The results of this analysis are reported in Fig. 2.18, where the height of the NM is studied as a function of time in panel (a), for the different slit lengths, and as a function of the slit length at a fixed time in panel (b). For this latter evolution stage, the top views of the NM are reported in panel (c), to show the relative amplitude on the top an side facets. In all cases, the (1 1 1)B facet shrinks while the {1 1 0} ones tend to close the shape leading to a triangular {1 1 0}-only faceted morphology. Due to the geometrical inclination of the facets, it is clear that shorter NM reach quicker the closing stage. The onset of the transition from a trapezoidal to a triangular shape is highlighted in panel (a) by the sudden change of the curves slopes, for the 0.5 and 1 μm long slits. Indeed, as soon as the fast-growing (1 1 1)B top disappears, the deposited material is spread nearly equally on the {1 1 0}, leading to a more isotropic growth of the facets at a slower growth rate. Apart from the small differences of material supply due to the MBE flux distribution, the growth is essentially self-similar, with a lateral expansion which is comparable to the vertical one. This is shown also by the top views in panel (c), where the largest NM corresponds to the shortest. In particular, for the 0.1 case which is grown on an square mask opening, a 3-fold symmetric pyramidal dot is found, mainly bounded by the three {1 1 0} facets that correspond to the back and front of the elongated NMs.

Furthermore, by looking at the different curves in Fig. 2.18(a), it is clear that the vertical growth follows different exponential curves, depending on the slit length. The longer is the fin, the slower is the vertical growth. Correspondently, by comparing the different NMs at

the same deposition stage as in panel (b), it is found that the shortest fins are taller than the most elongated ones. This behavior is compared to the experiments, reported by the grey band. These are collected for multiple samples after 30 min of deposition, and the width of the band corresponds to the variability of the experimental data. The important result is that both theory and experiments report the same tendency to reduce the height when growing a longer fin. This can be theoretically explained, in the framework of the present kinetic model, by considering that the material that flows form the lateral $\{1\,1\,0\}$ toward the top $(1\,1\,1)$B has to spread on a smaller surface area of the latter facets for the case of smaller NM, thus promoting the vertical growth direction.

Three-dimensional fin growth on a circular pattern

A deeper insight into the kinetic mechanisms driving the vertical growth of NW is provided by dedicated growth experiments, in which the slit orientation is changed with respect to $\langle 1\,1\,\overline{2}\rangle$ direction that has been considered so far. In particular, this allows us to test more accurately the validity of the description, and in particular of the generality of the incorporation times deduced by simulations. To this purpose, a circular pattern was designed to have a proper control of the angular dependence of the growth dynamics. It consisted of several slits etched in the oxide layer along a ring pattern, all pointing toward the center of the circle, with an angular distance of about 1°. By applying the same growth recipe as for the $\langle 1\,1\,\overline{2}\rangle$ slit case, 3D faceted fins are observed for the intermediate orientations, together with the previously analyzed vertical NM, as it is shown in Fig. 2.19(a). By the closer inspection in panel (b), it is possible to recognize a continuous change of the faceted morphology, from vertical to slanted NMs. These two limiting cases are shown more in detail in panels (c) and (d) respectively.

The vertical growth of NMs within $\langle 1\,1\,\overline{2}\rangle$-oriented slits appears with the same features described in the previous section, with the trapezoidal shape bounded by $\{1\,1\,0\}$ surfaces. A similar behavior is found for the slanted NM obtained for the $\langle 1\,1\,0\rangle$ oriented slits. These crystals in particular are shaped as isosceles trapezoids, still bounded by $\{1\,1\,0\}$, but with a more defected top. As shown in the zoomed view in panel (d), their sidewalls form an angle of ∼35° with the substrate surface, suggesting that their correspond to $\{1\,1\,0\}$ facets which both can match the inclination angle and can lay within the elongated oxide slit. As a first conclusion, $\langle 1\,1\,\overline{2}\rangle$ and $\langle 1\,1\,0\rangle$ orientations are the only ones on the $(1\,1\,1)$B plane to share the possibility to admit a pair of $\{1\,1\,0\}$ facets running along the slit length and forming the main sidewalls of the GaAs crystal. On the contrary, the closing top for the $\langle 1\,1\,0\rangle$ oriented NM is not well defined as for the vertical ones, as it presents an indented profile composed by $\{1\,1\,n\}$-like facets. Still, this morphology is compatible with the main aspect of the model developed so far, where a fast growth front leads to a directional growth of the crystal, while keeping the growth velocity of the $\{1\,1\,0\}$ facets much lower.

As a consequence of the crystal symmetry, on the $(1\,1\,1)$B substrate plane there are six $\langle 1\,1\,\overline{2}\rangle$ slit orientations available. These are alternated by six $\langle 1\,1\,0\rangle$ oriented slits, at 30° one from the other. However, even if the same fin morphology is found for each of the six orientations, the actual rotational symmetry of this system is three-fold. Indeed, the fin

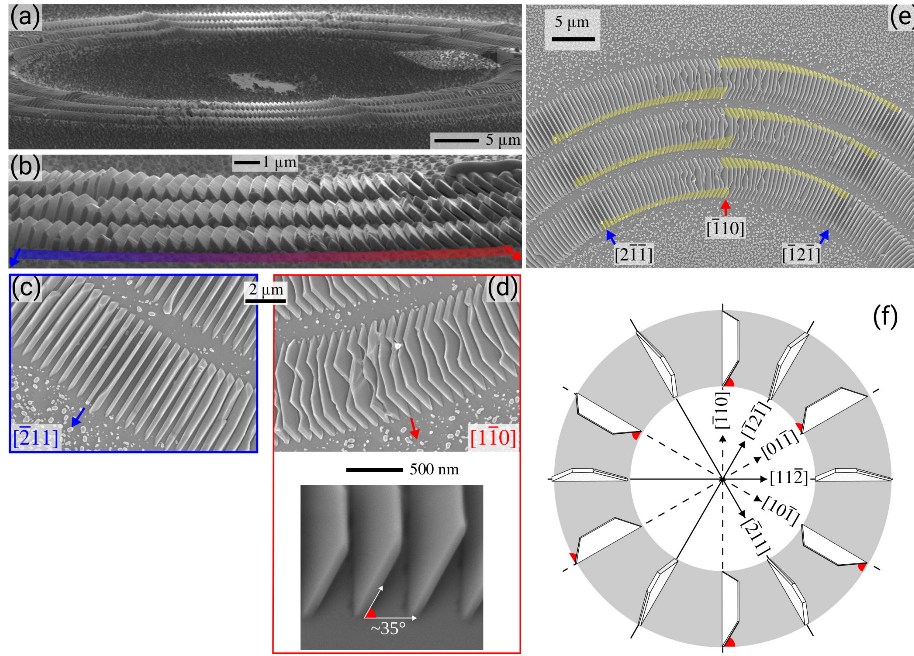

Figure 2.19: Fin growth on a circular pattern obtained by rotating the slit for every <1° after 60 min GaAs deposition. (a) SEM view of the whole patterned area showing selective growth into all slits. (b) Enlarged view of a 30° wide sector of panel (a) showing the continuous change in the NM morphology from vertical to slanted shapes. Top views of these two limiting cases are shown in panels (c) and (d) respectively. The actual inclination of the slanted NMs is made evident in the inset, showing an SEM image taken from the fin front. (e) SEM top view of a 30° sector in between successive $\langle 1\,1\,\bar{2}\rangle$ directions showing the exchange from inner to outer of the 110 back facet of the fin, colored in yellow. (f) Scheme of the three-fold repetition of vertical and slanted morphologies along the whole circle. (from Ref. [142])

front and back exchange from the inner of the ring pattern to the outer side when moving by 30° from one $\langle 1\,1\,\bar{2}\rangle$ direction to the next one, as for the $[2\,\bar{1}\,\bar{1}]$ and $[\bar{1}\,2\,\bar{1}]$ orientations. These switch of the fin orientation is shown in Fig. 2.19(e), where the yellow bands highlight the back of the fin shape.

This phenomenon occurs gradually through all the intermediate fin orientations. The process becomes precisely the reverse when a $\langle 1\,1\,0\rangle$ direction in between is reached. This is the case where the front and the back of the fin have the same shape. In a similar way, the direction to which the slanted NMs are tilted is found to alternate from one side to the other if comparing adjacent $\langle 1\,1\,0\rangle$ directions, as it is for $[\bar{1}\,1\,0]$ and $[0\,1\,\bar{1}]$. These symmetry properties are shown in detail in Fig. 2.19(f), where the fin morphology and orientation are sketched for all the main twelve slit directions.

The very same PF model used to study the growth of vertical NMs along the $\langle 1\,1\,2\rangle$ directions can be straightforwardly applied to simulate the growth on an arbitrarily oriented slit. To this purpose, it is sufficient to rotate the initial profile in the simulation domain, which is the reference frame for the crystallographic properties of the system. The result of the growth simulations on the circular pattern is described in Fig. 2.20. To have the more accurate representation by simulations of the fin morphologies, we have included $\{1\,1\,3\}$ facets in the model. These can be recognized in experiments mainly on the top of

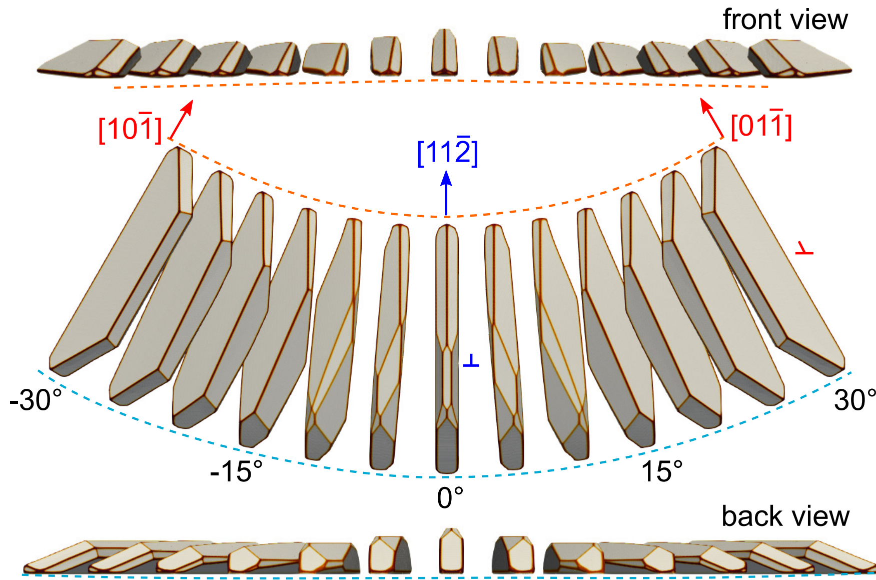

Figure 2.20: Fin profiles predicted by growth simulations for different orientations of a 1.5 μm slit. The rotation angles for the slit range from 0° to 30°, with 5° step. Vertical and slanted NMs are found at 0° and 30° respectively, while multi-faceted fins are obtained for intermediate orientations. As evident in the front and back views, the fin height is maximum for the 0°-oriented NMs and decreases to a minimum at 15° and slightly increases again while moving toward 30°. {1 1 0}, {1 1 1}B and {1 1 3} facets are considered in the simulation. (from Ref. [142])

the vertical NMs, on the sides of the main (1 1 1)B surface. The {1 1 3} facets may also contribute to the formation of the growth front for the slanted ⟨1 1 0⟩ NMs, while they could provide a more complex faceting for the intermediate orientations, which are still to be properly characterized. The {1 1 3} planes are reported to have a similar surface energy density [146] as the other low-index facets here considered, therefore it is reasonable to account for them from an energetic point of view. In principle, also {114} facets could appear due to their low energy [148] while, on the contrary, {112} facets are unstable [146]. Here however, we focus only on the {1 1 3} assuming that they are representative of similar {1 1 n} facets, as it is not possible to distinguish and identify properly other facet families from experiments. By applying the principle of best fitting the morphology of experiments, the adatom incorporation time used in the simulations for the {1 1 3} facets is estimated to be two times longer than the value for {1 1 1}B ($\tau_{113} = 2\tau_{111B}$). Intuitively, this leads to an intermediate growth rate if compared to the fastest {1 1 1}B front and the slow {1 1 0} facets.

When the slit is rotated by 30°, a progressive transition of the simulated morphologies is found, in good agreement with the one observed experimentally in Fig. 2.19(b). The different shapes result by a different balance of the {1 1 0}, {1 1 1}B and {1 1 3} facets, in some cases resulting in a more vertical shape, in others in a more slanted or rounded one, according to the closest orientation among the twelve described in Fig. 2.19(f). When the oxide orientation differs just of a small angle from the [1 1 $\bar{2}$] or [0 1 $\bar{1}$] directions, the simulated morphology tends to rotate along the [1 1 1] axis, in order to align to the more

favorable axis. In particular, a strong asymmetry is evident when considering the largest misalignment of 15° in which the two sides of the fin tend to rotate toward opposite optimal slit orientations.

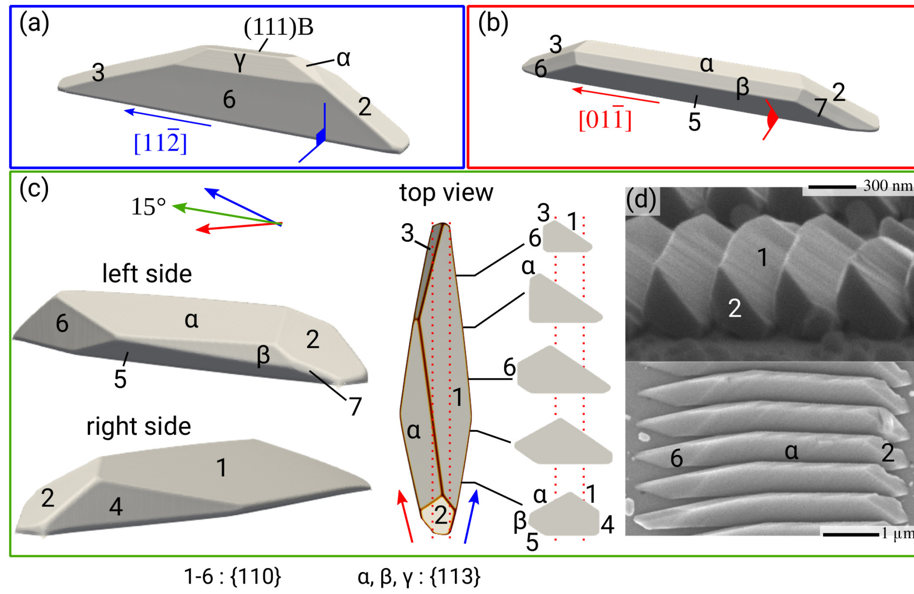

Figure 2.21: Details of the simulated fin morphologies reported in Fig. 2.20 for three slit orientations: (a) vertical NM at 0°; (b) slanted NM at 30°; (c) multi-faceted fin structure at 15°, with coexistence of facets from both the 0°-oriented NM shape (facets 4 and 6) and the 30° one (facets 1 and 5). Different vertical cross-sections of the 15° fin are also reported, aligned with respect to the oxide slit, traced by the dotted lines, and show a large lateral overgrowth reflecting the tendency to realign with the 0° and 30° NMs. (d) SEM images corresponding to the 15° orientation, resembling the simulation results in panel (c). Steps and irregularities are distinguishable on the fin surfaces. (from Ref. [142])

The main result of simulations, which adds information to the analysis of the morphologies already presented in Fig. 2.19, is the possibility to clearly identify the facets that compose each fin. This analysis is performed in Fig. 2.21 for the main morphologies obtained by the simulation on the circular pattern. Panel (a) shows the vertical NM grown along the $[1\,1\,\bar{2}]$ orientation. The profile is clearly correspondent to the one analyzed in Fig. 2.17, with the additional modeling of $\{1\,1\,3\}$ facets. These mainly appear side-by-side to the elongated $(1\,1\,1)$B facet, and this result improves further the agreement with experiments. In panel (b) the slanted NM obtained with a $[0\,1\,\bar{1}]$ oxide slit is shown. As already recognized in the experiments of Fig. 2.19(d), the growth makes more favorable to develop an inclined shape in order to fit the main $\{1\,1\,0\}$ that bound the shape into the oxide slit. Here we can recognize that the top growth front is made of $\{1\,1\,3\}$ facets, in place of the $\{1\,1\,1\}$B. This is caused by the relative ratio between the incorporation times, which makes the $\{1\,1\,1\}$B disappearing faster, leaving only the two $\{1\,1\,3\}$ facets at longer evolution stages. As a consequence of that, the slanted NM is also a bit more thick than the vertical one, as the competing incorporation between $\{1\,1\,0\}$ and $\{1\,1\,3\}$ is less effective than with $(1\,1\,1)$B, therefore the transfer of material from the sides of the NM to the top growth front is less pronounced.

The most complex case is the growth of the crystal out of an oxide window which is misaligned by 15° with respect to a $\langle 1\,1\,\bar{2}\rangle$, or equivalently $\langle 1\,1\,0\rangle$. In this case, as it is reported in Fig. 2.21(c), the growth tendency is to align the facets both toward the $\langle 1\,1\,\bar{2}\rangle$ and $\langle 1\,1\,0\rangle$ morphologies, which are shown in the other two panels of the figure. Thus, the resulting shape contains $\{1\,1\,0\}$ facets present both in the vertical NM, such as those labeled as 4 and 6, and in the slanted one, as for the 1 and 5 labeled facets. As a consequence, as it is shown in the cross sections in Fig. 2.21(c), the fin tends to growth significantly on the horizontal direction, overgrowing on the oxide surface well beyond the oxide slit, which is indicated by the dotted lines. This morphology is in good agreement with the experimental data. In particular here a magnified view of the corresponding sector of the circular pattern from 2.21(d) is presented. Both simulations and experiment exhibit an edge on top of the fin, instead of the flat $(1\,1\,1)$B, possibly due to the connection of a slanted $\{1\,1\,0\}$, as for label 1, and a $\{1\,1\,3\}$ facet, labeled as α. In the experiments, some irregularities are found at the crystal top, probably resulting from growth defects, as it is particularly evident for the slanted NMs. Moreover, the grey-scale contrast of the SEM images identifies a striping along the elongated facets. This could suggest a high density of steps, which facilitate the rotation of the crystal geometry toward the actual $\{1\,1\,0\}$ and $\{1\,1\,3\}$ planes. Those atomic scale features cannot be explicitly included in our model, which is based on a continuum description targeted to capture a mesoscopic scale. However, their effect is played in the simulations by a small curvature of the facets. For the case of the largest $\{1\,1\,0\}$ in Fig. 2.21(c), an overall rotation of about 3° for the surface normal is found by comparing the two opposite sides of the facet. This results from the constraint which is imposed by the oxide window. In the initial growth stages, the deposited material is forced to accommodate accordingly to the slit in an unfavorable direction. Therefore, as soon as the morphology overcomes the oxide edge, it starts to overgrow on the oxide surface, balancing the increasing energy cost for the crystal-oxide interface with the capability of exposing well defined crystal facets.

2.4 Conclusions

In this chapter, we have deeply analyzed the role of orientation-dependent incorporation kinetics in driving the faceting of a crystal by means of growth simulations. In particular, it has been shown that the differences in the incorporation times for the different facets can influence the evolution of the crystal morphology. The competition between kinetics and other anisotropic properties, such as for the surface energy and for the material supply, has been studied. This has clarified that an intermediate growth regime has to be considered between the ECS and the KCS formulations, making the approach here proposed reliable to model realistic growth cases.

Indeed, the PF model here developed has efficiently captured the main features of the growth of GaAs homoepitaxial NMs by SAE-MBE. The kinetic origin of such a growth has been demonstrated, with particular attention to the impact of the slit orientation on the morphological changes observed for the nanomembranes. The main result of this analysis is

the possibility to extract fundamental information on the kinetic growth velocities of the GaAs facets. These, or more appropriately the incorporation times, are responsible of the morphological evolution of the growing nanostructures. In particular, the determination of these kinetic parameters was enabled by the analysis of the experiments performed on the peculiar patterns where the oxide slits were aligned on a circular array, to map all the possible crystal orientations having a more general picture of the system. The morphologies observed in experiments were then interpreted thanks to the PF simulations, allowing both for a precise characterization of the fin faceting and for a quantification of the growth parameters for GaAs. Despite the unavoidable approximations inherent in the continuum approach for the description of the crystal, without any possibility of modeling the fine atomic-scale detail such as steps and step bunching, the approach here proposed has proved to be reliable in analyzing the physics of the growth process. Importantly, this is not yet accessible by atomistic methods due to the length scale of the growing structures. Importantly, the properties deduced by simulations for the set of $\{1\,1\,1\}$B, $\{1\,1\,0\}$ and $\{1\,1\,3\}$ facets are well consistent with the morphologies observed experimentally for the different slit orientations. In particular, the incorporation times here estimated have revealed an interesting hierarchy in the facet growth rates: $\{1\,1\,1\}$B$>\{1\,1\,3\}\gg\{1\,1\,0\}$. The important point is that these properties cannot be inferred by looking at the corresponding surface energies, demonstrating in particular that the apparently reasonable concept for which high surface energy corresponds to high growth rate lacks of a quantitative confirmation. Indeed, it does not consider at all the complex dynamics of adatom redistribution and incorporation on the surface, which results to be crucial to explain the large difference in growth velocities which is observed in the present experiments. A difference in incorporation times which does not correlate with any difference in the surface energy densities.

Chapter 3

Elasticity in core/shell nanowires by finite element method

3.1 Continuum elasticity for semiconductor heteroepitaxy

In semiconductor heteroepitaxy, the lattice structure can exhibit a strain deformation. This phenomenon is common when the two materials involved in the growth have different lattice parameters, as it is for the GaP/InGaP and Ge/GeSn cases studied in the following Chapters 4 and 5. In general, the growing film has to adapt to match the lattice parameter of the substrate, requiring an elastic deformation of the crystal structure. The same result can be achieved thanks to a plastic relaxation mediated by defects [149–151], that however we are not going to include in our models.

The elastic deformation of the crystal can be described by the vector field of the displacement $\boldsymbol{u}$ [152]. If we consider a point of the system in its initial state, $\boldsymbol{r}_0$, and the new position $\boldsymbol{r}$ of the same point moved by the elastic forces, the displacement $\boldsymbol{u}$ is defined as the difference between these two positions:

$$\boldsymbol{u} = \boldsymbol{r} - \boldsymbol{r}_0 \tag{3.1}$$

In the limit of infinitesimal displacements, all the deformations of the solid can be described by linear elasticity [152]. In particular the elastic state of the system can be modeled by using a symmetric strain tensor, which includes all the first spatial derivatives of the displacement field:

$$\varepsilon_{ij} = \frac{1}{2}\left(\frac{\partial u_i}{\partial x_j} + \frac{\partial u_j}{\partial x_i}\right) \tag{3.2}$$

The indexes i, j correspond to the cartesian directions x, y, z. This notation describes the relative deformation of the solid, referred to the initial condition. The main advantage of the strain description is that it allows to deal with scalar quantities, rather than with a vectorial field. To have a complete picture of the system, we need to define also the forces that act into the system, so that we can describe the equilibrium state, as it will be discussed later. In particular, the elastic forces, caused by the reaction of the material

to the deformation, can be expressed by the stress tensor $\boldsymbol{\sigma}$, that has the dimension of a force per unit area. In the linear approximation provided by the Hooke's law, σ_{ij} is directly proportional to the strain:

$$\sigma_{ij} = \sum_{lm} C_{ijlm}\, \varepsilon_{lm} \tag{3.3}$$

where $\boldsymbol{C}$ is the symmetric tensor of the elastic constants.

If the growing film has to be compressed in order to match the lattice parameter of the substrate, it tends to expand in order to restore its zero-stress condition. This expansion, or more in general the strain that the system would assume to reach the zero-stress condition, is defined as the eigenstrain tensor $\boldsymbol{\varepsilon}^*$ [153]. The stress tensor $\boldsymbol{\sigma}$ can now be defined in a more complete form for our needs as depending on two strain quantities, the eigenstrain and the response strain $\boldsymbol{\varepsilon}$, as:

$$\sigma_{ij} = \sum_{lm} C_{ijlm}(\varepsilon_{lm} - \varepsilon^*_{lm}) \tag{3.4}$$

where for $\boldsymbol{\varepsilon} = \boldsymbol{\varepsilon}^*$ the stress is null, according to the definition of the eigenstrain. In a cubic structure, as it is for Ge, Si and GeSn the eigenstrain is diagonal and can be defined as:

$$\boldsymbol{\varepsilon}^* = \begin{bmatrix} \varepsilon^* & 0 & 0 \\ 0 & \varepsilon^* & 0 \\ 0 & 0 & \varepsilon^* \end{bmatrix} \tag{3.5}$$

where $\varepsilon^* = \frac{a_{film} - a_{substrate}}{a_{film}}$. For core/shell nanowires the a_{film} corresponds to the material of the growing shell, while $a_{substrate}$ refers to the core, which acts as a substrate for the growth of the shell layers and is the initial reference for the elastic deformation. In the case of an hexagonal lattice, we have to distinguish between the a and c lattice parameters. Therefore the eigenstrain can be written as:

$$\boldsymbol{\varepsilon}^*_{hex} = \begin{bmatrix} \varepsilon^*_a & 0 & 0 \\ 0 & \varepsilon^*_a & 0 \\ 0 & 0 & \varepsilon^*_c \end{bmatrix} \tag{3.6}$$

The tensor $\boldsymbol{C}$, whether the crystal has a cubic symmetry as for Ge/Si systems, can be expressed using three constants [154]: C_{11}, C_{12} and C_{44}, which correspond to the stress and strain components as outlined in table 3.7.

$$\boldsymbol{C} = \begin{bmatrix} C_{11} & C_{12} & C_{12} & 0 & 0 & 0 \\ C_{12} & C_{11} & C_{12} & 0 & 0 & 0 \\ C_{12} & C_{12} & C_{11} & 0 & 0 & 0 \\ 0 & 0 & 0 & C_{44} & 0 & 0 \\ 0 & 0 & 0 & 0 & C_{44} & 0 \\ 0 & 0 & 0 & 0 & 0 & C_{44} \end{bmatrix} \tag{3.7}$$

In the case of isotropic elastic properties, the elastic constants are further related by $C_{11} = C_{12} + 2C_{44}$, so that the Hooke's law depends on two parameters only, renamed as $\lambda = C_{12}$ and $\mu = C_{44}$, which are the Lamé coefficients. In this case, the relation between the stress tensor and the strain tensor can be written as:

$$\sigma_{ij} = \lambda \sum_k (\varepsilon_{kk} - \varepsilon^*_{kk}) + 2\mu \, (\varepsilon_{ij} - \varepsilon^*_{ij}) \tag{3.8}$$

A useful relation is the conversion between elastic constants, such as Young modulus E and Poisson ratio ν:

$$\begin{aligned} \mu &= \frac{E}{2(1+\nu)} & \lambda &= \frac{E \cdot \nu}{(1+\nu)\cdot(1-2\nu)} \\ E &= \mu\frac{3\lambda + 2\mu}{\lambda + \mu} & \nu &= \frac{\lambda}{2(\lambda+\mu)} \end{aligned} \tag{3.9}$$

E is the stress/strain ratio along the same axis, while λ is the ratio of the strain in one direction to the strain in the transverse direction.

On the contrary, when the crystal structure is hexagonal, as for the wurtzite materials GaP and InGaP presented in Chapter 4, the tensor $\boldsymbol{C}$ is expressed in terms of:

$$\boldsymbol{C} = \begin{bmatrix} C_{11} & C_{12} & C_{13} & 0 & 0 & 0 \\ C_{12} & C_{11} & C_{13} & 0 & 0 & 0 \\ C_{13} & C_{13} & C_{33} & 0 & 0 & 0 \\ 0 & 0 & 0 & C_{44} & 0 & 0 \\ 0 & 0 & 0 & 0 & C_{44} & 0 \\ 0 & 0 & 0 & 0 & 0 & C_{66} \end{bmatrix} \tag{3.10}$$

where $C_{66} = (C_{11} - C_{12})/2$. To determine the equivalent elastic constants for the hexagonal structure, whether only the cubic ones are present in the literature, it is possible to use the Martin's relations [155].

When dealing with elasticity simulations, it is important to properly set the reference frame in which the elastic properties are defined. In particular, when we consider the nanowire structure, the hexagonal matrix is already defined so that the [0 0 0 1] axis naturally coincides with the z direction [22]. On the contrary, when dealing with cubic crystals and nanowire along the [1 1 1] direction, a rotation of the elastic constants matrix is required to properly use these parameters in the simulations. In particular, we have to consider the rotation matrix R:

$$R = \begin{bmatrix} \frac{1}{\sqrt{2}} & 0 & -\frac{1}{\sqrt{2}} \\ -\frac{1}{\sqrt{6}} & \sqrt{\frac{2}{3}} & -\frac{1}{\sqrt{6}} \\ \frac{1}{\sqrt{3}} & \frac{1}{\sqrt{3}} & -\frac{1}{\sqrt{3}} \end{bmatrix} \tag{3.11}$$

to compute the elastic constants in the proper reference frame as $\tilde{C}_{ijkl} = R_{ip}R_{jq}R_{ks}R_{lt}C_{pqst}$. By applying this transformation, the $\tilde{\boldsymbol{C}}$ tensor becomes:

$$\tilde{\boldsymbol{C}} = \begin{bmatrix} \tilde{C}_{11} & \tilde{C}_{12} & \tilde{C}_{13} & \tilde{C}_{14} & 0 & 0 \\ \tilde{C}_{12} & \tilde{C}_{11} & \tilde{C}_{13} & -\tilde{C}_{14} & 0 & 0 \\ \tilde{C}_{13} & \tilde{C}_{13} & \tilde{C}_{33} & 0 & 0 & 0 \\ \tilde{C}_{14} & -\tilde{C}_{14} & 0 & \tilde{C}_{44} & 0 & 0 \\ 0 & 0 & 0 & 0 & \tilde{C}_{44} & \tilde{C}_{14} \\ 0 & 0 & 0 & 0 & \tilde{C}_{14} & \tilde{C}_{66} \end{bmatrix} \tag{3.12}$$

where the elements are defined as:

$$\begin{aligned} \tilde{C} &= (C_{11} + C_{12} + 2C_{44})/2 \\ \tilde{C} &= (C_{11} + 5C_{12} - 2C_{44})/6 \\ \tilde{C} &= (C_{11} + 2C_{12} - 2C_{44})/3 \\ \tilde{C} &= \sqrt{2}(-C_{11} + C_{12} + 2C_{44})/6 \\ \tilde{C} &= (C_{11} + 2C_{12} + 4C_{44})/3 \\ \tilde{C} &= (C_{11} - C_{12} + C_{44})/3 \\ \tilde{C} &= (C_{11} - C_{12} + 4C_{44})/6 \end{aligned}$$

An interesting property of the continuum description of the elastic properties is that, for the hexagonal crystal structure, the C tensor is invariant for any rotation along the NW axis [0 0 0 1], although the fundamental atomic lattice is not. However, the same property does not hold for cubic NW along [0 0 1]. In this case the system is invariant only for rotations along the axis of an angle which is multiple of $\pi/3$ or it becomes invariant under isotropic conditions, when it holds that $\tilde{C}_{44} = (\tilde{C}_{11} - \tilde{C}_{12})/2$. In the comparison with the experimental measures by TEM of the strain in NWs, it can be useful to extract from the strain tensor a specific component referred to a prescribed crystal direction, which is different from the axis of the reference frame used in the simulations. This result can be achieved by rotating the strain tensor along the prescribed reference frame by the following transformation:

$$\tilde{\boldsymbol{\varepsilon}} = R \cdot \boldsymbol{\varepsilon} \cdot R^T \tag{3.13}$$

where R is the rotation matrix, with the proper angular coefficients, and R^T is its transposed. Additionally, when dealing with NWs, it is useful to express the strain in cylindrical coordinates, namely radial, tangential and axial, which can be obtained from the cartesian tensor as:

$$
\begin{aligned}
\varepsilon_R =& \varepsilon_{xx}\cos(\mathrm{atan}(y/x))\cos(\mathrm{atan}(y/x)) + 2\varepsilon_{xy}\sin(\mathrm{atan}(y/x))\cos(\mathrm{atan}(y/x)) \\
&+ \varepsilon_{yy}\sin(\mathrm{atan}(y/x))\sin(\mathrm{atan}(y/x)) \\
\varepsilon_T =& \varepsilon_{xx}\sin(atan(y/x))\sin(\mathrm{atan}(y/x)) - 2\varepsilon_{xy}\sin(\mathrm{atan}(y/x))\cos(\mathrm{atan}(y/x)) \\
&+ \varepsilon_{yy}\cos(\mathrm{atan}(y/x))\cos(\mathrm{atan}(y/x)) \\
\varepsilon_A =& \varepsilon_{zz}
\end{aligned}
$$

3.1.1 Mechanical equilibrium

The deformation of the lattice structure in the nanowire is a process that can be considered instantaneous with respect to the typical time scale of deposition and growth. Therefore, when dealing with elasticity in semiconductors, the interest is not for the dynamics of the elastic relaxation, but for its stationary condition, which represents the actual state of the NW once it is grown. The mechanical equilibrium, which corresponds to the hypothesis required to calculate the strain, is defined as the condition where the sum of the elastic forces is zero:

$$
\boldsymbol{F}_{tot} = \int_{\Omega} \boldsymbol{f}\ d^3r + \int_{\partial\Omega} \boldsymbol{\sigma}\cdot\hat{n}\ d^2r = 0 \tag{3.14}
$$

where $\boldsymbol{f}$ are the forces per volume unit, $\boldsymbol{\sigma}$ is the elastic force per area unit, Ω is the whole domain considered and $\partial\Omega$ is the free surface. Thanks to the divergence theorem, the equilibrium condition can be written as:

$$
\int_{\Omega} \left(\boldsymbol{f} + \nabla\cdot\boldsymbol{\sigma}\right)\ d^3r = 0 \tag{3.15}
$$

In the growth of a crystal, it can be assumed that no volume forces are present, so $\boldsymbol{f} = 0$. By considering equation 3.15 valid pointwise, the mechanical equilibrium condition can be rewritten in the following system:

$$
\begin{cases}
\nabla\cdot\boldsymbol{\sigma} = 0 & \text{on} \quad \Omega \\
\boldsymbol{\sigma}\cdot\hat{n} = 0 & \text{on} \quad \Gamma_N \\
\boldsymbol{u} = 0 & \text{on} \quad \Gamma_D
\end{cases} \tag{3.16}
$$

Dirichlet conditions are set on the bottom boundary Γ_D of the nanowire, where it is assumed that all the displacements are null during the evolution process as there the crystal is fixed to the substrate. On the contrary the Neumann boundary Γ_N represents the interface between vacuum, or equivalently the surrounding vapor phase, and the crystal, where the projection of the stress perpendicular to the surface must be equal to 0, since the system is fully relaxed towards it.

The system in equation 3.16 can be formulated in terms of the displacement field $\boldsymbol{u}$. In the case of a semi-infinite isotropic film, with a biaxial stress and uniform composition, the elastic properties μ and λ don't change in the film. The eigenstain can be expressed by a constant tensor $\varepsilon^*_{ij} = \varepsilon^*\delta_{ij}$. In this approximation, using the conversion between the stress

tensor and the displacement field from equations 3.8 and 3.2, the mechanical equilibrium condition $\nabla \cdot \boldsymbol{\sigma} = 0$ can be expressed by the Navier-Cauchy equation:

$$\mu \nabla^2 \boldsymbol{u} + (\lambda + \mu)\, \nabla (\nabla \cdot \boldsymbol{u}) = 0 \tag{3.17}$$

3.2 Finite element method

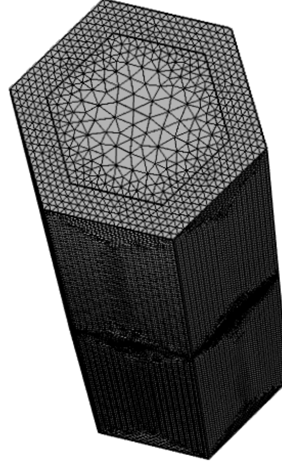

Figure 3.1: Schematics of the explicit mesh for a core/shell nanowire structure.

The Finite Element Method (FEM) is a common and efficient procedure to solve Partial Differential Equations (PDE). Generally speaking, a PDE problem is composed by an equation, that includes differential operators, and a suitable number of boundary conditions, that are necessary to find a unique solution of the problem. The order of the equation is determined by the highest grade of derivation. Usually the PDE problems can be reduced to a second order one, separating the main equation in a set of equations with an order minor or equal to $\mathrm{II}^{\mathrm{nd}}$, which can be handled by the FEM solver. The following system shows a prototypical PDE problem, including differential operators up to second order and proper boundary conditions:

$$\begin{cases} -\nabla \cdot (a \nabla u) + b \nabla u + cu = d & \text{on} \quad \Omega \\ u = g & \text{on} \quad \Gamma_D \\ a \nabla u \cdot \hat{n} = e & \text{on} \quad \Gamma_N \end{cases} \tag{3.18}$$

It represents all the possible combinations of I^{st} and $\mathrm{II}^{\mathrm{nd}}$ order operators that will be used in the present work. The FEM relies on two main concepts: the weak formulation of the PDE and the Galerkin method.

3.2.1 Weak formulation

The first step to solve a PDE problem consists in expressing the equations in the weak formulation. It is basically an alternative way to write the problem, which introduces some more general properties that can simplify the numerical procedure. The weak form

is defined as the scalar product between the PDE and a test function $\psi \in X$, where $X := \{\psi \in H^1(\Omega) : \psi = 0 \text{ on } \partial\Omega\}$. In other terms it consists in the integration, over the whole domain Ω, of the product between the PDE and a function ϕ.

$$(\text{PDE},\ \psi) = \int_\Omega \text{PDE} \cdot \psi \tag{3.19}$$

For example, the weak formulation of the PDE, from equation 3.18, results:

$$-\int_\Omega \nabla \cdot (a\nabla u)\ \psi + \int_\Omega b\nabla u\ \psi + \int_\Omega cu\ \psi = \int_\Omega d\ \psi \tag{3.20}$$

This new integral equation can be re-arranged, in order to simplify the procedure for finding a solution. The aim is to reduce the derivation order over the solution u by integrating per part. More precisely one derivative can be moved to the test function ψ, using the identity $\nabla(f\nabla A \cdot B) = \nabla \cdot (f\nabla A)\, B + f\nabla A \cdot \nabla B$:

$$\begin{aligned} -\int_\Omega \nabla \cdot (a\nabla u)\ \psi = \int_\Omega a\nabla u \cdot \nabla\psi - \int_\Omega \nabla \cdot (a\nabla u\ \psi) = \\ \int_\Omega a\nabla u \cdot \nabla\psi - \int_{\partial\Omega} a\nabla u \cdot \hat{n}\ \psi \end{aligned} \tag{3.21}$$

Apparently this seems just an alternative way to write the problem, but it contains a deeper and extremely useful property: we have to require only that the first derivative of u is integrable over Ω, while in the original PDE problem it was necessary to guarantee that u is twice derivable.

By applying this technique a surface integral is found, whose value depends on the boundary conditions. In the following derivation, it is assumed that $e \equiv 0$, so the boundary integral is 0 and can be neglected. Under this condition, a second order PDE gives these possible weak formulations, for each order of derivation:

$$\begin{array}{ll} 2^{nd} & (-\nabla \cdot (a\nabla u)\,, \psi) = (a\nabla u, \nabla\psi) \equiv A(u,\psi) \\ 1^{st} & (b\nabla u, \psi) = -\,(u, \nabla \cdot (b\psi)) \equiv B(u,\psi) \quad \text{and} \quad (\nabla \cdot (bu)\,, \psi) = -\,(u, b\nabla\psi) \\ 0^{th} & (u,\psi) \end{array} \tag{3.22}$$

3.2.2 Galerkin method

The weak formulation allows to simplify the differential problem, but it still requires something more to find the solution u. Since most of the second order PDE can't be solved analytically, there is the need of a numerical strategy, like the Galerkin method, to find an approximate solution. The space Ω is partitioned in many subspaces, labeled with h. The geometry of these subspaces is defined by a set of points in Ω, called nodes, and by the connection between these points. The idea is to find an approximate solution on each smaller space h and then, based on these results, to establish the solution for the entire space, interpolating the single h-solutions. The key point is that the space has to be split in portions on which it is possible to solve the problem, otherwise this subdivision of Ω is

useless. For each h-space it is necessary to find a set of basis functions $\{\psi_1 \dots \psi_n\}$. Each function is associated to a node, with the particular property $\psi_j(x_i) = \delta_{i,j}$. In this way it is possible to write the approximate solution for the h-space as a linear combination of ψ_j:

$$\begin{aligned} u_h(x) &= \sum_{j=1}^{n} u_j \ \psi_j(x) \\ u_h(x_i) &= \sum_{j=1}^{n} u_j \ \psi_j(x_i) = u_i \quad \text{since} \quad \psi_j(x_i) = \delta_{i,j} \end{aligned} \tag{3.23}$$

But also the weak formulation of the PDE can be written on this basis, using A and B to indicate the different orders of differentiation:

$$\begin{cases} A(u, \psi_i) + B(u, \psi_i) + (u, \psi_i) = (d, \psi_i) & \forall i \in I_\Omega \\ u = g & \text{on } I_{\Gamma_D} \end{cases} \tag{3.24}$$

$$\begin{cases} \displaystyle\sum_{j=1}^{N} \left(A(\psi_j, \psi_i) + B(\psi_j, \psi_i) + (\psi_j, \psi_i) \right) u_j = (d, \psi_i) & \forall i \in I_\Omega \\ u_i = g_i & \forall i \in I_{\Gamma_D} \end{cases} \tag{3.25}$$

The general problem for u has been reduced to a problem for the coordinates u_j and can be written in matrix form:

$$\mathrm{M} \ \boldsymbol{u} = \boldsymbol{d} \tag{3.26}$$

where the matrix M is composed by the following elements:

$$\mathrm{M}_{i,j} := \begin{cases} A(\psi_j, \psi_i) + B(\psi_j, \psi_i) + (\psi_j, \psi_i) & \forall i \in I_\Omega \\ 1 & \forall i \in I_{\Gamma_D}, \quad i = j \\ 0 & \forall i \in I_{\Gamma_D}, \quad i \neq j \end{cases} \tag{3.27}$$

and

$$d_i := \begin{cases} (d, \psi_i) & \forall i \in I_\Omega \\ g_i & \forall i \in I_{\Gamma_D} \end{cases} \tag{3.28}$$

By solving this linear system it is possible to build the set of local solutions u_i at each node. By interpolating these values on the whole space Ω it is then possible to obtain the approximate solution of the original PDE.

Chapter 4

Bending in core/shell GaP/InGaP wurtzite nanowires

Core/shell nanowires are a promising platform for the development of high-quality heterostructures made of semiconductors with a large lattice mismatch. Another advantage that they can provide if compared to the growth on flat substrates is the possibility of transferring the lattice structure from the core to the shell. In particular, in this Chapter we present the system of wurtzite GaP/$In_xGa_{1-x}P$ core/shell nanowires, studied with the aim of developing an LED solution for the green light emission. Experiments revealed that these nanowires exhibit a random bending phenomenon, which has to be avoided for the applications. Here we provide an analysis of the system, by combining transmission electron microscopy and energy dispersive X-ray spectroscopy with finite element method static simulations to get a better understanding of the nanowire bending for this type of core/shell nanowires. Our final goal is to propose a solution to prevent, or at least to minimize, the tendency to bend the core/shell structure.

4.1 Introduction

Semiconductor heteroepitaxy is a technique commonly exploited to develop technologies for micro- and opto-electronics in order to improve the performances of devices. However, the difference of the lattice parameters between the most common semiconductors limits the range of usable combinations [156]. Indeed the lattice mismatch often promotes the nucleation of detrimental defects, such as misfit dislocations [97], that reduce the device performance. In this context, core/shell nanowires are a system of great interest as they can be considered as a type of heteroepitaxy on a compliant substrate, especially in the case of cores with a small diameter [157], and that enables the elastic relaxation of the strain in the shell in two directions, something which is not possible in planar heterostructures [158]. These advantages have been predicted to lead to much lower residual strain and therefore to a higher critical thickness for defect nucleation [83, 159]. Therefore, core-shell nanowires do represent a great promise in fabricating novel nanostructures beyond the current technological limits, for example in the fields of solid state lighting [83, 160, 161],

electronics [162], photovoltaics [163–165] and hydrogen production [166]. Very recently, nanowires have been also proposed as applications in quantum computing and Majorana physics [167] when combining a semiconductor core with a superconductive shell.

Despite these promising premises, the lattice mismatch can still lead to unwanted phenomena even in core/shell nanowires, as it is for the case of surface roughness [168] and surface quantum dots [169], the formation of compositional inhomogeneities in ternary compounds, which could affect several properties, for instance the thermal transport [170, 171]. Moreover, even if the plastic relaxation can be prevented in nanowires, a residual strain is still present and this could lead to morphological changes of the nanostructures. The case that we are going to analyze here is the bending of nanowires, which generally hinders their applications in array-based devices. Only very recently the bending behavior has been proposed as a controllable property [132], opening new possibilities for the design of novel nanowire-based devices. In the literature [172], the bending has been already related to one asymmetry in the shell thickness by TEM measures, which are in most cases a time-consuming techniques and that requires the manipulation of the nanowires out of the growth array. In that analysys, it has been proposed as very useful the possibility to develop 3D simulations which can couple with the asymmetry in the shell in order to gain additional information about the bending behavior. Actually, a study based on finite element calculations of shell thickness and composition asymmetry for InAsP has been previously considered [173]. Still, despite a dedicated X-ray diffraction analysis, no detailed comparison between the numerical results and the experimental measurements has been performed there, particularly because no experimental access to composition asymmetry was possible.

Therefore, in the present NW system, a diagnostic tool for quickly estimating the degree of both asymmetries in nanowires by measuring the bending, for instance based on scanning electron microscopy, would allow to save time and resources in the optimization of the growth of these nanostructures. In this Chapter, we study the bending as induced by elastic strain relaxation in lattice-mismatched wurtzite GaP/$In_xGa_{1-x}P$ core-shell nanowires [83, 174]. We rely on dedicated SEM and TEM measurements, performing EDX analysis for the composition, combined with a theoretical analysis based on realistic three-dimensional Finite Element Method simulations, which allow to quantitatively relate the bending to the geometric and to compositional asymmetry. In particular, in Section 4.3.1 we investigate a representative core-shell NW, accurately mapping its strain condition and comparing the bending to the experimental data, discussed in Section 4.2. Then, in Section 4.3.3 we extend the FEM model to a set of WZ GaP/$In_xGa_{1-x}P$ samples with varying shell composition and thickness, with the aim to indicate a predictive procedure to infer the degree of asymmetry of a core-shell NW, by simply measuring its bending curvature. All the growth experiments and the measurements have been performed by the group of Prof. Bakkers at Technische Universiteit Eindhoven. In particular the growth was performed by Luca Gagliano, while the TEM studies by Marcel A. Verheijen.

4.2 Experimental

4.2.1 Materials and methods

The template used for the shell growth is made by GaP wurtzite nanowires, grown on a GaP(111)B substrate by using VLS technique. The growth is catalyzed by a Au droplet, positioned on the substrate by nanoimprint lithography, with a 2.5 μm pitch. The deposition is made by Metalorganic Vapour Phase Epitaxy (MOVPE) at 615° C using Trimethylgallium (TMGa) and Phosphine (PH_3) as precursors. To prevent sidewall tapering, HCl is added in the chamber. The second step of the growth process consist in the removal of the Au catalyst by a Iodine solution. Then the shell is grown by MOVPE using TMGa, Trimethylindium (TMIn) and PH_3 as precursors. The key point of this growth technique is the capability of transferring the WZ crystal structure from the core to the shell [20, 83].

4.2.2 SEM, TEM and EDX characterization

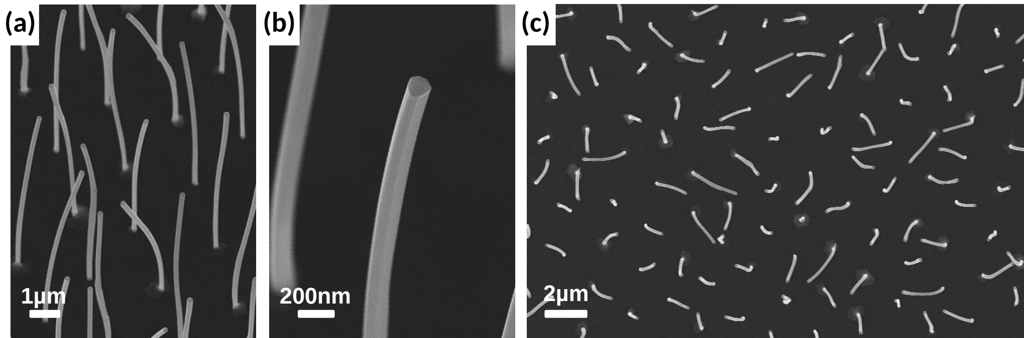

Figure 4.1: SEM images of WZ GaP/InGaP core–shell NWs grown on a zinc-blende (1 1 1) GaP substrate. (a) An SEM image taken at 30° tilt, showing the clear bending of the nanowires. The nanowires exhibit different degrees of bending: in some cases being bent in two different directions, forming an S-shape. This suggests asymmetry in the core–shell structure developing not only radially, but also axially along the nanowire length. (b) A close-up of a bent WZ GaP/InGaP core–shell NW. (c) A top view SEM image, showing the different bending directions of the nanowires. The degree of bending and the orientation are at random. (from Ref. [175])

The first result that can be observed after the NW growth is a clear bending phenomenon. In Fig 4.1(a,b) we show SEM images of the nanowires after the shell growth. The bending appears to be at random, with different magnitude for the different nanowires. Some of them seem even bent in two directions, resulting in an S-shape. The randomness is confirmed by the top view in panel (c), excluding a systematic effect of the deposition or of a crystallographic preferred orientation. Here we investigate this phenomenon by considering that a core/shell NW can be a stressed system due to the lattice mismatch between the core and the shell materials. The residual strain can make the ideal NW structure a metastable system, which eventually bends to reduce the elastic energy density. However, SEM images are not sufficient to have a precise characterization of the bending. Therefore we applied TEM to the study of the morphology of several WZ GaP/$In_xGa_{1-x}P$ NWs, as shown in Fig. 4.2.

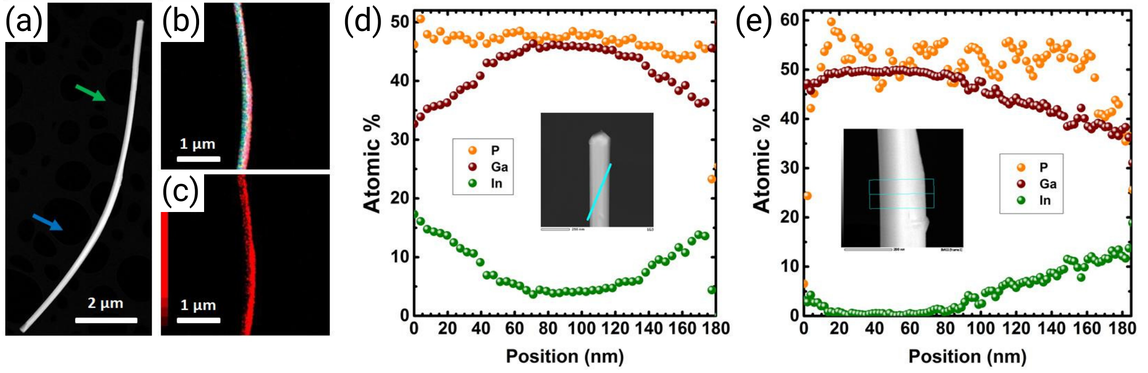

Figure 4.2: (a) A HAADF image of a WZ GaP/$In_{0.2}Ga_{0.8}P$ (average composition) core–shell NW. We see that the lower part is sizeably thicker than the upper central part, but for the very top segment, which is only slightly thinner than the bottom segment. (b), (c) An EDX colour map of the same nanowire, demonstrating the difference in thickness and composition between the two sections of the nanowire. In (b) we show the signals of both Ga (green) and In (red), while in (c) we show only the In signal to better clarify the link between the In content and local curvature. (d), (e) EDX linescans of the WZ GaP/$In_{0.2}Ga_{0.8}P$ core–shell NW in (a)–(c). The light blue lines in the insets indicate where the measurements were taken and the position is finally projected perpendicularly to the NW axis. (d) is across the region close to the tip of the NW (total diameter ∼175 nm), where the nanowire is approximately symmetric, both in thickness and composition. (e) is across the bottom section (total diameter ∼185 nm), and shows a relevant asymmetry, both in shell thickness and composition. The results of these linescans are summarised in Table 4.1. (from Ref. [175])

In Fig. 4.2 we show the high-angle annular dark-field scanning transmission electron microscopy (HAADF) image of a representative core/shell nanowire. To perform this analysis, the nanowires are removed from the growth substrate an placed on a TEM grid, in the following we will define this condition as ‘free-standing’ because the nanowire is able to deform freely at both tips. From panel (a) we can recognize a general bending of the structure. However, by the closer analysis shown in panels (b,c), we recognize that the structure is not uniform along the nanowire axis. Indeed a thinner and more straight section is recognized in the top part, highlighted by the green arrow, while a thicker an more bent section is found in the bottom region, highlighted by the blue arrow. By considering that the GaP cores were untapered, at least on the length scale here considered, we can deduce that the thickness changes is due to a change in the shell thickness.

	Thickness left side (nm)	In fraction left side	Thickness right side (nm)	In fraction right side
Top section (exp.)	40 ± 0.5	0.30 ± 0.04	35 ± 5	0.28 ± 0.04
Bottom section (exp.)	10 ± 0.5	0.10 ± 0.04	80 ± 5	0.22 ± 0.04
Top section (sim.)	40	0.20	35	0.25
Bottom section (sim.)	10	0.10	80	0.30

Table 4.1: Structural parameters of the WZ GaP/$In_{0.2}Ga_{0.8}P$ core–shell NW shown in Fig. 4.2, obtained by TEM analysis. We report the thickness and the composition of the $In_xGa_{1-x}P$ shell on either side of the NW. The resulting asymmetries cause the bending.

In order to confirm this hypothesis, we investigate more in detail the NW structure by performing energy-dispersive X-ray diffraction (EDX) linescans, as shown in Fig. 4.2(d-e), perpendicularly to the NW axis. The inset of each panel shows where the scan was performed along the NW. The numerical data for the composition are also reported in table 4.1. The lower In concentration, and consequently the higher Ga content, has to be attributed to an artifact of the measurement technique. Indeed, the beam has to penetrate and probe the entire nanowire, which makes the core to contribute to the measurement. This causes an underestimation of the In content in the middle of the scan, where the volume of the core contributes more. Therefore, the linescan is more accurate when probing only, or mostly, the shell volume, which corresponds to the left and right side of the plot, which is actually the region of interest in order to explain the observed bending as due to irregularities in the shell. From these data, we have an additional confirmation that the change in the nanowire diameter is due to the shell, and not just to a tapering of the core. In the upper section (panel (d)) we observe a rather symmetric shell, with a slight increase of the diameter in the region close to the tip. On the opposite, in the bottom section (panel (e)) a strong asymmetry is found in the shell thickness. The convex (right) side is about 80nm thick, while the concave (left) side has a shell 10 nm thin. From the EDX maps, we can investigate also the role played by the shell composition. By looking, for instance, at the In concentration, we find a similar trend as for the shell thickness. The top part has a symmetric composition, within the experimental uncertainty, while the bottom one is asymmetric. Moreover, we recognize a gradient of In content across the shell region, possibly due to an increased incorporation for larger thicknesses, similarly to what is observed for Ge/GeSn core/shell nanowires.

Based on these experimental results, we can try to qualitatively explain the bending of the nanowires, in order to proceed with the development of a numerical model to get also quantitative results. The model is based on the occurrence of a random event, that could be the formation of a defect, that causes an initial asymmetry of the wire. This generates an asymmetric balance between the two sides of the shell, that induces a bending of the structure. As a result, the elastic relaxation of the lattice mismatch is modified, and becomes more effective in the concave side of the nanowire, where the expansion of the lattice parameter is favored. This, in turn, promotes both a preferential material diffusion, and in particular In segregation, towards the concave side, characterized by a lower elastic energy. This enhances the asymmetry of the system, promoting the bending of the nanowire. The random event than initially triggers the process can be associated with the formation of an island on the surface of the WZ GaP core or by some defect caused by the Au catalyst removal process, eventually including some residual Au nanoparticles. The nanowires where the bending is more complex, with a change in the bending direction along the axis, can be modeled by considering the occurrence of multiple initial random events on opposite sides of the nanowire.

4.3 Elastic continuum predictions

The bending of a nanowire, in a first approximation, has many similarities with the case of cantilever bending. Indeed, a nanowire can be simplified as a beam with one end being fixed boundary, which corresponds to the base attached to the substrate, and the other end which is free to move. When a force is applied to the cantilever, for instance to the free tip, the structure reacts by bending, similarly to a spring which is compressed by an external force. Analytically, the problem of beam bending, here limited to static conditions with no discussion of the vibrational mode, can be described by two main theories: the Euler-Bernoulli and the Timoshenko ones [176]. Following the latter formulation, the deformation of a beam along the z axis, when a force is applied along the x axis, can be described by the following displacements functions: $u_x(x, y, z) = w(z)$, $u_y(x, y, z) = 0$ and $u_z(x, y, z) = z\psi(x)$, where ψ is the rotation angle an xy cross-section of the beam. The beam deformation can then be determined by solving the following system of partial differential equations:

$$\begin{cases} \dfrac{d^2}{dx^2}\left(EI\dfrac{d\psi(x)}{dx}\right) = F(x) \\ \dfrac{dw}{dx} = \psi - \dfrac{1}{kAG}\dfrac{d}{dx}\left(EI\dfrac{\psi(x)}{dx}\right) \end{cases} \tag{4.1}$$

where L is the total length of the beam, A is the area of the xy cross-section, I is the area moment of inertia, k is the Timoshenko shear coefficient, E is the elastic modulus and G the shear one. The external force applied to the system is represented by the function F(x), that can be restricted to the tip of the cantilever, or to an intermediate point, by applying a Dirac-delta function. The Euler-Bernoulli formulation can be obtained when considering negligible the last term of the second equation. This basically holds when $L \gg 1$ and implies that the cross-section is always perpendicular to the central axis of the beam. When considering a force F applied to the top of the cantilever, the solution for the displacement function is $w(z) = \frac{F(L-z)}{kAG} - \frac{Fz}{2EI}\left(L^3 - \frac{z^2}{3}\right) + \frac{FL^3}{3EI}$, usually reported in the approximated form as being expressed only by the third term. This analytical model can be applied when the length of the beam is larger if compared to the maximum displacement at the tip. This is a result of the first order approximation in eq. (3.2). To go beyond this limit, a geometrically nonlinear model [177] has to be developed by accounting higher-order contributions in the definition of the strain energy density [178, 179]. Core/shell nanowires go well beyond the limits of the analytical models due to the non-uniform thickness and composition properties of the shell, which change along the NW axis. Moreover, the bending force is an internal one, as we will discuss, and it is strongly affected by the asymmetry of the NW. For these reasons, we exploit a FEM model which includes the anisotropic elastic constants for the materials involved, but for the sake of simplicity relies on the linear elasticity theory.

4.3.1 Modeling core/shell nanowire bending

In the hypothesis that the bending of the nanowire is correlated with a different elastic relaxation on the two sides of the nanowire, we need to develop a numerical model to assess quantitatively the strain relaxation mechanisms in the structure. In particular, we study the WZ GaP/$In_xGa_{1-x}P$ core-shell structure by FEM simulations using the COMSOL Multiphysics® software. The size of the nanowire and the length scale where the bending is observed require to apply a continuum mechanics description [22, 180, 181]. Elastic deformations in core/shell nanowires arise mainly from the lattice mismatch between the core and the shell. The bulk lattice parameter of the GaP/$In_xGa_{1-x}P$ alloy is computed according to the linear Vegard's law [182], by an interpolation between the bulk lattice parameters of InP [183] and GaP [184] in the wurtzite phase. The same procedure is used to determine the elastic constants of the shell, which are accounted in the model by considering the proper anisotropy for the wurtzite phase [185]. The model is developed in 3D, with an hexagonal base for both the core and the shell. In the following, we will define the length of the apothem as NW radius. The deformations are then determined numerically by the FEM by solving the mechanical equilibrium problem. It mainly consists in the minimization of the elastic energy, profiting of the capability of the crystal structure to expand toward the free surface. Both tips of the nanowire are modelled as free surfaces by considering the nanowire as free-standing, that corresponds to the condition used for TEM analysis where the NW is detached from the growth substrate. Numerically, this is achieved by applying just a zero displacement for the center of the nanowire and to avoid any pure rotation of the whole structure, which does not impact in any way with the solution of the mechanical equilibrium problem, but just with the reference frame.

We now have to model the asymmetries that have been observed in the nanowires to capture the bending behavior. In Fig. 4.3 we show a sketch of the core/shell NW to describe the main variables introduced in the bending model. In panel (a) the blue region represents the inner core, which is surrounded by the red shell. To achieve that type of bending, we can play on two different parameters. The first asymmetry that we consider is related to the shell thickness. As shown in panel (b), we model it by applying a shift of the hexagonal cross section with respect to the core one, so that we have that the left side of the shell is thicker than the right one. This means that the compressive load stored in the shell is different for the two sides, and this induces the bending on the right side of the structure, corresponding to the thinner shell. The second type of asymmetry that can be considered is related to the composition of the shell, that we will measure as the In concentration, which is responsible for the lattice mismatch in the system. As shown by the color map in panel (c), we set a linear gradient for the In composition which is higher on the left side (red) and lower on the right one (yellow). To quantify this gradient, we fix an average composition for the shell and then we choose a composition variation in the structure. The two extremes of the composition gradient are then obtained by adding, or subtracting, the composition variation to the average value chosen for the nanowire. Again, this induces the bending toward the right side, where the tendency to expand to reduce the elastic compression is weaker if compared to the other side of the shell.

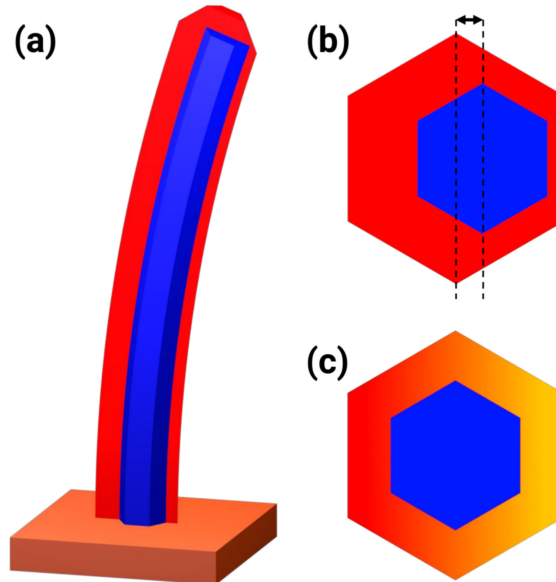

Figure 4.3: A schematic concept drawing illustrating the structure of the studied nanowires. (a) WZ GaP/$In_xGa_{1-x}P$ core/shell NW. Blue: WZ GaP core. Red: WZ $In_xGa_{1-x}P$ shell. The nanowire is bent due to asymmetry in the shell, which can be of two types: (b) thickness asymmetry, which we model as a displacement (shift) of the core with respect to the center of the shell, and (c) compositional asymmetry, where the orange (right) side represents a lower In composition than the red (left) side. We model the composition as varying linearly between the two sides. Here we define the composition variation as the difference between the maximum and the average In composition. (from Ref. [175])

4.3.2 Comparison between simulations and experiments

We now apply the numerical model to an experimental case study. We have chosen, among all the nanowires studied by TEM, to focus on a representative case (already reported in Fig. 4.2) with a high bending and a clear measured asymmetry both in composition and in shell thickness. In this way, we have the opportunity to test the validity of the model by checking if it is quantitatively reliable in reproducing the bending or if some additional parameter has to be considered. In the inset of Fig. 4.4a we report a sketch summarizing how the NW is partitioned: a 2.5 μm long top part with 175nm of thickness, a 5.5 μm long lower part with 190 nm of thickness. A 2 μm long central section is added to connect the two, with linearly varying thickness in order to avoid discontinuities in the FEM simulation. The asymmetric thickness and composition of the shell are set according to the numerical values measured by EDX and reported in Table 4.1. The additional central section is modeled by interpolating with continuity the values for the top and bottom sections.

In Fig. 4.4(a), the resulting equilibrium shape for the bent nanowire, as obtained by the FEM model, is compared to the TEM image for the NW studied. As a first result, we can conclude that the model if capable of reproducing the bending of the NW. In panel (c) the hydrostatic strain is shown for three cross sections, representative of the three segments used to model the NW. The first result is that, overall, the core volume has a tensile strain (red color), while the shell a compressive one (blue color). This is in agreement with what is expected when the lattice parameter of the shell is larger than the one of the core, as in this

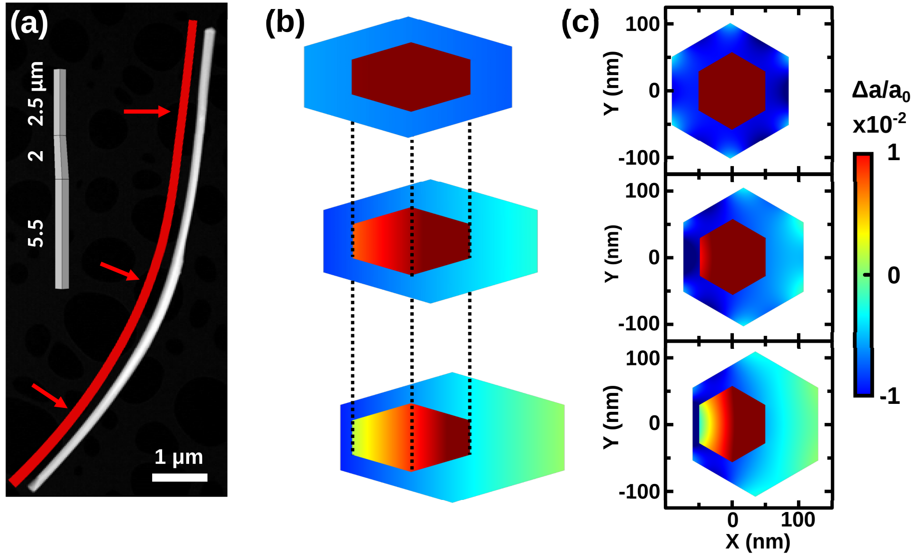

Figure 4.4: (a) A comparison between FEM simulation (red) and a TEM HAADF image of the WZ GaP/$In_{0.2}Ga_{0.8}P$ core/shell NW. The inset shows the three segments used for the FEM simulation. The central segment was used to avoid discontinuities in the model. (b) Plots of the axial strain in the three segments of the NW to illustrate the elastic deformation along the length of the nanowire. The colour scale is the same as in (c). (c) Hydrostatic strain (sum of radial, tangential and axial) plots in the three segments of the NW. The degree of asymmetry in the shell clearly affects the asymmetry in strain distribution. In the bottom segment, the left side of the core is subject to compressive strain, while the right side is almost completely relaxed. Only elastic relaxation is considered in the simulation. (from Ref. [175])

system. By a deeper analysis of the strain maps, we recognize that the elastic relaxation is not the same for the different cross sections, as a consequence of the different asymmetries. In particular, where the asymmetry in composition and shell thickness is more evident, the strain relaxation is enhanced, as it is evident in the bottom section. In particular, the most peripheral 20 nm of the shell, close to the free surface on the right of the bottom section, have a nearly zero-strain condition. Additionally, the asymmetric deformation in the shell induces, as a consequence, an asymmetry in the strain distribution of the core. The enhancement in the strain relaxation on one side of the nanowire is a direct consequence of the bending of the structure, which allows for a larger expansion on the convex side (right). This can be highlighted by considering the axial component, shown in panel (b), which represents the deformation along the axis of the nanowire. This deformation is higher where the residual strain is lower, i.e. on the right side of the nanowire. From these results, we can then conclude that the description of the bending by means of the elasticity theory is fully consistent with the behavior observed experimentally.

4.3.3 Comprehensive analysis of nanowire bending

While we have confirmed that the FEM model is able to reproduce the bending of a nanowire, we still have to prove the applicability of the FEM model as a predictive tool useful for the experiment analysis. Indeed, to the present development of the model, the only additional information that we get by simulations is the distribution of the residuals strain,

but the TEM and EDX analysis cannot be avoided. To that purpose, we investigate more in detail the relationship between the bending and the shell asymmetries, together with the core and shell sizes, in order to find a correlation between these variables. Initially, we start from mapping the NW curvature as a function of the core diameter and the shell thickness, defined as the average between the two extremes sides of the shell. To limit this analysis only to these two structural variables, we fix the composition and thickness asymmetries. In particular, we set an average In concentration equal to 25% with an asymmetry of 5%, which means that on one side the In concentration is equal to 20% and on the other side is 30%. Similarly, we fix that the core displacement is set equal to 1/4 of the average shell thickness. These parameters have been chosen because they are, on average, representative of the set of NW analyzed in details by TEM (here not reported).

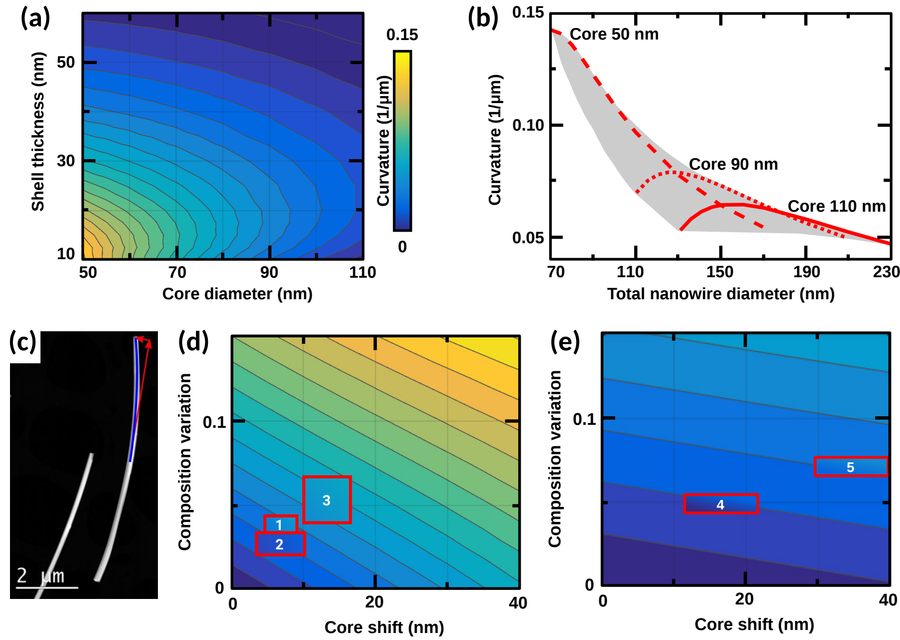

Figure 4.5: (a) The calculated curvature of a WZ GaP/In$_x$Ga$_{1-x}$P core–shell NW as a function of the average shell thickness and core diameter. The average composition is x = 0.25, with a composition variation of ±0.05. The core shift is 1/4 of the shell thickness. The colour bar indicates the NW curvature and is also used for (d), (e). (b) Distribution of the nanowire curvature (grey area) as a function of the total nanowire diameter, based on the data from panel (a). The trend not only depends on the total diameter, but also on the core diameter. The red curves outline the curvature for three core diameters. (c) A HAADF image of two WZ GaP/In$_x$Ga$_{1-x}$P NWs grown under the same conditions, clearly showing bending. The curvature is measured by interpolating the NW geometry with a parabola (blue line) and by computing the second derivative of this function in the centre of the NW. The red arrows are a guide to the eye to indicate the bending- induced displacement of the tip. (d), (e) The calculated curvature of WZ GaP/In$_x$Ga$_{1-x}$P NWs as a function of composition and core shift, with overlaid experimental data (red rectangles). The numbers are used to identify the NWs, as reported in Table 4.2. The size of each red rectangle represents the experimental error on the two axis dimensions. The colour gradient in the rectangle represents the error on the experimental curvature. Parameters: (d) core 100 nm, shell 50 nm, average x = 0.25. (e) Core 100 nm, shell 160 nm, average x = 0.60. The comparison between calculated and experimental data yields very good agreement. (from Ref. [175])

The resulting curvature map is shown in Fig. 4.5(a), where the axis report the core

diameter and shell thickness and the color scale quantifies the curvature of the nanowire. The latter is measured as an average curvature by interpolating the shape obtained by the FEM simulation with a parabola and by evaluating the second derivative halfway along the nanowire axes (see panel (c) for the same procedure applied on a TEM image). For the sake of simplicity, the asymmetry is set to be constant along the axis. As a consequence, we notice that analysis is independent on the length of the nanowire, provided that it is not of the same order of magnitude of the NW radius.

If we consider a fixed shell thickness, we observe that the curvature decreases as the core diameter increases. This can be explained by considering that the larger is the core, the higher is its stiffness, i.e. the resistance to the bending which is induced by the elastic deformations of the surrounding shell. On the other hand, a similar behavior cannot be recognized by fixing the core diameter and by changing the shell thickness. Indeed, initially the increase of the shell thickness tends to enhance the bending of the nanowire, as the larger volume of the shell can exert a stronger force to bend the core. However, when the shell grows further, an unexpected decrease of the curvature is observed. This can be explained by considering that a larger shell both has a stronger bending force, but also increases the stiffness of the total structure. This means that the rotation of the structure could in principle improve the relaxation in some regions of the shell, but at the same time requires and additional shell compression in other regions, making the bending less favored overall.

The increased stiffness for the larger shell suggests a possible relationship between the total NW and the bending, with the idea that the larger is the NW and the lower is the tendency to bend. However, this simple idea cannot be applied straightforwardly as multiple aspects have to be considered. This is better illustrated in Fig. 4.5(b), where the curvature values used to plot the map of panel (a) are represented as a function of the total nanowire diameter. We can correctly find, as suggested before, that the curvature becomes larger when the NW is thinner, as in this case less elastic energy is required to bend the structure. However, a spreading of the relation between curvature and NW size is observed for larger diameters. To understand this latter behavior, we plot three distinct curves, corresponding to three core diameters. This makes clear that it is not sufficient to know the NW total diameter to infer on the bending, but also the size of the core is a quantity to be considered. Indeed, as already discussed in panel (a) for a fixed core diameter, the bending is smaller when the shell is thinner, then it rises up to a maximum value to finally decrease with the further thickening of the shell. This is because a larger nanowire requires a larger elastic energy, or more precisely an asymmetry of the elastic deformations, to bend the whole structure. This analysis suggests that a possible solution to reduce, up to negligible curvature value, the bending of ternary core/shell nanowires could be to grow graded shells. In particular the grading is useful to keep a low lattice mismatch in the initial shell layers, to reduce the tendency to bend the structure when its stiffness is low, due to the small total diameter. Then the composition could be increased up to the value required for applications, because the bending is hindered by the already thick shell. Such a strategy is preferred to the use of a thick core, which in principle could lead as well to a low curvature. However, the

lower compliance of a large core reduces the elastic relaxation in the shell, favoring plastic relaxation mechanisms which introduce defects in the system, as for misfit dislocations.

The final result that we can get from the comparison between the FEM model and the experimental results is to develop a diagnostic tool to correlate the observed curvature with the asymmetries in shape and composition of the nanowires. To this goal, we collect the structural parameters of a set of nanowires by TEM and EDX, as shown in Fig. 4.5(c) for the curvature and as reported in Table 4.2 for the thickness and composition. These data are directly compared with a curvature map obtained by the FEM model, as a function of the core shift and of the composition variation, as shown in Fig. 4.5(d,e). The two panels differ for the shell thickness, core diameter and average composition that characterize the two sets of NW that were analyzed. The experimental data are plotted on the map as colored rectangles. Their lateral size represents the experimental uncertainty on the measure of the asymmetries, while the color map inside the rectangles quantifies the curvature: the variation of the color corresponds to the uncertainty on the measure of the curvature. The main color map in the background corresponds to the values predicted by the FEM model. From both panel (d) and (e), a good agreement between the simulation results and the experimental data is achieved, as demonstrated by the correspondence between the color inside the experimental rectangles and the corresponding FEM background (the numerical values are reported in Table 4.2). This confirms that the FEM modeling is an accurate predictive tool to study the degree of shell asymmetry in a core/shell system with a lattice mismatch between the material of the core and the one of the shell. While the FEM calculations, in principle, show that a single curvature value could be achieved by different combination of shell thickness and composition asymmetries, the comparison with experiments highlights that both mechanisms are equally present. Indeed, the experimental rectangles are located approximately on the diagonal of panels (d) and (e), indicating that there is no NW which is bent just due to a shell asymmetry or a compositional one. Actually, the two mechanisms can be considered as related, since an initial asymmetry in the shell thickness can be produced by a lower elastic chemical potential on a side of the nanowire, which is also favoring the migration of the larger In atoms, rather than the Ga ones. In conclusion, by supposing a fair equipartition in compositional and thickness asymmetries, it is actually possible to predict the degree of overall asymmetry just on the basis of simple

NW n.	Composition	Shell thickness (nm)	Core shift (nm)	Composition variation	Measured curvature ($1/\mu$m)
1	27%	32	6 ± 4	$4 \pm 2\%$	0.055 ± 0.01
2	24%	47	7 ± 3	$3 \pm 1\%$	0.025 ± 0.01
3	26%	42	12 ± 7	$6 \pm 3\%$	0.060 ± 0.01
4	58%	170	17 ± 7	$4 \pm 1\%$	0.02 ± 0.01
5	61%	155	35 ± 5	$7 \pm 1\%$	0.04 ± 0.01

Table 4.2: Experimental data gathered with TEM from the WZ GaP/InGaP core–shell NWs considered in this study. We also compare the measured curvature with the curvature predicted by the FEM simulations. These results are visualized in Fig. 4.5(d,e).

SEM measurements of the NW bending.

4.4 Conclusions

In this Chapter we have quantitatively investigated the origin of bending in WZ GaP/In$_x$Ga$_{1-x}$P core-shell NWs and we have proposed a predictive tool to estimate the asymmetry in a core-shell NW structure. Indeed, by measuring the bending in a nanowire, for example by a simple SEM analysis, we can determine a small range in the asymmetry in shell thickness and composition. Since we have shown that the NW curvature is due to such inhomogeneity, this should be avoided in those applications where uniformity is required. Based on our finite element method analysis, we propose a strategy to limit the bending which consists in growing a graded buffer shell with a composition ranging from the one of the core to the one desired for applications, provided that the grading does not hinder much the devices performances. Indeed, in this way, a gradual elastic relaxation can be initially provided by the core/shell structure while growing the shell. Then, once the shell thickness is high enough to limit bending by the increased stiffness of the nanostructure, the composition in the shell can be increased without making the nanowire bend much, even in the presence of small asymmetries in the growth process. Moreover, due to the elastic relaxation in the buffer shell, it could be also possible to limit the nucleation of misfit dislocations, which makes nanowire a promising solution with respect to planar geometries to host lattice-mismatched heterostructures. This work has been developed on WZ GaP/In$_x$Ga$_{1-x}$P core-shell NWs, but, in principle, it can be extended to any kind of core/shell NW system, provided that the elastic constants of the materials are properly defined for the finite element calculations, and some experimental TEM data are available for the initial setup the modeling tool.

Chapter 5

Elastic strain relaxation in Ge/GeSn core/shell nanowires

In the previous Chapter 4 we have investigated the bending of nanowires, which is a structural phenomenon in core/shell NW which is already apparent when they are analyzed at SEM. In this Chapter, we investigate materials properties which are accessible only by a TEM analysis, as the alloy composition in the shell of a nanowire and the residual elastic strain, but which still can affect the performances of the possible technological applications. In particular, we focus on the Ge/GeSn core/shell nanowire system and by finite element method static simulations, combined with transmission electron diffraction measurements, we will estimate the residual misfit strain when a radial Sn gradient in the shell and a Ge segregation at the nanowire facet edges are present. By exploiting the simulation results, we will correlate the elastic relaxation of the lattice parameter mismatch with the incorporation of Sn above the equilibrium solubility and we will provide a detailed explanation of the role of the nanowire core in the strain relaxation mechanism.

5.1 Introduction

The direct bandgap is a crucial property for optical devices, often achieved by III-V semiconductors. However, the possibility to have good optical properties with group IV semiconductors would be welcomed, due to the wide use of Si in the current technological applications. Among the group IV, GeSn alloys are a promising solution to provide a good flexibility to independently tune the bandgap, still having a control of the lattice parameter mismatch [186–188]. The direct growth of GeSn on Si substrates would be an important advantage to achieve cost-effective and scalable Si photonics, targeted to operate at mid-IR wavelengths of 2-5 μm [189]. However, there are two main obstacles for this possibility. First, there is a large lattice parameter difference between Ge and Sn, which leads to a strain up to 15% [190], which results in the formation of a high density of defects [191, 192]. Moreover, the residual compressive strain in the GeSn alloy can affect the band structure, thus requiring an increase of the Sn content needed for a indirect-to-direct bandgap transition [187, 191, 193]. Therefore, specific growth strategies have to be developed in order to overcome the

strain issue, to enable the fabrication of efficient mid-IR optoelectronic devices [190, 194]. The second big challenge in the growth of GeSn alloys comes from the low equilibrium solubility of Sn in Ge, which is approximately equal to 1% [195]. In particular, the difference in the surface energy densities, combined with this extremely low solubility, tends to favor the Sn segregation and precipitation on the surface while growing the GeSn alloy [196–198]. To overcome this latter problem, in the literature [192, 199, 200] several methods have been proposed, based on out-of-equilibrium growth conditions and aiming at maximizing the strain relaxation. Indeed, strain is expected to play a role also in the incorporation dynamics, similarly to what was already reported for AlGaN alloys [201]. For the planar growth on Ge substrates, the main approaches developed so far are based on the management of the strain relaxation by plastic relaxation[202] or by increasing the compliance of the substrate via a Ge buffer layer [187, 191]. For instance, graded GeSn layers were demonstrated to achieve up to 16% Sn content [203]. The main drawback of these techniques is that plastic relaxation, involving multiple types of dislocations, is a difficult-to-control mechanism, and in particular the threading arms which eventually reach the top layers are detrimental for the applications.

To overcome these limitation, core/shell Ge/GeSn nanowires have been proposed as a promising solution [204, 205] as they permit a fully elastic relaxation. As we will discuss in detail in this chapter, this is made possible both by the elastic compliance of the Ge core and by the effect of free facets at the nanowire sidewalls. Reasonably, the increased Sn content observed in experiments [204] could be related to an enhancement in strain relaxation, as a similar effect has been reported for the case of GeSn layers grown on a planar substrate with a tunable lattice parameter [206]. It is the goal of this Chapter to investigate this hypothesis, studying in detail the interplay between strain and Sn incorporation with respect to the growth of the GeSn shell on a pure Ge nanowire, in a core/shell structure. In Section 5.3 we present an accurate characterization of the residual strain in the core/shell nanowire structure. This is not a trivial task to be performed experimentally, as the order of magnitude of the typical strain in these structures (of the order of 10^{-3}) is close to the accuracy limit of TEM. Moreover, what makes this system complex is the variability of strain, which depends locally on the non-uniform Sn distribution in the shell, which has been mapped by Energy-Dispersive X-ray (EDX) measurements. In particular, segregation along the edges of the shell and a Sn gradient along the NW radius are observed. Our work provides a theoretical approach capable of quantifying the elastic relaxation on the nanowires. This analysis is performed by finite element calculations and compared to dedicated TEM measurements for the strain. This has enables us to find a correlation between the strain relaxation during growth and the Sn incorporation in the shell. Finally, in section 5.4, a detailed study of the role of the core in the strain relaxation of the shell is presented by finite element results. All the growth experiments and the measurements have been performed by the group of Prof. Bakkers at Technische Universiteit Eindhoven. In particular, the growth was performed by Simone Assali, while the TEM studies by Marcel A. Verheijen.

5.2 GeSn growth issues

The growth of GeSn layers on planar substrates is generally affected by the development of defects. A main source for these is the lattice mismatch between the GeSn alloy and the substrate. An estimation for this mismatch can be based on the lattice parameters for bulk Ge and α-Sn. From these, by exploiting the Vegard's law, the lattice parameter for the GeSn alloy can be estimated. By considering that for lasing application a composition at least equal to 13% of Sn is requested, it results that a mismatch of about $\sim 1.9\%$ has to be accommodated by the system during the heteroepitaxial growth. As for other group IV semiconductor as Ge and Si, there are two ways to achieve strain release: elasticity and plasticity. The former, in the low temperature regime required to prevent Sn precipitation, can't profit of a Stransky-Krastanov growth mode and is limited to the tetragonal distortion. In this configuration, the lattice can deform elastically toward the free surface, but it is constrained to the lattice mismatch strain for the in-plane direction, where no free surface allows for an elastic relaxation. Therefore, the high residual elastic energy, that is stored in the GeSn layer during growth, can induce the formation of defects as misfit dislocations, including edge and threading dislocations, stacking faults and twin boundaries. These can provide an efficient relaxation of the compressive strain in the epilayer, but the major drawback is their detrimental effect on optical and electronic properties.

5.2.1 Equilibrium solubility of Sn

Beside the issues that arise from the lattice mismatch, the growth of a GeSn alloy is made more complex also by the low solubility of α-Sn in Ge. Indeed, in equilibrium conditions, the solubility of Sn is reported to be 1.1% [195], which is well below the target of about 13% which is required to have a direct band gap. The solubility decreases when considering SnGeSi alloys, down to a value of 0.1% [207] in a pure Si crystal. For these reasons, an out-of-equilibrium growth condition is required to obtain the desired Sn concentration. In particular, it is crucial to avoid phase separation caused by surface segregation or bulk precipitation. The former is particularly active due to the lower surface energy of Sn. The two main strategies to suppress this unwanted phenomenon are to grow at low temperature, to reduce the probability of atom exchange between the bulk and the surface, and to grow at high deposition rates, freezing rapidly the Sn atom in a bulk state. Indeed, bulk precipitation is less active during the growth, and could become more relevant in case of post-processing techniques as the rapid thermal annealing.

5.2.2 Ge/GeSn core shell nanowires: experimental details

Core/shell nanowires can be exploited as an alternative solution for growing heteroepitaxial GeSn. The aim of using such a structure is to exploit the larger free surface area. Indeed, for applications in Mid-IR detector it would increase the active surface capable of collecting the optic signal. But the main advantage of using nanowires is related to the growth, where the core template can offer peculiar properties, inaccessible by planar substrates. In this Chapter, we focus in particular to the elastic relaxation mechanism,

which is key to achieve a GeSn growth nearly defect free.

The growth was performed by CVD using germane (GeH_4), tin chloride ($SnCl_4$), and hydrogen chloride (HCl) as precursors [204] . The core is made of pure Ge and it is grown on a Ge (1 1 1) wafer for 2 h at 320 °C, reaching a length of $\sim 5\mu$m, exploiting the vapor-liquid-solid technique catalyzed by a gold droplet. The diameter of the core, which is an important parameter for this system as it will be discussed later, can be tuned from 50 nm to 100 nm by changing the size of the initial droplet. This technique allows also for a precise control of the NW positioning in regular arrays. The shell is grown in a second stage, where the temperature is reduced at about 300 °C using a $GeH_4/SnCl_4$ precursor ratio of about 740 °C. Additional HCl is used in the growth chamber to control the tapering of the nanowire and to prevent the overgrowth of the shell in the top part.

5.3 Strain tunability by core/shell nanowires

A first set of information about the growth quality can be deduced by an SEM analysis. In particular, the growth was optimized by looking at the morphology of the shell surface, in order to achieve smooth sidewalls, with a low tapering in order to guarantee uniformity in the NW and to prevent macroscopic Sn segregation in droplets. This first part was performed by the growers essentially by changing the partial pressures of the precursor and by changing the temperature. Then, a more detailed analysis involving TEM and FEM simulations is required to investigate the Sn incorporation and the elastic properties of the system.

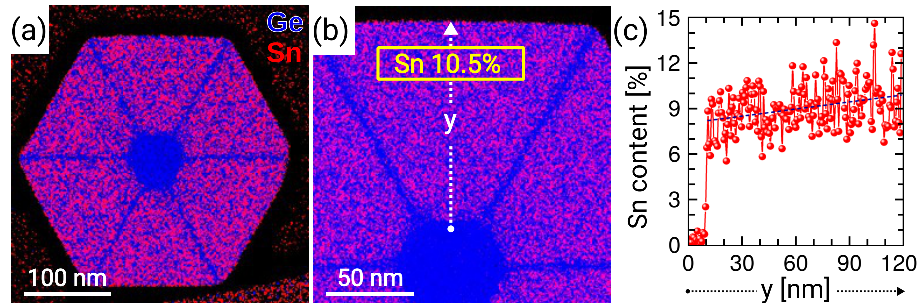

Figure 5.1: (a) Cross-sectional EDX compositional map of a $Ge/Ge_{0.895}Sn_{0.105}$ core/shell NW. The core radius is 30 nm and the shell thickness is ~110 nm. A nominal shell composition of 10.5 ± 0.5% in Sn is estimated by averaging the EDX signal within the yellow rectangle reported in the magnified view in panel (b). (c) Variation of the Sn content along the NW radius "y" showing the progressive increase of the Sn amount in the shell (dashed tendency line). (from Ref. [208])

The experimental group, that worked on the growth, prepared thin lamellae from the grown nanowires by FIB to be analyzed by TEM. In particular, by exploiting EDX, a precise estimation of the Sn distribution in the shell was achieved, demonstrating the validity of the growth recipe to get a sufficiently high Sn incorporation, well above the equilibrium value. In particular, as shown in Fig. 5.1(a), a cross-section with an hexagonal shape was found, with six {1 1 2} facets perpendicular to the substrate. The main feature visible from this overview is the formation of Sn poor stripes moving from the core to the hexagon

vertexes, forming a sunburst-like structure. By averaging the Sn concentration over the yellow rectangle highlighted in panel (b), a composition of 10.5% was achieved in this sample. However, the more important result of this analysis, that will be particularly useful to characterize the strain dependent Sn incorporation, is reported in panel (c). A clear gradient of Sn concentration is found in the shell, moving perpendicularly to the core. Despite the relatively small variations of composition (from 8% to 10.5%), as we will show by FEM simulations, this is an important feature to consider for a proper characterization of the system. In particular, the highest composition is achieved close to the shell surface. In addition, from the EDX measurements, we can conclude that no local precipitation of Sn nor clustering are observed [204], probably thanks to a limited diffusion of Sn during growth.

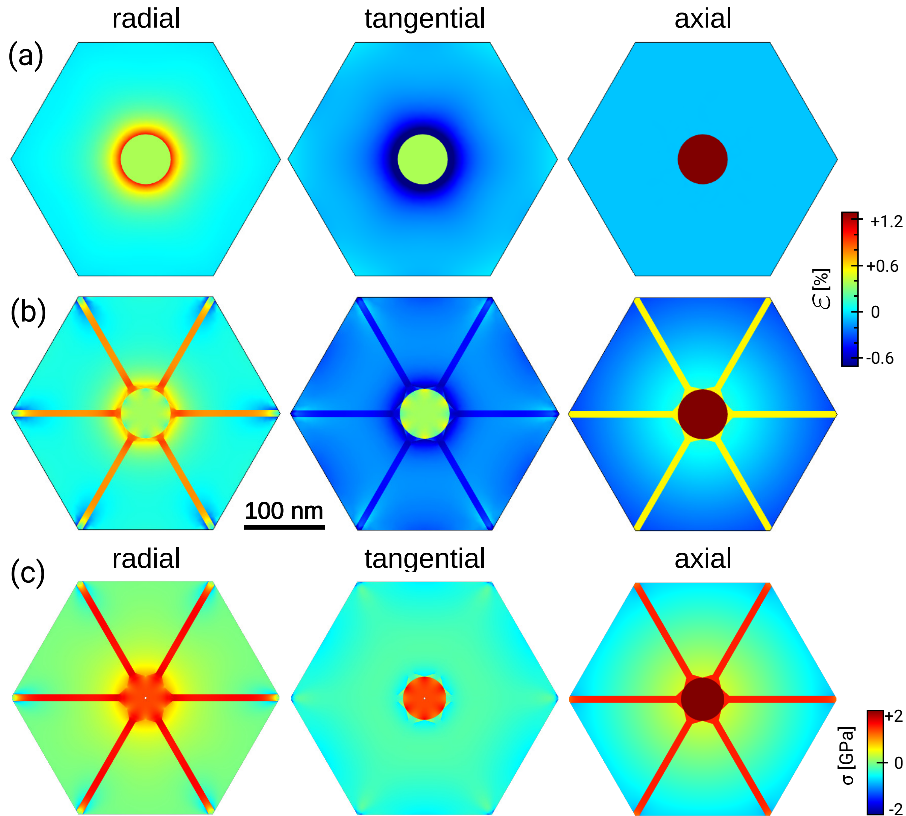

Figure 5.2: Color maps of the radial, tangential and axial components of the strain field, as computed by FEM. (a) A uniform 9.6 % Sn composition is set in the shell. (b) A linear composition gradient from 8% to 10.5% Sn and 5% Sn stripes along the hexagon vertices are assumed in order to match the experiments. (c) Stress maps for the case in panel (b). (from Ref. [208])

The first step of our analysis is to study the strain relaxation of this core/shell nanowire structure. We expect that the 3D substrate, made by the Ge core, allows for a better relaxation than a planar substrate. It is important to have a precise quantitative estimation for it, as it affects both the band structure and, more importantly, the tendency to nucleate defects. To this purpose, we have solved the mechanical equilibrium problem by the FEM, in the hypothesis of pure elastic deformation as formalized in Chapter 3, as no defect is observed in the NW analyzed by TEM [204]. The nanowire is modeled as a cylindrical core surrounded by an hexagonal shell. Core diameter (50 nm) and shell thickness (120 nm) are

set according to the cross-section in Fig. 5.1. The composition is set in two different ways. In a simplified model, to have a clear idea of the core/shell relaxation mechanisms, we set a uniform composition of Sn in the shell equal to 9.6%, which corresponds to the average of the composition measured by EDX in the whole shell. In addition to this preliminary model, we have also studied the case with the actual composition gradient (from 8% to 10.5%) in the shell and with the sunburst structure, made of 5% Sn stripes. To reasonably handle the strain tensor, we focus on the three main components, radial, tangential and axial, which are representative of the axial symmetry of the NW. In Fig. 5.2 we report the color maps of the strain and stress components for the two models here considered. In panel (a) the Sn composition is uniform in the shell, and as a result also the strain is nearly constant in the whole shell volume. Variations are visible for the radial and tangential components only in the region close to the core boundary. As predicted by analytical formulae [151], the axial and tangential components are compressive, due to the lattice mismatch between GeSn and Ge, while the radial one results to be tensile, according to the Poisson ratio. Indeed, the compression in two directions causes a dilatation toward the free surface perpendicular to the radius. To be more precise, also the axial component can profit of the free surface of the top of the nanowire, but it is not free to relax as the shell is bounded to the core, and an expansion of the former requires also the latter to expand. However, since the Ge is in elastic equilibrium at a smaller lattice parameter than GeSn, the core opposes to the axial expansion. Finally, the tangential component is mainly limited by the ring geometry of the shell. For a quantification of the strain, the three components, averaged in the shell volume, are reported in Table 5.1.

The NW system however is more complex than the simple uniform-composition case, suggesting that a numerical model is needed and that analytical formulas are not sufficient to get a quantitative value for the residual strain in the nanowire. Indeed, by looking at the color maps in Fig. 5.2(b), the strain distribution is not uniform as described by the simple model. This is particularly true for the axial component, where a color gradient develops radially, resembling the gradient that was measured for the Sn composition. Additionally, the sunburst structure introduces in the system strain variations in the regions nearby the Sn poor stripes. Looking at the numerical values in Table 5.1, the residual strain for the tangential and axial components is larger for the realistic model, if compared to

		Radial	Tangential	Axial [1 1 1]
uniform composition	shell	0.12%	-0.06%	-0.06%
	core	0.39%	0.39%	1.39%
composition gradient + sunburst	shell	0.12%	-0.19%	-0.13%
	core	0.38%	0.37%	1.33%

Table 5.1: Average strain values from FEM calculations, for the case including the Sn composition gradient and sunburst-like stripes as in Fig. 5.1 and the case of a shell with a uniform composition of 9.6%. The averages are computed in the core volume and in the surrounding shell volume by considering the central portion of the NW, as long as 1/4 of the total NW length. The volume of the sunburst-like stripes is excluded from the averages.

the uniform-composition one. The role of the sunburst structure, similarly to the core, is to oppose to the tendency of the shell to expand axially and radially, as shown by the tensile stress in the sunburst stripes in Fig. 5.2(c), resulting in an additional stiffness of the core/shell system than what is expected for an ideal system. Differently, along the tangential direction the shell can profit of a small transfer of the strain to the sunburst stripes, acting in this case as a compliant feature rather than as a stiffening element and thus resulting in a uniform stress within the shell. In any case, the important message from this FEM results is that the residual strain in the NW is rather small. Indeed the multiple mechanisms for relaxation, involving the expansion toward both the lateral and the top free surfaces, provide an efficient relaxation, at least if compared to the planar case of heteroepitaxial growth.

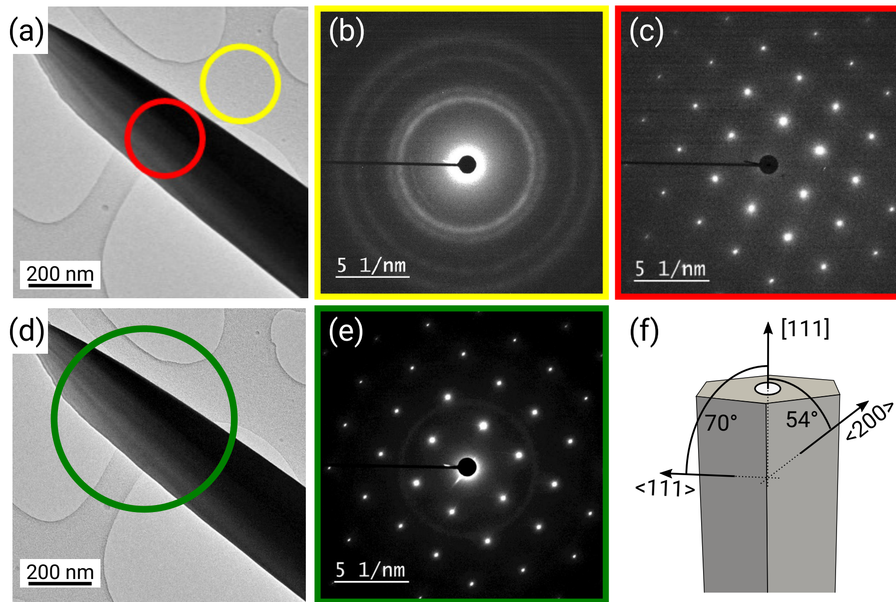

Figure 5.3: (a) Bright field TEM image of a GeSn NW disposed on the TEM grid for the strain measurement by external calibration, separating (b) the diffraction pattern of the Pt nanoparticles alone and (c) the NW diffraction pattern. The circles represent the diameters and positions of the selected-area electron diffraction apertures. (d) Bright field TEM image of the GeSn NW on the TEM grid for strain measurement by internal calibration, superimposing the signals from both the Pt nanoparticle and the NW in the diffraction pattern (e). The sample is the same as described in Fig. 5.1. (f) Schematic representation of the directions along which the strain is determined. (from Ref. [208])

To confirm the model, an experimental measure of the strain can be useful. However this is challenging, as a geometrical phase analysis [209, 210] requires a reference area within the same field of view, therefore cannot be applied to our 3D system. A possible alternative is to exploit the electron diffraction (ED) patterns from the TEM measurements to estimate the lattice spacing, and then deduce the strain. TEM measures were performed by imaging along the $\langle 1\,1\,0 \rangle$ zone axis, which enables to evaluate the strain along $\langle 1\,1\,1 \rangle$ and $\langle 2\,0\,0 \rangle$ directions. To improve the precision of the measure, reducing systematic errors inherited by the measuring technique, we have used Pt nanoparticles as a reference. These where deposited on the supporting holey carbon film where the wires were put for the

measure, as shown in Fig. 5.3(a). This calibration technique can be used in two different manners: external and internal. In the former, the poly-crystalline ring patterns from the Pt nanoparticles are acquired in a dedicated spot, as shown in Fig. 5.3(b). Then the nanowire is probed (see panel (c)) and then the signal is corrected by using the Pt signal as a reference. Differently, in the internal calibration mode, the Pt signal is acquired in the same spot as in the nanowire (see panel (d-e)).

The lattice spacings provided by TEM correspond to the [1 1 1] axial direction, to a $\langle 1\,1\,1\rangle$ direction tilted of 70° with respect to the axis and a $\langle 2\,0\,0\rangle$ direction tilted of 54° (see panel (f)). For the first case, the resulting strain is directly comparable with the axial strain in the simulations. On the contrary, a rotation of the strain tensor is required to compare with the tilted directions, as formalized in section 3.1.

From each lattice spacing, the lattice parameter can be calculated by using the same conversion factors as for the cubic cell of Ge. Then, the strain is computed by comparing with the lattice parameter obtained by the Vegard's law [211] for the GeSn alloy: $\varepsilon = \frac{a_{measured} - a_{\mathrm{GeSn}}}{a_{\mathrm{GeSn}}}$. From each electron-diffraction (ED) pattern, we can get a single spacing for both core and shell, as no double spot can be distinguished in the pattern. Nevertheless, we assume that the signal corresponds to the shell as its volume is more than 10 times larger than the one of the core. In any case, we have a single value for the entire shell, while we expect a different strain between the regions close to the core and the ones close to the free surfaces. Moreover, the composition is not uniform, as demonstrated by experiments, but we have to choose a single value (here we use the average composition 9.6% Sn) to calculate by Vegard's law a_{GeSn}, which is required for the computation of the strain. By considering the variability of the results, probably caused by the complexity of the composition and strain distribution, an error of 0.01 Å on the lattice spacing is estimated, which corresponds to a variability of about 0.3% in strain.

Table 2 reports the comparison between the TEM strain values and the FEM ones, elaborated by projecting the strain tensor along the three directions here analyzed: axial [1 1 1], $\langle 1\,1\,1\rangle$ and $\langle 2\,0\,0\rangle$. It is notable that both calibration methods have a non-negligible variability of the data, even if we can conclude that the internal calibration gives results closer to the FEM predictions. Anyhow, overall we have the indication that the residual strain in the nanowires is rather low, if compared to preliminary estimations already present in the literature [204]. Moreover, we have the clear indications that FEM simulations are a quite essential tool for a quantitative analysis of strain in NW, as the complexity of the system and the low magnitude of the strain to be measured make difficult to reduce further the variability of the experimental data.

Besides the characterization of the strain relaxation in core/shell nanowires, the main aim of using FEM simulations is to study the possible correlation between strain and Sn incorporation. Indeed, this topic is interesting not only for fundamental research, but also for the applications, where the control of the Sn incorporation is crucial. As already identified in the color maps of Fig. 5.2, the strain in the shell is not uniform, especially in the case of non uniform composition. Indeed, the lattice parameter of the GeSn alloy to be accommodated by the shell expansion increases while moving from the core to the shell

		Axial [1 1 1]	⟨1 1 1⟩	⟨2 0 0⟩
FEM	uniform composition	-0.6%	-0.03%	-0.03%
	composition gradient + sunburst	-0.13%	-0.05%	-0.07%
TEM	NW 1 external calibration	-0.5%	-0.5%	-0.6%
	NW 1 internal calibration	-0.6%	0.0%	-0.3%
	NW 2 internal calibration	-0.2%	0.5%	0.0%

Table 5.2: Comparison of the strain values obtained by FEM calculations and TEM measurements. FEM results are reported for both the case of a shell with uniform composition of 9.6% and the case including composition gradient and sunburst stripes, as in Table 5.1. The strain tensor is projected along the axial [1 1 1], ⟨1 1 1⟩ and ⟨2 0 0⟩ directions to compare with TEM data and averaged on the same shell volume as in Table 5.1. TEM data are acquired by both external and internal calibration techniques. In the latter case, measurements from two different NWs from the same sample (labeled as NW1 and NW2) are reported to show the uncertainty of the strain data, due to the 0.3% inaccuracy in the strain value derived from the electron diffraction patterns

surface. These variations are studied more in detail in Fig. 5.4, where the strain components are considered along a radius of the NW ('y'). In this case, to target the analysis to the most relevant case for applications, we have used the composition values for the highest Sn incorporation (13%) reported in Ref. [204]. Panel (a) reports the simple model with a uniform Sn composition of 11.7%, a core diameter of 50 nm and a shell thickness of 120 nm. The most noticeable thing is that, in this case, all the strain components converge to zero while approaching to the free surface. By looking more in detail, the axial strain is nearly constant, as it depends mainly on the volume balance between the core and the shell, but not on the distance from the core. On the contrary, the tangential strain is relaxed better far from the core. This is mainly due to a geometrical reason: a radial expansion when the radius is larger corresponds to a larger expansion tangentially, while the inner regions of the shell are more constrained to the core size, which opposes to the deformation. The radial tensile expansion can then be interpreted as a direct consequence of the compression in the tangential direction, due to the Poisson's ration. The strain distribution changes significantly when considering the actual Sn distribution observed in the experiments, which includes both a gradient along the radius from 9% to 13% and the sunburst stripes, with a 5% Sn composition (see panel (b)). Radial and tangential components keep a similar behavior, converging to a lower value when approaching to the free surface. This is due again to the geometrical limits of the tangential expansion. However, in this case, the strain does not converge to zero as the Sn composition, and hence the lattice mismatch, increases close to the surface. But the main impact of the non uniform Sn distribution can be found on the axial components, which is even tensile in the region close to the core. Indeed, while for a uniform composition the axial strain is determined by the balance between the core and the shell, in this case the inner shell (poorer Sn content) acts similarly to the core and opposes to the expansion of the outer shell. Finally, the role of the sunburst if to increase the stiffness of the whole structure, opposing as the core to the tendency of the shell to expand.

To get more deeply in the understanding of the strain role during growth, we have to

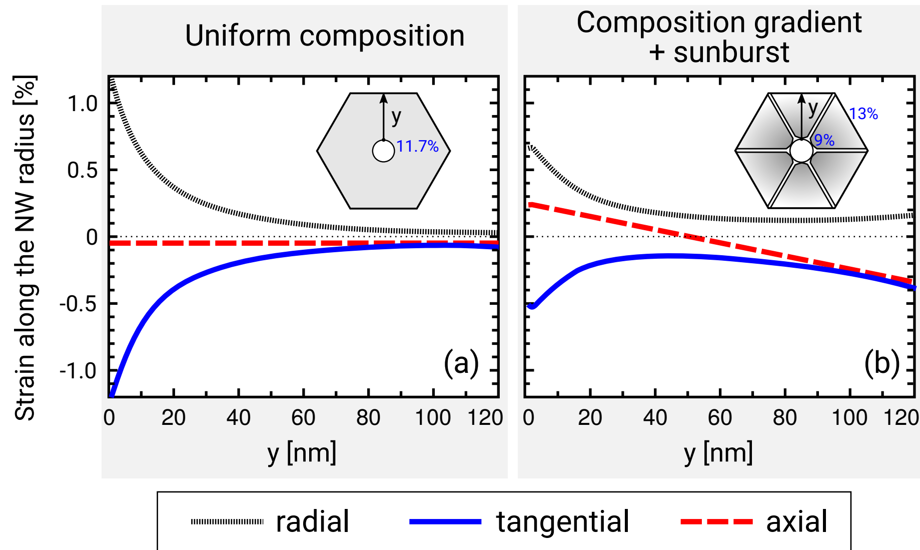

Figure 5.4: Variation of the radial, tangential and axial strain components along the NW radius "y" (see insets) obtained by FEM calculations in the case of uniform composition (a) and in the presence of composition gradient and sunburst segregation (b). The core radius is 25 nm and the shell is ∼ 120 nm thick. In (b) Sn composition varies linearly from 9% to 13% for a 120nm thick shell, corresponding to an average of 11.7% as used in (a), and 5% Sn sunburst stripes are also taken into account. (from Ref. [208])

investigate the strain at the NW surface, where the Sn incorporation mechanisms are active. This has to be repeated for several shell thicknesses, as to reproduce different stages of the growth process. As in the previous case of Fig. 5.4, we compare the two different models for the composition: uniform and gradient combined with sunburst structure. To have a representative value of the compression on the surface, we average the strain on a side facet in an area as wide as 1/3 of the total facet width. This guarantees to have a sufficient number of mesh points to average on, limiting the numerical uncertainties that could arise in the data processing. When the uniform composition is considered, all the strain components tend to decrease when the shell thickness increases, as shown in Fig. 5.5(a). The residual strain at the surface reaches a value below 0.2% when the shell is about two time thicker than the core. This can be generally explained because the larger is the shell volume, the stronger is the possibility to expand the core, accommodating the GeSn lattice parameter. This is particularly true for the surface where, as shown in Fig. 5.4(a), the strain reaches the lowest values. In the more realistic case where both the composition gradient and the sunburst structure are considered (see panel (b)), the tendency to reduce the strain when increasing the shell is maintained, but the strain does not tend to converge to a nearly zero value. A tendency to stabilize on a constant strain is recognized, despite any further increase of the shell volume. At a first look, this condition would make the NW an unfavorable system for GeSn growth. However, we must consider that, beside the constant strain, the system is accommodating an increasing Sn composition. This behavior is clearly unfavorable from the point of view of the energetics of the system, as both the Sn incorporation above the equilibrium solubility and the non-zero residual strain does not represent the minimum

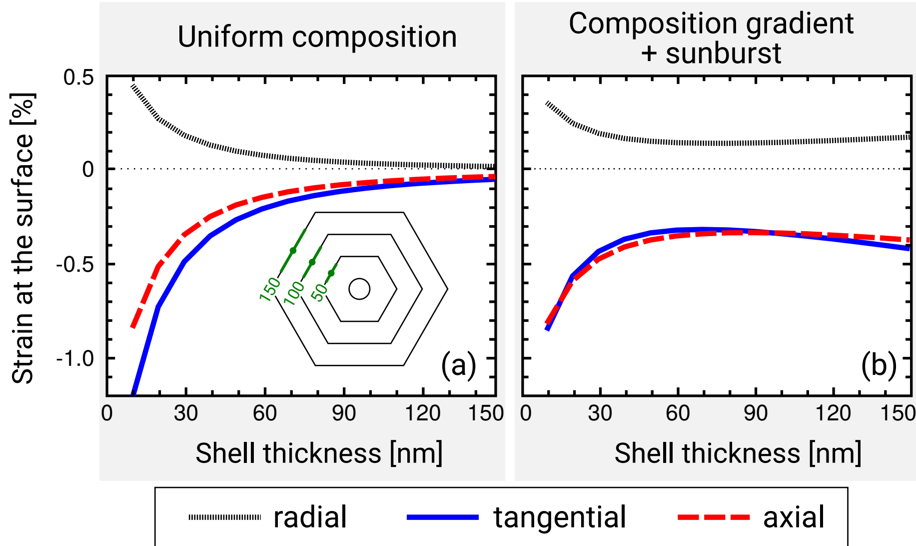

Figure 5.5: Comparison for the strain at the surface computed for different thicknesses of the NW shell. The strain values are averaged in the central 1/3 portion of the NW lateral surface, 750 nm far from the NW top. The core radius is 25 nm. In (b) Sn composition varies linearly from 9% to 13% for a 120nm thick shell, corresponding to an average of 11.7% as used in (a), and 5% Sn sunburst stripes are also taken into account. (from Ref. [208])

energy configuration. Therefore, the growth of GeSn nanowires must have a kinetic origin. The growth process is performed in excess of Sn, which pushes the incorporation of Sn in the alloy. Moreover, the low temperature and the relatively fast deposition rate allow for an out-of-equilibrium growth. However, the fact that the Sn incorporation is still limited may suggest that an additional limiting factor should be considered. The variability of the Sn incorporation during growth, under the same growth conditions, may suggest a dependence with strain. The tendency to incorporate more Sn, as pushed by the growth conditions, has to be balanced by the capability of the structure to accommodate the lattice parameter keeping a low residual strain. In other words, to incorporate more Sn, the nanowire has to grow larger. The quantity of Sn that is incorporated should keep the strain below a certain threshold, above which the tendency of the system would be to segregate Sn on the surface, reducing the strain in the surface layers. Following this model for the growth dynamics, the strain threshold mechanism can be recovered in the FEM model by looking at the tendency of the strain at the surface to stabilize (around the 0.4% value) when the shell grows thicker and incorporates a growing concentration of Sn. It has to be noticed that, in our case, the analysis is valid for a $\{1\,1\,2\}$ surface, as this is the only one exposed by the nanowire shell analyzed experimentally.

5.4 Core diameter and strain relaxation

An additional structural variable provided by the core/shell system is the diameter of the Ge core. Here we want to investigate whether this introduces and additional degree of freedom in the optimization of the epitaxial growth of GeSn layers. As a comparison, in

planar growth a similar role is played by the exploitation of virtual substrates to tune the lattice parameter of the substrate on which GeSn is grown [192].

From experiments performed by S. Assali at Technische Universiteit Eindhoven, it is found that smaller cores lead to the growth of a thicker GeSn shell. In addition, the surface of the shell presents better defined {1 1 2} facets, if compared to the larger cores where a multi-faceted shell is obtained. To understand why the incorporation of material is different between the two cores, in the hypothesis of a strain mediated Sn incorporation, here we compare the strain relaxation for the two systems.

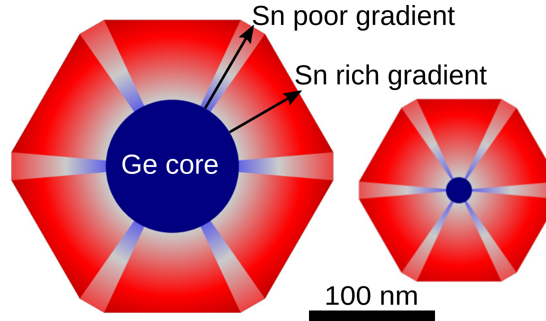

Figure 5.6: Schematics of the morphology modeled by FEM when changing the core diameter. A linear composition gradient from 8 % up to 13 % Sn for a 60 nm shell (6 % to 10 % Sn in the stripes along the hexagon vertices) is assumed in order to match the experimental data. The cylindrical core is of pure Ge.

A quantitative determination of the strain distribution in cross-sectional TEM samples of Ge/GeSn core/shell NWs using electron diffraction is challenging, especially for the case of thick cores, and therefore thick nanowires (>100 nm). Therefore, we apply the FEM method to estimate the elastic strain in core/shell nanowires to study the role of the core diameter. The core is modeled as a cylinder, as no clear faceting is observed neither for small nor for larger core. Moreover, by introducing a faceted core with sharp edges, the risk is to introduce a numerical divergence of the elastic field to the presence of perfectly sharp edges, which are not realistic of the actual system. The shell is bounded by six {1 1 2} facets, plus six {1 1 0} smaller ones. Indeed, in the system with a larger core diameter, a more irregular shell growth us found and a dodecagonal shell can be observed. A second difference with the system considered in the previous Section 5.3 is represented by the composition distribution in the shell. In addition to the {1 1 2} composition gradient, a Sn gradient is measured along {1 1 0} especially for larger cores. To have a representative model of the system, we include both gradients in the simulations, as shown in Fig. 5.6, with the same composition increase with shell thickness for the different core diameters, not to introduce too many different parameters between these system. In particular, along the $\langle 1\,1\,2 \rangle$ stripes the Sn content varies from 8% to 13% for a 60 nm shell, while along $\langle 1\,1\,0 \rangle$ the corresponding gradient is from 6% to 10%.

Despite the additional composition gradient introduced in this model, with respect to the one studied in the previous section, the strain relaxation in the nanowire has the same characteristic features as analyzed before. Along the radial direction, the shell can expand freely toward the free surface. On the contrary, along the tangential direction, the shell is

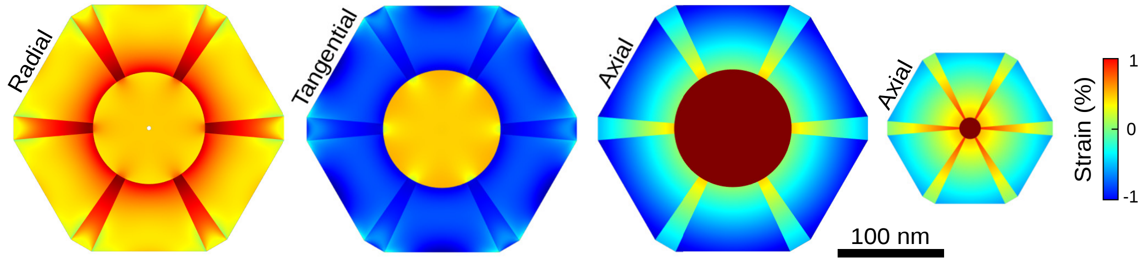

Figure 5.7: Color map of the tangential (a) and axial (b) FEM strain components for a 110 nm core diameter and a 60 nm thick shell. Axial strain for a 20/60 nm Ge/GeSn core/shell NW heterostructure, highlighting a tensile strain in the inner part of the shell. The composition is set as described in Fig. 5.7.

bounded by a ring symmetry around the core, therefore it remains compressed as shown by the color map in Fig. 5.7. As an additional phenomenon, which however has a minor effect on the strain relaxation, the tangential strain is partitioned between the Sn rich and Sn poor stripes. Along the NW [1 1 1] axis, on one side it can expand toward the top free surface, but on the other side it is tied to the length of the Ge core. Moreover, the tendency of the shell to elongate is twofold. Indeed, the Sn poor regions in the shell tend to expand less than the Sn rich ones, reducing the overall tendency of the shell to stretch the core. Still, a tensile deformation of the core is present, as it can be seen by the color map in Fig. 5.7.

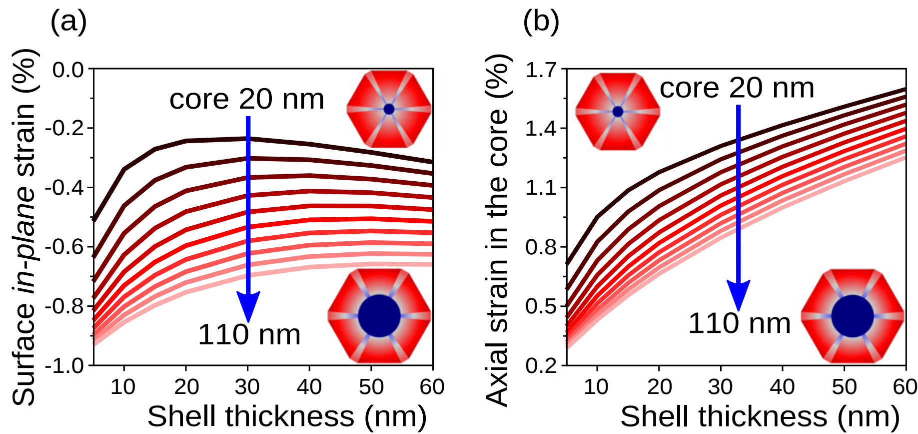

Figure 5.8: (a) In-plane strain (average of tangential and axial components) at the surface of the shell as a function of the shell thickness, for different core diameters. (b) Axial strain averaged in the core volumes for different core diameters. The composition is set as described in Fig. 5.8.

To investigate the possible role of strain in controlling the growth rate of the GeSn shell, it is possible to investigate the properties at the surface by FEM for different shell thicknesses, mimicking the sequential stages of the growth. In Fig. 5.8(a) the strain on the surface are reported as a function of the shell thickness. Different curves represent different core diameters. The strain has been computed by averaging the tangential and axial components, which resemble an in-plane strain on the surface. This is a measure of the compression of the unit cell, which could drive the segregation of Sn atoms on the surface, limiting the incorporation of material and, as a consequence, the shell growth rate. By this analysis, a large increase in the compressive strain from -0.2 % to -0.8 % is observed by

changing the Ge core diameter from 20 nm to 110 nm, which corresponds to the actual experimental range. This maximum variation is observed for a shell thickness of about 20 nm. Indeed, larger shells have an increasing strength to stretch the core, due to the increased GeSn volume.

An interesting feature regarding the axial strain relaxation in the regions close to the core can be highlighted by comparing the strain analysis for different core diameters. The inner part of the shell, having a lower Sn composition, may have even a tensile strain. This is because it is acting like the core as a compliant substrate for the outer shell, which has a larger volume and a stronger tendency to expand, having a higher Sn content. This is particularly evident in the color map in Fig. 5.7 for the NW with the smaller core (20 nm), which can be easily deformed by the surrounding shell. The axial deformation of the core is quantified in the plot of Fig. 5.8(b). It is evident that the residual strain is always tensile, and it magnitude is higher when the core is smaller, and therefore can be easily deformed by the surrounding shell. The same analysis for the radial and tangential components, which for the core volume have the same average value being the deformation nearly hydrostatic in the plane perpendicular to the NW axis, gives a similar trend, but on a lower strain scale, ranging from 0.05 % to 0.45 %.

5.5 Conclusions

In this Chapter we have analyzed by realistic 3D FEM calculations the residual elastic strain and the Sn incorporation in core/shell Ge/GeSn NW. This analysis has been compared to TEM results for the residual strain, still close to the accuracy limit. The simulations have revealed in particular the impact of the sunburst segregation and of the Sn incorporation gradient on the elastic properties, inducing a stiffening of the shell with respect to the case of uniform composition. More importantly, a strain threshold allowing for an incremental Sn incorporation has been identified for the $\{1\,1\,2\}$ NW facets by comparing the strain relaxation at the surface during growth and the resulting Sn distribution in the shell as measured by EDX. This corresponds to a mechanism of compositional pulling which is similar to the one identified for other systems, as AlGaN [201]. A correlation between strain relaxation, corresponding to the lattice parameter at the growing front, and the Sn incorporation has been proposed also in other recent literature works [206, 212]. An advantage of the analysis made on NW, where no dislocations are observed [204], is the possibility to quantify the residual strain as the result of a pure elastic relaxation, which is not possible in planar films growth where the plastic relaxation by misfit dislocations in unavoidable. For the NW system, we have also characterized the role of the core diameter, suggesting that the smaller Ge cores are more promising for an efficient strain relaxation in the GeSn shell, offering a possible strategy to improve the Sn incorporation in core/shell nanowires.

Chapter 6

Heteroepitaxial growth of islands on patterned substrates

In the Chapters 2 and 3 we have proposed an innovative modeling technique to simulate the growth of NM and a continuum elasticity approach to study the strain relaxation in core/shell NW. Here we combine these two aspects, surface diffusion and elasticity, by investigating the heteroepitaxial growth of islands on pit-patterned substrates by phase-field simulations. A system that has been widely studied in the literature, but which still requires the development of a modeling technique which can precisely capture all the aspects of this type of growth. Here in particular, we study the dynamics which results from material deposition and redistribution via surface diffusion, according to the tendency toward free-energy minimization. We apply a continuum model, based on the concepts proposed by the so called Asaro-Tiller-Grinfeld theory. In particular, we consider the balance between surface energy, misfit strain and wetting energy. The numerical solutions are obtained by finite element method, which permits to precisely account for the effect of the actual pit morphology on the strain relaxation. The mechanisms leading to islanding into the pit are discussed with respect to the growth conditions and pattern properties. Finally, as an additional result, the model is applied to study the case of island stacking.

6.1 Introduction

The growth of islands in semiconductor heteroepitaxy has been a research topic deeply investigated since decades [23, 213–215]. The first general understanding of the growth dynamics from a theoretical point of view was initially achieved by Asaro-Tiller-Grinfeld and Srolovitz with the well known ATG analytic theory [25–27]. By assuming that nucleation barriers do not play a major role [216], the ATG theory models how a strained film becomes unstable with respect to a profile perturbation, leading to the formation of a periodic array of islands. This process is explained by considering the competition between the surface energy cost, which favors the flattening of the surface, and the elastic relaxation of the strain, which induces the growth of islands. The growth dynamics occurs in quasi-equilibrium conditions, therefore it is reasonable to assume that it is driven by the minimization of the

free energy of the system. In the following years, several works were published with the aim to improve the simple ATG description by capturing multiple features observed in the experiments [114]. In particular, the modellization of the wetting energy was introduced [217–220], then surface energy anisotropy [220, 221], the mechanism of compositional mixing in alloy [222–225] and even plastic effects [226].

The technological interest to control the positioning and size of the growing islands has driven the scientific research toward the study of patterned substrates. One of the main approaches, that we are going to analyze in this chapter, consists in patterning the substrate with an ordered array of pits. Nowadays, this can be achieved thanks to reactive ion etching and to lithographic techniques [30, 227, 228], which enable an accurate control of the pattern properties, both in terms of pit positioning and of control of their size and morphology. Indeed, it has been demonstrated by experiments [229–233] that, under suitable growth conditions, a perfectly ordered array of islands can be grown. However, the challenging aspect of this procedure is that the growth parameter window that allows for such an ordered growth is limited and complex to be found. Indeed, growth temperature and deposition flux as well as pit size, shape and periodicity, all affect the localization and uniformity of the grown islands.

In the literature, some theoretical studies [29, 234] show that the growth temperature and the deposition flux as well as pit size, shape and periodicity, all affect the localization and uniformity of the grown islands. From one hand, the tendency of filling the pits is expected due to capillarity. On the other hand, the strain relaxation is particularly favored for the island that grows inside the pit [235]. And this, in analogy with the ATG theory, tends to drive the growth, opposing to a flat filling of the pit. An exact numerical modeling of this latter contribution is computationally quite demanding. Therefore, typically, only approximated approaches have been presented in the literature, particularly limiting the description to selected pit shapes with low aspect ratios [31, 236, 237].

In this Chapter, a general model based on a phase-field approach is developed in order to study the island growth on patterned substrates [113, 238, 239]. The main advantage of the present model with respect to the literature is the possibility to implicitly track both the film surface and the substrate interface. Within this description, a partial differential equations system is formulated to describe the growth dynamics of the system. This is solved numerically by exploiting finite element method, which allows us to deal with arbitrary substrate morphologies, including the ones used in experiments, still profiting of an exact solutions of the elastic relaxation, without the need of higher order approximations. For the sake of simplicity, here we focus on a pure elastic description with no plastic relaxation, even though phase-field models have been developed also to account for the presence of defects [240, 241].

Once the model is properly defined, growth simulations are performed to precisely identify the mechanisms driving the ordered growth of islands, with particular attentions to the parameters that mostly affect this dynamics. Here we have chosen to focus on the prototypical system where Ge islands are grown on a Si(0 0 1) substrate, within the approximation of isotropic surface energy and elastic properties, and neglecting intermixing

effects. However most of the conclusions can be extended to a wide range of Stranski-Krastanov systems, such as III-V compounds [215, 242], just by changing the material properties used in the model. Importantly, the results presented here are not limited to simulate the annealing of a film deposited on the substrate, but the growth dynamics is studied during the deposition of the material forming the growing layer.

This Chapter is organized with the definition of the phase-field model which couples surface diffusion and elasticity in Section 6.2. The role of the wetting energy term in determining a critical thickness for island formation is presented in Section 6.2.1. Then the growth of a single island in a pit is characterized by the detailed analysis of the free energy contributions in Section 6.3.1. Once the main growth dynamics has been assessed, further elements can be studied, as the impact of the growth conditions in Section 6.3.2, of the pattern geometry in Section 6.3.3 and of the elastic properties of the materials which compose the substrate and the growing film in Section 6.3.4. Then the model is used to perform full 3D simulations as described in Section 6.3.5. Finally a different type of ordering is presented in Section 6.4 as due to the vertical stacking of multiple layers with islands.

6.2 Phase-field model for island growth

To simulate the growth process, a phase-field model is exploited, combined with a finite element method to solve numerically the diffusion equations. The model has been developed starting from the one proposed by Rätz *et al.* in Ref. [113] and it has been improved to include the description of the substrate morphology. This approach is similar to the one presented in Ref. [221, 243, 244]. A phase-field model basically consists in an implicit description of the system morphology via an order parameter called phase-field function. In a general approach, this function varies with continuity within the domain considered for the simulation and, based on its numerical values, identifies the different topological regions of the system. In our case, we need to distinguish between three phases: the substrate, the film and the vacuum. The latter has to be accounted for, as the simulation domain is wider than the solid itself. This represents a main numerical advantage of this approach, because the simulation domain can be set a priori and does not evolve during the simulation, as it happens in the case of an explicit modeling, where the simulation domain directly corresponds to the free surface of the system. As illustrated in Fig. 6.1, two phase-field functions φ and c are used to distinguish between the different regions, instead of using a single function with multiple values. φ is set to vary smoothly from 1 in the solid to 0 in the vacuum. The surface of the solid corresponds to the diffuse interface where $1 > \varphi > 0$ and it is represented by the $\varphi = 0.5$ isoline, which in the following figures will be directly used to show the surface profile. Similarly, the substrate is represented by the value 1 of the c parameter, which is equal to 0 elsewhere. The substrate-film interface is reported as the $c = 0.5$ isoline. Since the SiGe system follows the SK growth mode, there is no need to consider also the substrate-vacuum interface. Indeed, the Si substrate is always covered by the Ge wetting layer. The mathematical definition of the phase-field function, used for both φ and c, is given by $1/2\,[1 - \tanh(3d(\boldsymbol{r})/\epsilon)]$ (see Fig. 6.1(a)), with ϵ the amplitude of the

interface region and $d(\boldsymbol{r})$ the signed-distance of a generic point $\boldsymbol{r}$ from the actual profile.

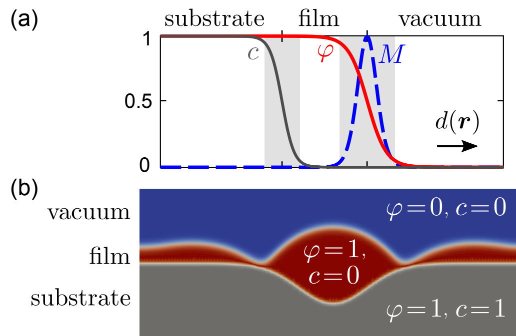

Figure 6.1: System representation by the PF approach. (a) Plot of the phase-field functions φ and c and of the surface mobility $M(\varphi, c)$ (scaled to unity) with respect to the signed-distance $d(\boldsymbol{r})$ from the surface and substrate profiles. Shaded regions correspond to the diffuse interfaces. (b) Definition of the substrate-film-vacuum regions by the φ and c fields within the simulation cell. (from Ref. [245])

The growth process can be reproduced by considering two main phenomena: material deposition and surface diffusion. Bulk diffusion, which in principle is active, is assumed here to be negligible due to high activation barriers that make this process at least two orders of magnitude slower than the surface one. For this reason, we consider that the substrate, which is always in the solid bulk region due to the existence of the Ge wetting layer, does not evolve in time (t). This introduces a fixed constraint on the phase-field function c ($\partial c/\partial t{=}0$) that allows to simplify the description of the dynamics by considering only the phase-field function φ. This assumption is particularly true when considering a Si substrate due to its rather low mobility if compared to the Ge one [246]. More precisely, both experimental and theoretical analysis [223, 247] showed that intermixing effects may involve also the first monolayers of the substrate when dealing with the initial few-monolayers-thin wetting layer. However, for the sake of simplicity, we do not include this complex dynamics [248] in the present model.

In the assumption of quasi-equilibrium conditions, the net flow of material on the surface is driven by the free-energy minimization. This is equivalent to consider a material transport in the direction of the local gradient of the chemical potential μ [249, 250]. Differently from the kinetic regime influenced by the adatom incorporation dynamics, here we are in quasi-equilibrium condition where $\mu = \mu_{eq}$ and the incorporation time is assumed instantaneous. The material transfer is quantified by the consequent variation of the surface profile. In our PF framework, the temporal evolution of the surface corresponds to the temporal variation of the φ function. This dynamics is mathematically represented by the degenerate Cahn-Hilliard equation for surface-diffusion, in which we have included an additional term $F(\varphi)$, accounting for the external material supply:

$$\frac{\partial \varphi}{\partial t} = \nabla \cdot [M(\varphi, c)\ \nabla \mu] + F(\varphi). \tag{6.1}$$

In this approach, the mobility coefficient consists in the function: $M(\varphi, c) = D(36/\epsilon)(1-c)\varphi^2(1-\varphi)^2$. Its value is non-zero only in the region close to the film surface, as shown

in Fig. 6.1(a). The numerical parameter D is an effective diffusion coefficient, which sets the time scale of the process. The diffusion equation (6.1), with this particular formulation of the mobility, ensures to determine a conservative dynamics [123] with no loss or gain of material, except for the source term of the deposition.

The external material supply is modeled as a vertical and uniform deposition flux $\boldsymbol{f} = -f\hat{\boldsymbol{z}}$, mimicking the conditions of molecular beam epitaxy, is assumed:

$$F(\varphi) = -(1+\mathcal{R})\ \boldsymbol{f}\cdot\nabla\varphi = -(1+\mathcal{R})\ f\frac{\partial\varphi}{\partial z}, \tag{6.2}$$

where f is the nominal deposition flux and $\mathcal{R} \in [-1, 1]$ is a random number, introduced to simulate local beam fluctuations. This is required in the initial stages of the growth to trigger the profile instability by setting the gradients of the chemical potential on the surface. Here the distribution of the flux is expected not to be crucial for the growth dynamics as we deal with structures characterized by a low AR if compared to the vertical growth studied in the previous chapters.

The chemical potential is defined as the functional variation of the total free energy G as $\mu = \delta G/\delta\varphi$ and corresponds to the energy gain/loss with respect to the addition or removal of an atom in a specific position of the profile. The free energy can be written in the form of a Ginzburg-Landau functional [10]:

$$G[\varphi] = \int_\Omega \gamma\left(\frac{\epsilon}{2}|\nabla\varphi|^2 d\boldsymbol{r} + \frac{1}{\epsilon}B(\varphi)\right) d\boldsymbol{r} + \int_\Omega \rho[\varphi, c, \boldsymbol{u}] d\boldsymbol{r}, \tag{6.3}$$

where $B(\varphi) = 18\varphi^2(1-\varphi)^2$ is a double-well potential.

The first term in the equation quantifies the surface energy on the system. This is determined by the product of the surface energy density and of the area of the surface profile. The second term of the equation corresponds to the elastic contribution to the chemical potential. This is determined by the elastic energy density $\rho[\varphi, c, \boldsymbol{u}]$, which is given by the surface and substrate morphology, via φ and c, and by the displacement field $\boldsymbol{u}$. The latter describes the local deformation of the crystal lattice $\boldsymbol{u} = \boldsymbol{u}(\boldsymbol{r})$ due to the film-substrate misfit strain $\varepsilon_{\mathrm{m}}^{\mathrm{fs}} = (a_{\mathrm{s}} - a_{\mathrm{f}})/a_{\mathrm{f}}$, with a_{s} and a_{f} the lattice parameters of the substrate and film respectively. For the Ge on Si system, $\varepsilon_{\mathrm{m}}^{\mathrm{fs}}$= -0.0399. By considering isotropic elasticity and introducing the elastic strain tensor $\boldsymbol{\varepsilon}$, so that $\varepsilon_{ij} = \frac{1}{2}\left(\partial u_i/\partial x_j + \partial u_j/\partial x_i\right) + \varepsilon_{\mathrm{m}}\delta_{ij}$, ρ is given by

$$\rho = \mu\sum_{i,j}\varepsilon_{ij}^2 + \frac{\lambda}{2}\left[\mathrm{Tr}(\boldsymbol{\varepsilon})\right]^2. \tag{6.4}$$

The material properties have to be defined on the whole simulation domain Ω as all the other variables of the system. To this purpose, the misfit ε_{m} and the Lamé coefficients μ, λ are interpolated with the function $h(\varphi) = \varphi^3(6\varphi^2 - 15\varphi + 10)$ from their values for the solid phase to 0 in the vacuum phase. Moreover, an additional modulation to distinguish between the properties of the substrate (at zero-misfit and with elastic constants μ_{s}, λ_{s}) and the ones of the film ($\varepsilon_{\mathrm{m}}^{\mathrm{fs}}$, μ_{f}, λ_{f}) is introduced by means of c:

$$\begin{aligned} \varepsilon_{\mathrm{m}} &= (1-c)\varepsilon_{\mathrm{m}}^{\mathrm{fs}} \cdot h(\varphi), \\ \mu &= [c\mu_{\mathrm{s}} + (1-c)\mu_{\mathrm{f}}] \cdot h(\varphi) + \mu_{\mathrm{v}}, \\ \lambda &= [c\lambda_{\mathrm{s}} + (1-c)\lambda_{\mathrm{f}}] \cdot h(\varphi), \end{aligned} \tag{6.5}$$

where μ_{v} is a small number $\sim 10^{-6}$ GPa, introduced for numerical reasons only [113] as perfectly zero elastic constants could cause numerically-divergent displacements. This apparently complex description of the elastic properties via the phase-field functions has the main advantage of enabling the simulation of whatever complex substrate or film geometry, still accounting properly for the different properties of the two materials. This feature is here exploited by considering the proper difference between the Si and Ge elastic properties: μ_{Si} = 52 GPa, λ_{Si} = 60 GPa while μ_{Ge} = 41 GPa, λ_{Ge} = 44 GPa. This model could be therefore efficiently applied also to other heteroepitaxial systems with compliant substrates where the evolution of the profile is strongly affected by the difference in the elastic properties between the film and the substrate [251].

The main unknown variable, that has to be determined in order to quantify the elastic contribution to the system free energy, is the displacement field $\boldsymbol{u}$. The most precise description would require to couple the surface diffusion dynamics in eq. (6.1) with the deformation dynamics. However, since the time scale for the elastic relaxation can be considered instantaneous with respect to the diffusion timescale, we can limit our study to a mechanical equilibrium problem to be coupled with the profile evolution dynamic. The problem of mechanical equilibrium of an elastic medium is well defined in the literature, as also discussed for core/shell NW in Chapter 3. The fundamentals consist in considering the equilibrium between all the elastic forces within the solid, that in differential form can be written as $\nabla \cdot \boldsymbol{\sigma} = \mathbf{0}$, with the stress tensor $\boldsymbol{\sigma}$ given by $\sigma_{ij} = 2\mu\varepsilon_{ij} + \delta_{ij}\lambda\mathrm{Tr}(\boldsymbol{\varepsilon})$. This relation is based on the linear Hooks law, in the hypothesis of small deformations. The partial differential equation for the displacement film reads:

$$\nabla \cdot \left[\mu\left(\nabla\boldsymbol{u} + (\nabla\boldsymbol{u})^T\right)\right] + \nabla\left(\lambda\nabla\cdot\boldsymbol{u}\right) = \nabla\left[(2\mu + 3\lambda)\,\varepsilon_{\mathrm{m}}\right]. \tag{6.6}$$

The numerical solution of the mechanical equilibrium for the Ge on Si system that we are going to consider is reported in Fig. 6.2. The boundary conditions are set on the borders of the simulation domain being periodic in all direction, but for the bottom of the cell (Γ_D), where the Si lattice is assumed to be not deformed and $\boldsymbol{u} = \mathbf{0}$ which allows to fix the reference frame for the numerical solution. For the definition of the boundary conditions, we are already profiting of a peculiar advantage given by the PF model. Indeed, if the solid profile were defined explicitly, Neumann boundary conditions $\boldsymbol{\sigma} \cdot \hat{\boldsymbol{n}} = \mathbf{0}$ should be applied at the free surfaces (Γ_N), to reproduce the zero-stress condition at the boundary with the vacuum region. In the PF model, this result is achieved automatically thanks to the interpolation of the elastic properties in the vacuum regions, which are treated as a medium with null elastic constants which do not exert any force on the solid surface. On the left side of Fig. 6.2(b), the solution of the strain component ε_{xx} is shown on the overall simulation

domain for a 2D slice cut through the island center. On the right side, the vacuum region, which has just a numerical value, but it is meaningless from a physical point of view, is clipped away and only the solid region within the $\varphi = 0.5$ isoline is reported. One numerical detail to be noticed is that, within the diffuse interface, the strain values are affected by the modulation of the misfit strain ε_{m} due to the $h(\varphi)$ function, highlighted in the figure. This is consistent with the diffuse description of the surface and it is demonstrated to converge to the expected value in the sharp-interface limit [32], which corresponds to $\epsilon \to 0$. To facilitate the readability of the physics, in the 3D views of the system, the profile is shown as cut at the $\varphi = 0.9$ isoline, $\sim \epsilon/2$ below the actual surface, in order to exclude the interface region affected by the numerical modulation, representing the physical strain expected at the surface.

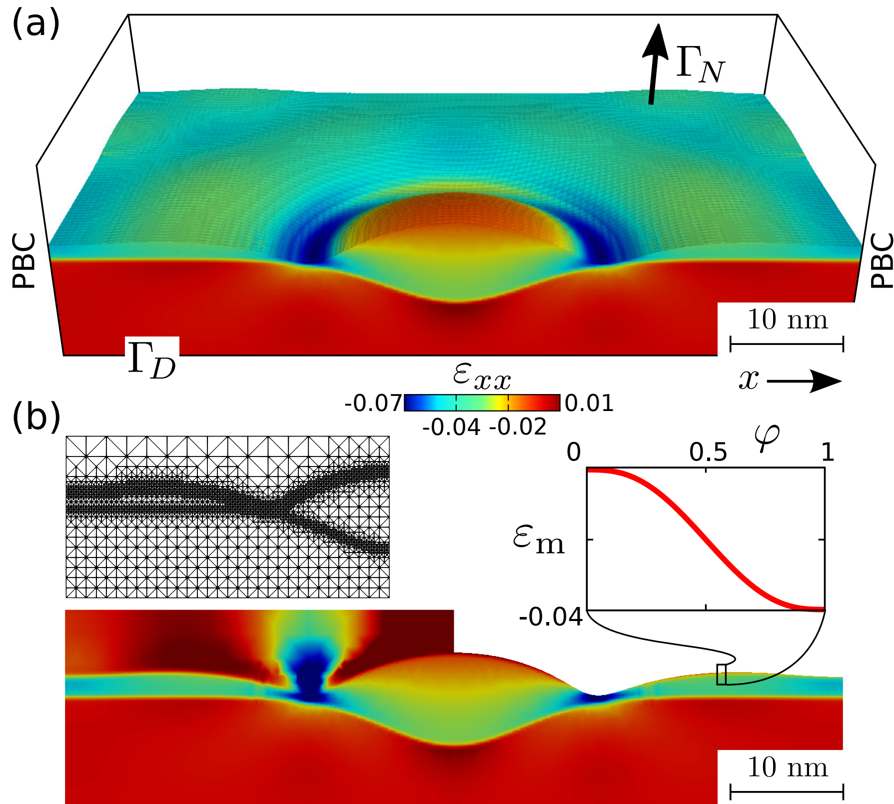

Figure 6.2: Strain field calculation by PF. (a) Color map of the strain component ε_{xx} for a 3D Ge island on a pit patterned Si substrate. Half of the simulation cell is reported to show the strain distribution within the film and the substrate in cross section. The surface is cut at $\varphi = 0.9$ in order to exclude the strain modulation due to the $h(\varphi)$ function. (b) Cross-section through the island center showing the full map of the strain field including the vacuum region (left) and the corresponding cut below the surface profile at $\varphi = 0.5$ (right). The modulation of the misfit strain ε_{m} at the film-vacuum interface is highlighted. The mesh used in the FEM calculation (for half of the profile) is reported in the inset, showing the local refinement at the interfaces traced by both φ and c. (from Ref. [245])

To determine the complete evolution, at each time-step of the simulation, the strain field at elastic equilibrium is calculated by solving eq. (6.6) and plugged into eq. (6.1) by the definition of the local chemical potential μ:

$$g(\varphi)\mu = \gamma\left[-\epsilon\nabla^2\varphi + \frac{1}{\epsilon}\frac{\partial}{\partial\varphi}B(\varphi)\right] + \frac{\partial}{\partial\varphi}\rho(\varphi, c, \boldsymbol{u}), \tag{6.7}$$

where the stabilizing function $g(\varphi) = 30\varphi^2(1-\varphi)^2$ has been introduced to improve the numerical stability of the solution, guaranteeing the convergence of this model to the corresponding sharp-interface limit for $\epsilon \to 0$ [113, 122].

6.2.1 Wetting energy and critical thickness

An important feature of the SK growth mode is the formation of a wetting layer, generally few MLs thick, above the substrate surface. Islanding occurs as a second stage of the growth above the WL, with the important property that the substrate is always covered by the material of the growing film, as we have already assumed in the model definition. This behavior can be motivated by considering the surface energies of the materials involved in the process, and in particular the top material has to have a lower surface energy density than the one of the substrate below. This is particularly true for the SiGe [252] system where $\gamma_{\mathrm{Ge}} \approx 6.0$ eV/nm$^2 < \gamma_{\mathrm{Si}} \approx 8.7$ eV/nm^2. Additionally, the interfacial energy is negligible and does not drive in any way the reduction of the Si-Ge interface, which would oppose to the full coverage of the WL. Ab-initio calculations [242, 253] revealed an additional interesting property of the SiGe system, for which the surface energy density of the growing film is not constant, but varies with the film thickness h. This behavior can be well fitted [217–220] by an exponential decay going from the surface energy density of the substrate γ_{s} at 0 ML to the one of the film γ_{f} in the limit of thick films:

$$\gamma(h) = \gamma_{\mathrm{f}} + (\gamma_{\mathrm{s}} - \gamma_{\mathrm{f}})\exp(-h/\delta). \tag{6.8}$$

A decay length $\delta \sim$ ML is chosen to return the bulk value γ_{f} when the film thickness exceeds 3-5 MLs, where this dependency with thickness becomes negligible.

The use of the wetting term has two consequences in the modeling of island growth. First, it determines a critical film thickness h_{c} below which the film is definitely stable even if it is strained. This is because each initial perturbation of the surface profile is flattened by the increased surface energy. In a linear approximation, for biaxial strain, it is possible to estimate [220, 254] $h_{\mathrm{c}} \approx -\delta \ln\left[(U_\varepsilon^2\delta^2)/(4\gamma_{\mathrm{f}}(\gamma_{\mathrm{s}} - \gamma_{\mathrm{f}}))\right]$, where $U_\varepsilon = \varepsilon_{\mathrm{m}}^2 \cdot 2\mu_{\mathrm{f}}(2\mu_{\mathrm{f}} + 3\lambda_{\mathrm{f}})^2/\left[(\mu_{\mathrm{f}} + \lambda_{\mathrm{f}})(2\mu_{\mathrm{f}} + \lambda_{\mathrm{f}})\right]$. The second result is that the increase of the surface energy density when, for any reason during the profile dynamics, the surface gets closer to the substrate provides a regularization of the profile instability. Indeed the higher energy reduces the tendency to dig toward the substrate. This tendency is generally recognized in the standard nonlinear ATG as a cusp singularity [255]. Thanks to the wetting energy modeling, the corresponding numerical divergence is avoided, achieving the possibility to simulate islands on top of the WL on a long-time scale, which includes the slow coarsening between neighboring islands [220].

These properties, due to the use of the wetting energy, are demonstrated in Fig. 6.3, where the evolution of a flat film is simulated during deposition. A value of $\delta = 0.27$ nm is considered in all the simulations here reported, leading to a critical thickness of $h_{\mathrm{c}} \approx 1.2$ nm.

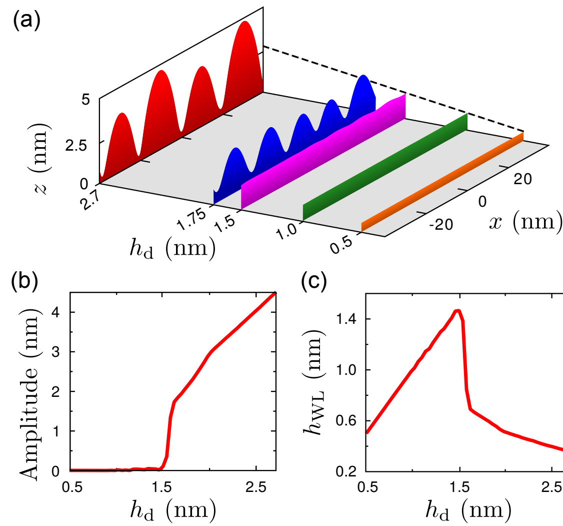

Figure 6.3: 2D simulation of island growth on a flat substrate during deposition (f/D $= 8\times10^{-4}$). Time is represented by the deposited material h_d. (a) Evolution sequence for the film profile. (b) Maximum peak-to-valley amplitude of the film. (c) Minimum film thickness, corresponding to the WL height h_WL. (from Ref. [245])

This slightly overestimates the value of the WL typically observed in the experiments (3-5MLs [256]). However, we have to accept this small discrepancy as by considering a lower δ we would have to tackle even thinner WLs, and this would require a more refined mesh that increases the computational cost. When the thickness h of the growing film is lower than the predicted h_c, the initial flat profile remains stable, despite the random perturbations that are induced by the deposition flux. This is highlighted in panel (b), where the maximum amplitude of the profile does not grow with time. Once the thickness becomes larger than h_c, the profile perturbations become unstable and the one with the fastest growth rate starts to become apparent, as predicted by the ATG model. This phenomenon occurs dynamically during the continuum deposition of material. Therefore a delay [223, 257] is required before the islands can actually become apparent, after the critical thickness is overcome. This delay is more relevant as the deposition flux is increased and, in the extreme case, can be responsible of the suppression of islanding due to the occurrence of plastic relaxation, before island formation can have a relevant effect on the elastic relaxation of the film. On the other hand, as shown in Fig. 6.3(c), an abrupt thinning of the WL is found when islands become apparent, and in particular when the growth rate of the perturbation becomes larger than the one of deposition. Indeed, at this stage, islands grow larger in volume and tend to dig trenches in the WL layer, reducing its volume. This process, as mentioned before, is stopped thanks to the wetting potential as soon as the WL thickness is smaller than the critical value h_c. By considering the parameters used for the simulation, we can quantify $h_\mathrm{WL} \approx 3$ MLs, which is in agreement with the experimental observation for Ge/Si. In the late evolution stages shown in Fig. 6.3(a), islands continue to grow on top of the WL, collecting material only from the deposition flux, until the coarsening dynamics [220] is triggered. This consists in the material transfer from smaller islands to larger ones, which guarantees a better strain relaxation, as it is expected for Ostwald ripening processes.

6.2.2 Computational details

The model described so far has been implemented numerically by exploiting the FEM toolbox AMDiS [17, 18], optimized for the phase-field approach. The main advantage of FEM is to provide an exact numerical solution for both the mechanical equilibrium problem and the diffusion dynamics. As shown in the inset of Fig. 6.2(b), the geometry of the system is defined by an adaptive mesh, which is finer at the free surface and at the film-substrate interface. These are the regions in the simulation domain where the material properties vary most and where the evolution dynamics occurs. In the other regions, and especially in the vacuum one, a coarser mesh is used to reduce the overall computational cost. The length scale considered in the simulation is the one of nm. To provide a sufficiently thin interface with a good mesh refinement (al least 8 points in the diffuse interface are required for an optimal convergence of the FEM solution), the widths ϵ of the free surface and of the film-substrate interface are set equal to 0.5 nm and 0.2 nm, respectively. The time scale of this process is totally determined by the numerical values associated to D as $\tau = D^{-1}$. The physical value of D can be estimated as $D = h_{\mathrm{l}} V_{\mathrm{a}} D_0 (kT)^{-1} \exp\left(-E_{\mathrm{b}}/(kT)\right)$, with h_{l} the ML thickness, V_{a} the volume per atom, D_0 the material diffusion coefficient, E_{b} the energy barrier for site hopping, k the Boltzmann constant and T the temperature. More precisely, in the Ge on Si system here reported, $h_{\mathrm{l}} = 0.146$ nm, $V_{\mathrm{a}} = 0.02$ nm^3, $D_0 = 8.5 \cdot 10^8$ nm^2/s [258], $E_{\mathrm{b}} = 1.1$ eV [259] and the typical growth temperature $T = 650°$C are assumed. With this set of parameters, $\tau \approx 0.03$ s, which means that the time of the deposition or annealing processes shown by the simulation results are on a reasonable time scale of minutes, which well corresponds to the one of MBE experiments. Most importantly, when considering a diffusion dynamics combined with a deposition process, the key parameter to consider is the relative time scale between deposition and diffusion, namely the f/D ratio. The time integration scheme used here is a semi-implicit one, with a time-linearization of the term $B'(\varphi)$ (see Ref. [10] for details). This allows us to consider relatively long time step, if compared to a fully explicit scheme, and we have exploited a dynamic adaptation of τ with values ranging between 10^{-1} - 10^{-2}, depending on the speed of the profile evolution.

6.3 Results and discussion

In this Section, we describe and discuss the result given by the PF simulations applied to the growth of heteroepitaxial Ge islands on pit-patterned Si substrates. In particular, the role of the deposition flux compared to the surface mobility, which respect to the pit sizes and pattern morphology will be analyzed. Moreover the geometrical and elastic properties of the pit are studied with respect to the ordering of islands. Finally, full 3D simulations are reported as a confirmation of the previous 2D results.

6.3.1 Island growth into the pit

The starting point is the understanding of the dynamical process which leads to the growth of an island inside the pit. This is the optimal condition of perfect ordering. Once this simple case is understood, the more complex scenario of islands growth both inside and

outsite the pit will be investigated. To this initial goal, 2D simulation are considered, in order to have both a simple picture of the system and to have a relatively low computational cost. The 2D plane is assumed to be an xz section of the 3D morphology (where z is the vertical direction), which corresponds to a biaxially strained film. The third y direction is considered infinitely extended, in order to avoid any contribution of material transfer from that direction. The pits are modeled as a V-shape, using here a 1:6 aspect ratio (AR), which is defined as the height-to-base ratio. This size has been chosen by considering the typical experimental conditions that favor the growth of islands inside pits [29].

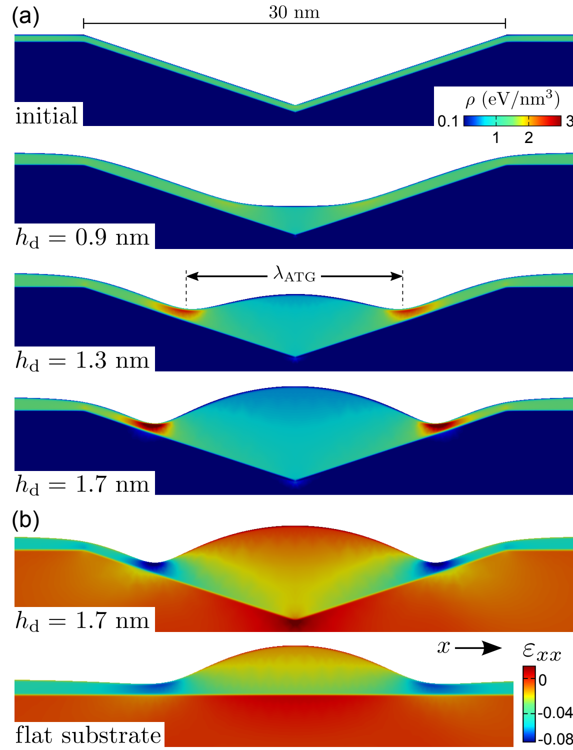

Figure 6.4: Simulation of island growth into a pit. (a) Evolution sequence during deposition ($f/D = 4 \times 10^{-4}$). The first profile, corresponding to the initial condition for the simulation, is set as a conformal 0.5 nm thick film. The color map for the elastic energy density ρ is shown. λ_{ATG} is shown for comparison. (b) Comparison of the strain map of the ε_{xx} component between the island grown into the pit and an equivalent one, with the same base and height, formed on a flat substrate. Only a portion of the 80 nm wide cell is reported. Figures are in 1:1 ratio. (from Ref. [245])

In Fig. 6.4(a) the time evolution of the island growth is shown. The initial film profile is set on a 30 nm wide pit, which is approximately two times wider than the instability wavelength $\lambda_{ATG} \approx 15$ nm expected from the ATG model. This condition was chosen to be on the safe side and to guarantee that, at least on a flat substrate, the island growth is achievable. The pit is surrounded by a 50 nm flat region, corresponding to the pit-pattern period, since boundary conditions are set on the two sides of the simulation domain. The initial Ge film is 0.5 nm thick, in order to be below the critical thickness h_c and to be able to assume a conformal shape with respect to the pit one, still without any island growth. The Ge deposition is considered at a constant vertical rate $f/D = 4 \times 10^{-4}$. This induces the growth of the island, as indicated by the three representative stages reported in Fig. 6.4(a),

identified by the different volume of deposited material quantified as $h_\mathrm{d} = f \times t$.

In the first stage of the growth, the main driving force is capillarity, which favors the flow of the deposited material inside the pit. This in motivated by the reduction of the exposed surface energy, minimizing the free energy of the system. However, it has be considered that there are two main contributions to the free energy. First the wetting-energy term opposes to the thinning of the WL, which is caused by the material transfer toward the pit. This is to avoid the increase in γ according to eq. (6.8). The second contribution is due to the elastic energy density of the system. However, as confirmed by looking at the color map in the figure, the elastic energy is rather uniform, which means that it does not induce any significant gradient for the chemical potential on the surface. The only variation of the elastic relaxation can be found in the bottom of the pit.

As far as the deposition continues, more strained material is fitted inside the pit. When the elastic energy stored in this volume becomes large enough, it induces significant variations of the surface chemical potential and leads to the growth of an islands, which is here shown for the $h_\mathrm{d} = 1.3$ nm growth stage. In this configuration, the additional surface energy cost given by the increased surface area is overcompensated by the enhanced strain relaxation which is promoted by the island morphology, with respect to the flat configuration. It is interesting to notice that the onset for islanding is anticipated to a lower h_d than the one expected for the growth on a planar substrate. This is important to guarantee that the surrounding WL regions, in a flat configuration, remain below the critical thickness h_c, suppressing any tendency to form islands.

The size of the island is almost comparable to the typical wavelength predicted by the ATG theory for a flat film, which confirms that the explanation of the island growth due to the balance between elastic relaxation and surface area is reasonable. The innovative result from the well known theory is that this wavelength is not maintained by the island, which tends to grow not only the amplitude, as predicted by ATG, but also to increase the base size while climbing on the pit sidewalls. This is again to optimize the balance between the total surface area, which would increase in the case of a fixed base width, and the elastic relaxation in the island. The improved strain release for bigger island volumes is confirmed by the color maps for the elastic energy density. The strain release mechanisms can be made more clear by looking at the strain maps, which give an information on the direction of the lattice deformations. In particular, in Fig. 6.4b, the strain ε_{xx} component is reported, which is the more representative of the in-plane compression of the system. The first clear information from these images is that the compression within the island is lower if compared to the surrounding WL, especially for the top region of the island. An higher compression is recognized at the borders of the island, where highly compressive lobes are found. A direct comparison with the corresponding case grown on a flat substrate is reported in the bottom of panel (b), where an island with the same AR is grown by a separate simulation. For a more direct comparison, the growth of an isolated island is triggered on the flat substrate, which keeps the surrounding WL flat as no random perturbation is initiated there. Again, the main result is that the pit induces a better strain relaxation overall. In particular the island top is almost fully relaxed, and this relaxation extends on a large volume toward

the bottom of the pit. As it was analyzed in the literature with static FEM analysis [235], this strain stabilization is due to the inverted-pyramidal volume below the island base, which can profit of the strain transfer toward the sidewalls of the pit structure, profiting of its compliance [260]. This strain relaxation mechanisms is active also in our simulations, as proved by the compressive lobes that result within the Si volume close the to the pit sidewalls.

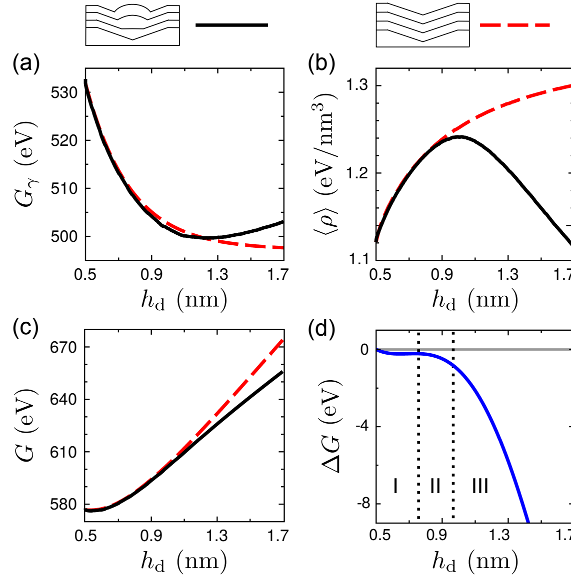

Figure 6.5: Plot of the energy contributions for the evolution in Fig. 6.4 (solid line), compared to a conformal growth (dashed line). (a) Surface energy G_γ, corresponding to the first integral in eq. (6.3) computed on the whole surface. (b) Elastic energy density ρ, averaged over the film volume. (c) Total free energy G including both film and substrate. (d) Difference in G between the two growth regimes here compared. I: quasi-conformal growth II: pit filling III: islanding. (from Ref. [245])

A deeper insight on the growth dynamics can be achieved by monitoring the energetics of the growing film. These data are reported in Fig. 6.5 by comparing two cases: the growth of the island inside the pit (by solid lines) and the reference case of conformal growth on the pit (dashed lines), where material redistribution is not allowed. This condition could be achieved, for instance, at low growth temperature [261] or high deposition rate. We analyze the two main contributions to the free energy, surface and elastic, together with the total free energy. In particular, panel (a) shows the surface energy G_γ. This quantity is obtained by integrating along the whole surface profile the first term of eq. (6.3). Panel (b) reports the elastic energy contribution, which is quantified by averaging the elastic energy density $\langle\rho\rangle$ over the stressed film volume, which is the active part for the island growth. Panel (c) draws the behavior of the total free energy G of the system. The increase of the total energy during the growth process apparently seems in contradiction with the statement that material redistribution is driven by the tendency to minimize the free energy. The complexity in our system arises from the continuous deposition of additional material on the surface. This causes an increase of the stressed material in the system and leads to an overall increase of the energy, but just due to the flux and not due to an anomalous surface diffusion dynamics. The energetic advantage of growing the island is made more clear in

the direct comparison with the reference case shown in panel (d), where the difference in free energy between the two cases, $\Delta G = G_{\text{island}} - G_{\text{conformal}}$, is reported. Three separate stages can be distinguished in this plot. As already shown in Fig. 6.5(a), the first part of the evolution (I) is characterized mainly by a decrease in the surface energy. This can be ascribed both to an initial thickening of the WL, which implies an exponential decay in γ according to eq. (6.8). The growth front evolves conformal to the substrate, except for the small rounding of the sharp tips set in the initial profile. Therefore the only energy variation that occurs is related to the variation of the wetting potential. The tendency to make the WL thicker contrasts the driving force toward pit filling. However, the energy gain due to the wetting potential decays exponentially as more material is deposited on the WL. Therefore, at subsequent stages, the material flow from the WL toward the pit is enabled. This dynamics allows the system to reduce the surface energy with respect to the reference case of conformal growth (II). The additional material that flows inside the pit produces a flattening of its bottom (see $h_{\text{d}} = 0.9$ nm in Fig. 6.4(a)), reducing the area exposed by the film surface. As a first conclusion, stages (I) and (II) are dominated by the surface energy contributions, while elasticity does not play a major role in determining the evolution dynamics. Still, the strain relaxation starts to be affected by the morphology of the film, producing a non uniform elastic energy density.

At variance from a tetragonally distorted flat film, which has a constant value ρ_{t} for the elastic energy density (equal to 1.38 eV/nm^3 for the case of Ge on Si) independent of the film thickness, the presence of the corner regions at the rims and at the bottom of a pit induces a non uniform strain field in the film, eventually providing a better strain release. As already observed in Fig. 6.4(b), this is also due to the strain partitioning between the film and the substrate. The limit of elastic energy corresponding to the flat film case is recovered for an infinitely thick conformal film on the pit geometry as illustrated in Fig. 6.5b. Indeed, when the volume of the film becomes larger, the relaxation mechanisms at its corner become negligible in the overall count of the elastic energy. However, the pit filling during the stage (II) of the growth enables an alternative path for the strain relaxation, mainly due to the inverted pyramid. Therefore, at some point, $\langle \rho \rangle$ is observed to decrease again, despite the continuous deposition of material. The effect of strain relaxation becomes the main driving force at stage (III), when the island grows into the pit. In this case, the cost for the increased surface is largely compensated by the enhanced strain relaxation within the island. As made evident in panel (d), a significant lowering in G is then obtained with respect to the conformal growth. This represents a proof that the growth of an island into the pit is a better pathway for the free-energy minimization.

6.3.2 The role of the growth conditions

Once the growth dynamics of a single island into the pit has been characterized, the model can be applied to study the role played by the growth parameters. Indeed, it is known from experiments that the perfectly ordered growth considered so far can be obtained only for a well defined range of growth condition [29]. In general, despite the pit seems to be the most favorable region to grow an islands, different processes can occur during the deposition,

leading to the formation of islands even outside the pit. This study is of practical interest, as the capability to control the formation and positioning of islands is crucial for application in uniform arrays.

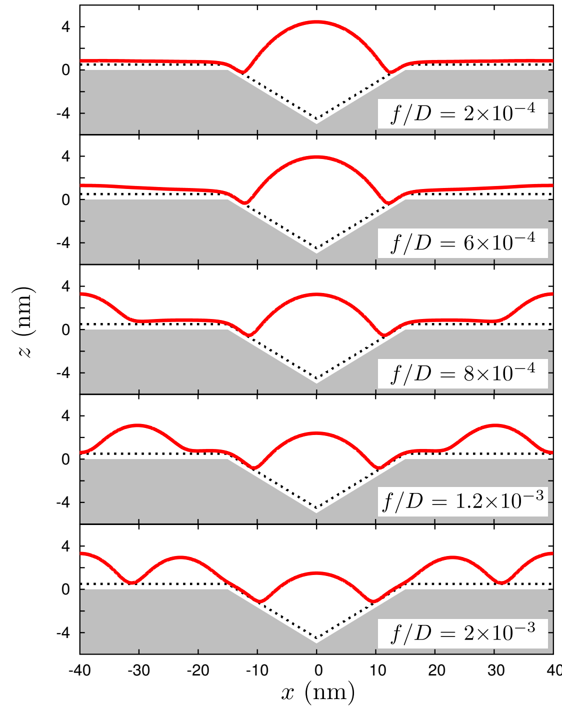

Figure 6.6: Role of the deposition-to-diffusion ratio f/D in the growth. The initial condition (dotted lines) is a conformal film, 0.5 nm thick, with the same pit geometry of Fig. 6.4. Profiles are plotted after 2.3 nm deposited. Notice that, for the case $f/D = 6 \times 10^{-4}$, the WL is thicker at the borders of the cell. (from Ref. [245])

According to our growth model (see eq. (6.1)), the key parameter which controls the time scale of the growth dynamics is the ratio f/D between the deposition flux and the surface mobility. This can be controlled both by acting on the material sources or by changing the temperature of the substrate, which has a direct effect on the mobility of adatoms. The two properties, deposition and diffusion, are strictly correlated, motivating the importance of their ratio rather than of their separate relative values. Indeed the diffusion length is determined both by the diffusion coefficient of the species involved in the transport, but also by the rate of the deposition, which determines how long an adatom can diffuse before it is buried by the subsequent deposited layer. The effect of changing the f/D ratio is illustrated in Fig. 6.6 by using the same pattern of Fig. 6.4 and depositing in 2.3 nm in total on the surface.

The lowest f/D ratio corresponds to the higher diffusion length for the deposited material, which can flow all over the surface. In particular, the tendency is to move toward the bottom of the pit because, as described in the previous section, it reduces the surface energy of the system. As a final result, a single island is grown inside the pit. By increasing the f/D three times ($f/D = 6 \times 10^{-4}$), the localized growth is still achieved, but with a higher accumulation of material on the surrounding WL, far from the pit region. This is evidenced by the small slope of the film profile that can be observed in the second panel of

Fig. 6.6. The non-flat slope is a suggestion that the diffusion of material toward the pit is partially limited by the increased deposition. This becomes more significant in the third case, at $f/D = 8 \times 10^{-4}$. The higher capability of the system to keep more material on the WL enables the formation of an island outside the pit, in the same time while the one inside the pit grows. By further increasing the f/D ratio at $f/D = 1.2 \times 10^{-3}$, a second island can be formed on the flat region of the substrate. In the final case analyzed here, a third island is observed outside the pit, leaving no flat regions for the film profile.

The extreme condition, with the highest f/D here considered, represents a case where the role of the pit in the growth of islands is nearly negligible. Indeed, the growth of the WL thickness above the critical value enables the growth of islands everywhere on the substrate. This behavior is similar to the one predicted by the ATG theory for the case of flat substrates. The only effect played by the pit is to introduce a non uniform elastic energy density in the growing film, due to the morphology of the pit. In particular the minimum of the chemical potential is localized in the center of the cell thanks to the additional relaxation of the pit, guaranteeing at least a lateral ordering of the island array. However this effect is not sufficient to drain all the deposited material to fill the pit. A detail that can be noticed is that the base of the islands is in good agreement with the ideal λ_{ATG}, while the island into the pit grows larger because it follows the sidewalls.

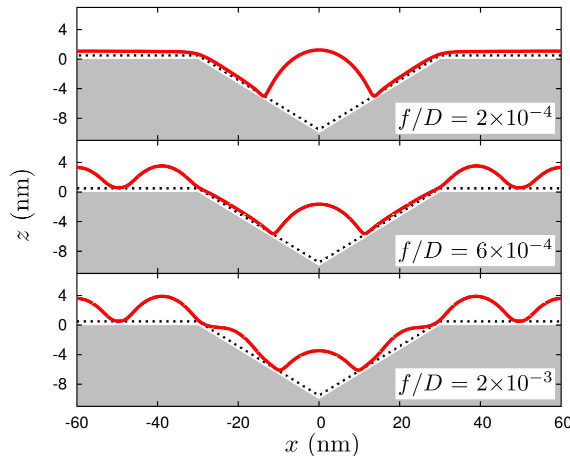

Figure 6.7: Role of the flux for larger pits obtained by doubling the base and the depth of those in Fig. 6.6. The initial condition (dotted lines) is a conformal film 0.5 nm thick. Profiles are plotted after 2.3 nm deposited. (from Ref. [245])

Since we have just shown that the diffusion length can play a major role in the growth dynamics, it is important to investigate the effect of the pit size on the growth of islands. For the first simulations, e.g. the one reported in Fig. 6.6, the pit width has been chosen to accommodate only one island. However, it not necessary to assume such a limitation in size to ensure a single-island growth. This is shown in the first panel of Fig. 6.7 where for a pit two times larger, i.e. $\approx 4\lambda_{\text{ATG}}$, a single island is grown. However this result may change if using a different f/D ratio to perform the growth. Indeed, while for the $f/D = 2 \times 10^{-4}$ ratio the dynamics drives the formation of a single island with a flat surrounding WL, for a ratio increased to $f/D = 6 \times 10^{-4}$ a perturbation of the film profile becomes unstable also outside the pit, leading to the growth of multiple islands. notice that, for the smaller pit

analyzed so far, this f/D ratio was sufficient to guarantee that only one island could develop. By a further increase of the flux up to a $f/D = 2 \times 10^{-3}$ ratio, the formation of multiple islands on the pit sidewalls is observed [262]. This phenomenon occurs because the upper part of the sidewalls if far enough from the bottom of the pit. Therefore those regions are able to accumulate material, growing above the WL critical thickness. Still, those islands on the sidewalls are smaller than the others, because their growth has to compete with the tendency to move material toward the larger and more efficiently relaxed island in the center of the pit. An interesting feature of the system, related with the pit size, is that the islands start to be apparent approximately with the same volume, more specifically with the same base width for the different pit configurations presented so far. As a consequence, if the pit aperture is too small, no island develops before the pit is completely filled. Then the growth is still observed above the pit region profiting of the relaxation promoted by the underlying inverted pyramid.

The trends analyzed in Fig. 6.6 and Fig. 6.7 give the possibility to identify the width of the capture zone determined by the island into the pit. This area tends to reduce for higher f/D ratios, due to the lower capability of adatoms to diffuse before being buried by the deposition process. If the distance between two adjacent pits exceeds this length, at least by the size of the minimum base required for the island growth, material can accumulate on the WL outside the pit, overcome the critical thickness and then form an island.

From the analysis performed so far, we can conclude that the surface profile strongly depends on the deposition flux. This suggests that the morphologies obtained during the growth are metastable states, that eventually differ from the equilibrium configuration. An important advantage of performing dynamic simulations is the possibility to follow the kinetic path, which is not accessible by a pure static analysis of the energetic of the system. Indeed the actual state achieved experimentally may be in an out-of equilibrium condition, far from the absolute minimum energy configuration. Nevertheless, it is always useful to investigate also the equilibrium condition toward which the system tends. This task is performed by the simulations in Fig. 6.8, where the annealing of the system is considered by suppressing the external source of material and keeping active only the surface diffusion. An important remark is that the equilibrium condition achieved by this approach does not necessarily match the absolute minimum energy. Indeed by simulations we can only consider the evolution pathways accessible via surface diffusion. In panel (a) we start to analyze the same profile obtained for $f/D = 1.2 \times 10^{-3}$ in Fig. 6.6. It is characterized by the growth of multiple islands both inside and outside the pit and it is imposed as the initial stage of the present simulation. The time sequence clearly shows that the material which composes the two islands on the flat WL is transferred toward the central island inside the pit. This process ends when the film outside becomes flat and no transfer is allowed any more due to the wetting potential, which opposes to a further thinning of the WL. Therefore we have verified that the islands outside the pit are just in a metastable state, which may appear during the growth process, but which does not correspond to the equilibrium configuration. This particular metastable state can be achieved not only through deposition, but also by an annealing simulation. The initial profile in Fig. 6.8(b,c)

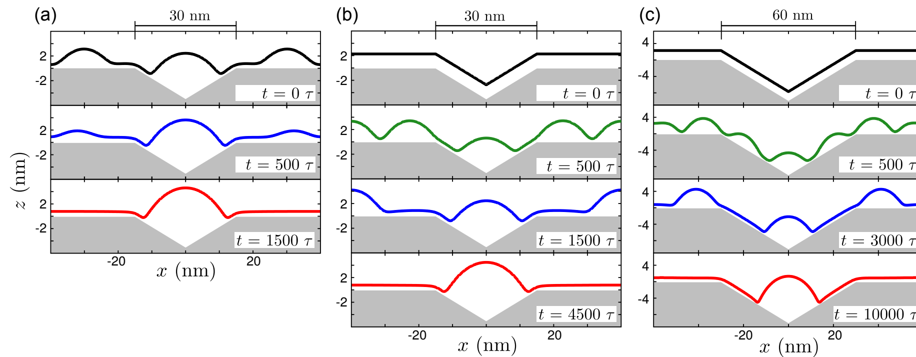

Figure 6.8: Annealing simulations from different initial geometries. (a) Evolution of the profile obtained for $f/D = 1.2 \times 10^{-3}$ in Fig. 6.6. (b,c) Evolution of a 2.3 nm thick conformal film (corresponding to the deposited material in panel (a)) for (b) a 30 nm wide pit as in Fig. 6.6 and (c) a 60 nm wide pit as in Fig. 6.7. Notice that the resulting islands in panels (a) and (b) are identical, while the one in panel (c) is larger due to the additional volume available in the cell. (from Ref. [245])

is set as a Ge conformal layer above the Si pit surface, for both 30 nm and 60 nm wide pits respectively. The thickness is set equal to $h_\mathrm{d} = 2.3$ nm to match the same deposited volume that is considered in panel (a), still guaranteeing to be above the critical thickness. In both those cases, an instability develops over the whole surface (shown at $t = 500\ \tau$). This induces the formation of islands both inside the pit, on the flat substrate outside and even on the pit sidewalls in correspondence with the largest pit width. This behavior resembles the one observed at high f/D in Figs. 6.6 and 6.7, and here we show that it is a temporary state. Indeed, by extending further the annealing time, the coarsening dynamics becomes relevant, exchanging material between islands in favor of the one inside the pit, which has the best strain relaxation among all. At longer evolution stage, just that island remains, providing the same equilibrium profile for all the three annealing simulations here considered, despite the different initial conditions and the intermediate evolution configurations.

6.3.3 Pattern geometry

The island growth into pits is driven both by capillarity and strain relaxation. This latter profits of the transfer of part of the strain into the substrate region. To achieve that, the key property is the compliance of the substrate, in terms of material elastic properties and geometry of the pits. The recent experimental techniques [29, 228, 231] allow one to finely control the pit shape, so that the role of different geometries can be considered experimentally. Here we want to investigate by simulations which is the impact of the substrate properties on the evolution of the growing film.

The evolution of islands growing into V-shaped pits with three different slopes is analyzed in Fig. 6.9. To focus only on the role of the pit itself, neglecting temporarily what happens outside on the flat substrate, we have set the simulation cell as wide as the pit. As already addressed in Section 6.3.1, at the onset of island growth, the typical base size $\sim \lambda_\mathrm{ATG}$ is observed for the three different cases here considered, suggesting a minor impact of the pit morphology on the initial island growth. However, it is immediately clear that the volume required to fill the pit, at least up to the level needed to have a base size $\sim \lambda_\mathrm{ATG}$, is not the

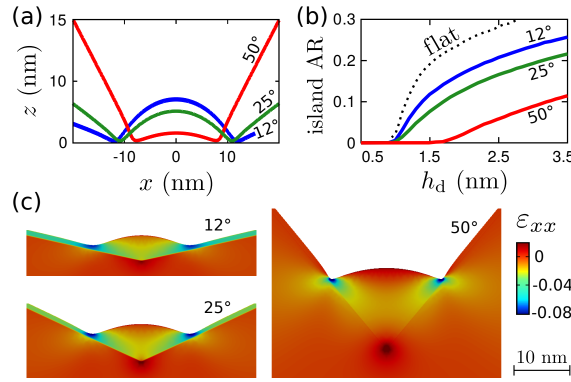

Figure 6.9: Simulations of island growth into pits of different sidewalls inclination: 12°, 25° and 50°. A low $f/D = 1 \times 10^{-4}$ is set. (a) Comparison of the profiles obtained at the same deposition time (vertical alignment is arbitrarily set). (b) Temporal evolution of the island AR. The curve for the case of an isolated island on a flat WL is shown by a dotted line (shifted at the onset of island growth for the shallowest pit). (c) Strain maps for the ε_{xx} component of islands at the same AR of 0.1. Only the central portion of the simulation cell (60 nm wide) is shown (in 1:1 ratio). (from Ref. [245])

same. Indeed, the stepper pit requires more material, and therefore a longer time, before the island starts to growth. As a consequence, a delay in the island formation occurs due to the different substrate morphology. This is made clear in the direct comparison of the surface profiles, at the same evolution time which also means same deposited volume, in Fig. 6.9(a), where the smallest island corresponds to the steepest sidewall configuration.

The delay in the island growth caused by the different sidewall inclination is highlight also in the analysis reported in Fig. 6.9(b), where the variation of the island AR is reported as a function of the material deposited. In addition to the three pit shapes, a reference case of the growth of a single island on a flat substrate is reported. Since the initial condition is clearly different between the pit and the flat substrate cases, the curve for the flat case has been shifted along the h_d to match the onset for the island formation of the shallowest pit, to allow for a closer comparison of the different behaviors. In this analysis we want to focus more on the equilibrium stages that are achieved by the islands during the deposition process. To this purpose, we have used a low $f/D = 1 \times 10^{-4}$ ratio, guaranteeing that each evolution stage is as close as possible to the equilibrium configuration for that particular deposited volume. As evident from the plot in panel (b), in addition to the effect on the onset of the instability, the sidewall inclination affects also the tendency to grow higher in AR. In particular, it is found that the steeper is the pit, the slower is the tendency to raise the AR. The reason for that is clarified by comparing the shape of an island of about the same AR, but different volume, for the three pits, as shown in Fig. 6.9(c). When the steepest pit is considered, the island appears more rounded. On the contrary, for the shallowest pit, the island is more cusp-like, similarly to what is expected for the growth on a flat substrate [263, 264]. This behavior reflects also the stronger tendency to fill the pit for steeper geometries. Indeed, the link between the WL and the island along the sidewalls requires an high curvature region, which tends to favor a more rounded shape which permits to reduce as much as possible this high curvature. In addition to that, as also discussed in Ref. [235], the steeper inclination of the sidewalls provides an enhanced relaxation within

the inverted-pyramid region. This produces a significant lowering of the strain at the surface of the islands, reducing the tendency driven by the chemical potential to increase the AR. The higher curvature at the link between the island and the sidewalls as well as the better strain relaxation make the AR of the steepest case grow slowly, as observed in Fig. 6.9(b).

When this trend is compared with experimental data for different pit shapes [29], it is found that the predictions of the model match the results for relatively shallow morphologies, in particular when the sidewalls angle is $\lesssim 30°$. Indeed a more complex variety of behaviors occurs when steeper geometries are considered. For example, in some cases it has even been shown that islands tend to form on the rims of the pit while no islanding if found in the bottom [29, 232, 235]. Additionally, experiments [231] have also shown that small pit obtained by focused ion beam could drive the ordering of islands only in between the pits. Even if recent theoretical studies [31, 265], based on approaches similar to the one exploited here, have been proposed to investigate this behavior, the study and reproduction of these peculiar trends is beyond the capabilities of the present model. Indeed, there are many additional physical features that should be considered for a complete picture of the system. One example is surface energy anisotropy, with particular attention to the strain-stabilized {105} facets [252]. These appears in the very initial stages of the growth and could promote the spontaneous growth of pyramids also on the flat region outside the pit. Moreover, the contribution of anisotropic elastic properties should be accounted, especially when considering steeper sidewalls as well as the intermixing dynamics, nucleation conditions [266] or even barriers [230], slowing down the transfer of material from the rims to the bottom of the pit. Further complexities may arise from a non uniform deposition when considering high AR morphologies, which could trigger the formation of islands on elevated regions [267].

From this short discussion, it is therefore clear how peculiar details of the system could lead to a variety of evolution dynamics, even for the case of a pit with a simple pyramidal shape. Additional complexity would be added to the system by changing the pattern geometry. For instance, in Ref. [57] it was shown that islands can grow on the top convex regions of large stripes and mesas, probably due to the existence of a peculiar local minimum of the chemical potential. Nonetheless, even in those experiments, it is confirmed that the concave foot of those structure represents the most favorable region to grow islands, particularly in conditions closer to equilibrium where the capillarity effect plays a major role in the distribution of material on the surface.

6.3.4 Material properties

In addition to the morphology of the pit, also the material properties may have an impact on the dynamics of capillarity and island growth. So far we have focused on the deposition of pure Ge on Si(001), but the present analysis could also be applied to other systems. The first variable that we investigate is the composition of the growing film. Indeed, the SiGe is an ideal alloy as Si and Ge are miscible for any composition, and therefore it is rather simple to tune the lattice mismatch between the film and the substrate just by changing the deposition ratio between Ge and Si. Moreover, particularly when depositing Ge on Si at

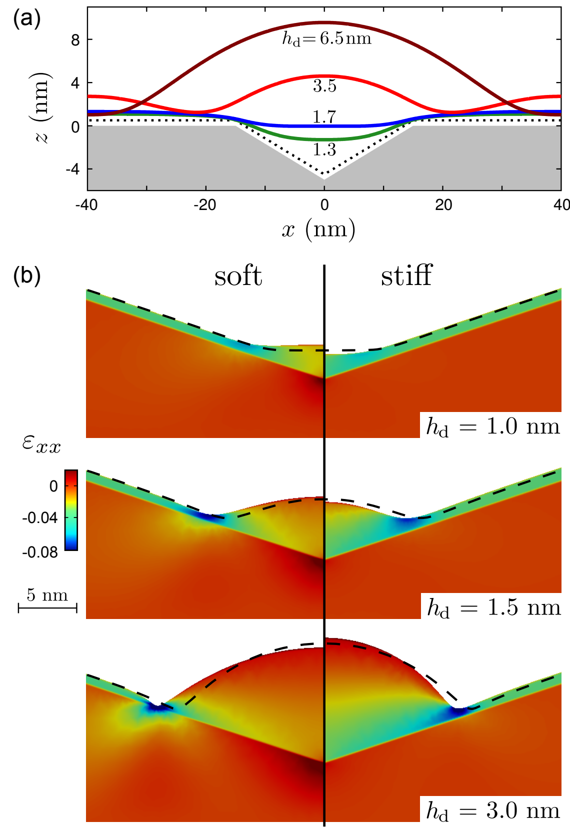

Figure 6.10: Effects of different elastic properties. (a) Evolution sequence for a simulation performed with the same pattern and growth conditions of Fig. 6.4 but for the deposition of a 50-50 SiGe alloy. (b) Comparison of island growth into the pit for (left) a soft substrate, with μ_s = 20 GPa, λ_s = 23 GPa, and (right) a stiff one, with μ_s = 236 GPa, λ_s = 277 GPa (values are obtained by an arbitrary scaling of the Si Young modulus). Misfit and surface properties are the same of Ge/Si. The dashed lines represent the corresponding surface profiles for the case with Si substrate. The strain component ε_{xx} is shown by the color map. Simulations are performed on a 60 nm wide pit, as large as the simulation cell. Only the central region is reported (in 1:1 ratio). $f/D = 1 \times 10^{-4}$. (from Ref. [245])

high temperature, the intermixing dynamics becomes unavoidable, and a significant fraction of Si is present in the growing layer [247], even if no Si is deposited during the growth. The actual intermixing dynamics is not part of the present treatment, and the implementation of a coupled model combining elasticity, surface diffusion and intermixing would require a big additional development effort [223–225]. Nevertheless, here we can study the evolution of an alloyed film on a pit-patterned substrate. This result can be achieved just by tuning the elastic and surface properties. In particular, for an ideal alloy as SiGe, the misfit ε_m^{fs} and surface energy γ_f can be determined by the linear Vegard's law, which interpolates between the bulk values for Si and Ge according to the local concentration. According to the analytical ATG theory, we expect that the major effect of this change in the simulation could be an increase of the island base, as $\lambda_{ATG} \sim \gamma/\varepsilon_m^2$. This means that a larger volume of strained SiGe is collected into the pit for capillarity reasons before an island start to grow. Even in this case, the pit still represents a preferential nucleation site, due to the better elastic relaxation. This is true also for a pit which is smaller than the base of the

island as in the case illustrated in Fig. 6.10(a). Since the deposited alloy has a composition of 50% Ge, its $\lambda_{\text{ATG}} \approx 60$ nm which is larger than the 30 nm wide pit. The first two stages report a pure capillarity dynamics, with no island growth despite the volume deposited is the same that in the pure Ge case of Fig. 6.4 allowed for an island formation. Once the pit is completely filled, the material continues to accumulate due to the deposition, but it preferentially flows on top of the pit, where still the strain relaxation is favored. When the critical thickness is overcome, islands are triggered all over the surface. The one in the center of the simulation cell is however more relaxed thanks to the inverted pyramid below, therefore it quickly makes the others disappear due to Ostwald ripening.

On the other hand, also the material of the substrate can have an impact on the growth process. Recent studies [251, 268] have identified that porous silicon or silicon membranes can act as compliant substrates, favoring the strain relaxation of the growing film. This behavior could become more effective for other heteroepitaxial systems where the difference in elastic properties between the film and the substrate is stronger. For the growth on planar substrate, a theory for the ATG instability has been developed in the literature [258]. In particular, it is known that stiffer substrates tend to stabilize the flat surface by increasing the critical thickness and, as a consequence, the wavelength λ_{ATG}.

The compliant role of the substrate can become more complex when a pit patterned substrate is considered. Thanks to our model which accounts for both the elastic properties of the substrate and of the deposited material, in Fig. 6.10(b) we propose the comparison of the growth of an island on two different pits, with the same morphology, but opposite compliant behavior. In particular, the one on the left is made softer than Si, while the one on the right is stiffer, and this is achieved just by changing the substrate elastic constants. In the initial stages, the pit filling dynamics is clearly enhanced in the case of the soft substrate. This is sufficient to grow an island into the pit bottom, which starts to grow following the sidewalls. On the contrary, in the stiff case the WL tends to grow thicker, allowing less material to flow toward the bottom of the pit. As a result, the island formation is delayed at later stages. This first observation is in good agreement with the prediction on a flat substrate [258]. However, the following evolution follows a different trend. Indeed, the island on the soft substrate has a more pronounced tendency to increase its base following the sidewalls. While the one on the stiff substrate tends to increase the AR, in favor of increasing the base width. This is particularly evident in the last stage reported in the figure, $h_{\text{d}} = 3.0$ nm, where the different height can be easily compared. This behavior can be motivated by the different strain relaxation, which can be recognized by the color map for the ε_{xx} component. The compliant substrate is able to accommodate a large part of the misfit strain of the growing film, lowering its elastic energy density. As a result, the island can achieve a good elastic relaxation without increasing much the AR. In this way, the surface curvature can remain relatively low thanks to the more rounded shape. On the opposite, the stiff substrate does not allow any strain relaxation against the sidewalls. Therefore, the elastic energy stored in the island can be relaxed just by further increase of the height, despite this requires to increase also the curvature of the profile.

6.3.5 3D simulation results

In the previous sections we have provided a detailed 2D analysis of the different contributions that may play a role in the ordering of heteroepitaxial islands on a pit patterned substrate. However, to provide a more realistic description of the evolution process, a full 3D model is needed. This enables to properly account for the three directions and improves the quantification of the energy of the system, both for the surface and elastic contribution, but has also an impact on the dynamics of material transfer. Moreover, the pit morphology is often not symmetric by rotation, for instance in the case of an inverted 3D pyramid. Therefore, in principle, the shape cannot be precisely described just by a 2D section. The arrangement of the pits on the substrate is another quantity that strictly requires a 3D description of the system. For instance, in a simple squared array of pits, as it is typically used in experiments, the flow of material from the WL toward the pit is expected to be different along the directions of the nearest neighbors with respect to the directions of the second-nearest neighbors, since the latter involve a larger flat regions between the pits.

One of the most useful advantages of using an implicit PF description is that the model can be straightforwardly applied to real 3D simulation just by extending the PF functions φ and c in the third dimension. The FEM toolbox AMDiS that we have exploited for the numerical implementation is developed to handle both 2 and 3 dimensions, so that no change was required on the numerical side. The main drawback of applying 3D simulations is related to the increased computational cost. To cope with that, a slightly lower resolution has been adopted by using larger interface widths for the free-surface (0.7 nm) and the film-substrate interface (0.4 nm). The pit morphology is an inverted-pyramid, which is representative of experiments and it is the closest to the V-shape used for 2D simulation, in order to permit a direct comparison with the previous simulation results. The AR of the pit has been fixed at 1:6, as in the most of the 2D cases considered so far.

The results of a 3D simulation are reported in Fig. 6.11(a,b) for the most respresentative stages of the island growth dynamics. The overall behavior seems to be fully consistent with the conclusions obtained by the 2D simulations, in particular the ones retrieved from Fig. 6.4. Initially the deposited material flows preferentially toward the bottom of the pit. There, when a sufficiently large volume is collected, an island starts growing. If we compare 2D and 3D simulations, we recognize that quantitatively they differ for the surface energy, particularly due to the different curvature value, and for the elastic strain relaxation, as the third direction is properly accounted for the calculation of the deformations within the island structure. Similarly to the 2D predictions, the localization of a single island inside the pit is basically related to its capture zone, which quantifies the volume of material that can be collected from the flat WL nearby. This depends on the f/D, as an high value allows for the accumulation of material outside, and when the critical thickness is reached, islanding can occur also there. At variance from the 2D description, this capture zone is expected to depend quadratically on the distance from the pit center. Therefore, as a result, the net material flowing into the 3D pit is larger if compared to a 2D infinite V-groove.

The 3D morphology of the pit, as well as the pit arrangement on the substrate, influences the actual island evolution. This is made clear by looking at the contour lines for selected

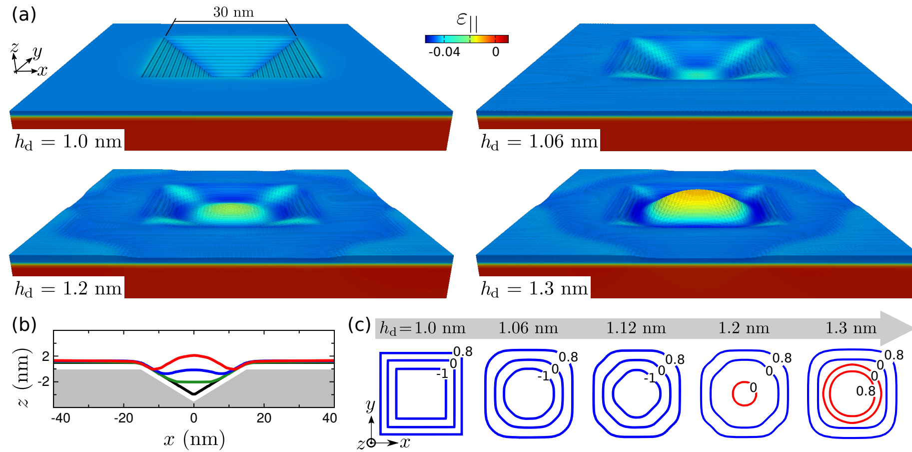

Figure 6.11: 3D simulation of island growth on a pit-patterned substrate. A 30 nm wide pit, with the shape of an inverted-pyramid of AR 1:6 and periodicity of 80 nm, is considered. (a) Perspective views of representative evolution stages, reporting the in-plane strain field $\varepsilon_{||} = (\varepsilon_{xx} + \varepsilon_{yy})/2$ by color map (a portion of the simulation cell is shown, stretched by a factor 1.5 along z). Profiles are clipped at $\varphi = 0.9$. (b) Cross-section profiles along the x direction through the pit center for the four stages shown in panel (a). (c) Elevation contour lines, in top view, for different stages of the evolution. Reported values correspond to the profile height z with respect to the substrate level on the flat regions. Blue and red colors are used for lines where z is decreasing or increasing respectively, moving toward the center. (from Ref. [245])

profile heights at different deposition stages which are reported in Fig. 6.11(c). Both the pit filling dynamics and the subsequent island growth reflect the squared symmetry of the pit. Indeed, the edges of the inverted-pyramid act as V-grooves. As predicted by the 2D model, these tend to collect material due to capillarity. Form the top-view, an apparent rotation of the pit morphology is then recognized. This phenomenon is enhanced by increasing the pit size or its AR, but it is limited to the initial stages dominated by capillarity. When the island starts to grow, it imposes its cusp-like geometry, mostly symmetric, independently on the initial squared symmetry of the pit. Indeed, the symmetric shape is expected to maximize the strain relaxation, minimizing at the same time the surface energy of the system when isotropic surface and elastic properties are considered.

6.4 Island stacking

The flexibility of the PF approach allows us to extend the modeling to other heteroepitaxial systems where the ordering of islands is considered of primary importance. In the literature, there are two main approaches to this purpose: pit patterning, as analyzed in the previous section, and island vertical ordering.

We focus here on the experimental results presented in Ref. [38], where it is observed that the stacking of SiGe nanodots for several layers follows a body-centered tetragonal stacking. The interesting aspect analyzed in that work, is that once dots are grown, the Si deposited on top as a capping layer is not perfectly flat. Indeed, by analyzing the surface via AFM, it was found that the free Si surface is composed by valleys in between the buried islands and bumps aligned vertical with the buried dots. Therefore, when the new SiGe

layer is deposited, we can infer that it resembles the growth on a Si substrate patterned with shallow pits. This could justify the preferential island positioning in the valleys of the Si surface [269], and not in vertical alignment with the buries dots. However, it can't be neglected that the elastic contribution would lead to the opposite behavior, since the aligned stacking would profit more of the elastic relaxation promoted by the buried SiGe layer [270, 271].

A better understanding of the competition between capillarity and localized elastic relaxation can be provided by simulation. The PF model can be straightforwardly extended to this system. The only variation with respect to the formulation used for the pit-patterned system is related to the definition of c. In this case, in the substrate region we have to account both for the Si layers and the SiGe grown ones, including the buried island profiles. Simulations are performed in 2D, to maximize the numerical resolution in order to have a precise quantification of the chemical potential contributions even in the case of small slope morphologies. The deposited material is made of SiGe alloy, at a 30% Ge content, which has a mismatch $\sim -1.3\%$ with respect to the pure Si, which composes the original flat substrate and the subsequent capping layers. The deposition of material, performed by CVD, is assumed to be isotropic and to impinge along the normal of each point of the surface. The $f/D = 1 \times 10^{-4}$ is sufficiently small to ensure that material can flow toward the local minimum of the chemical potential, suppressing the random island formation that would naturally occur at higher deposition rates.

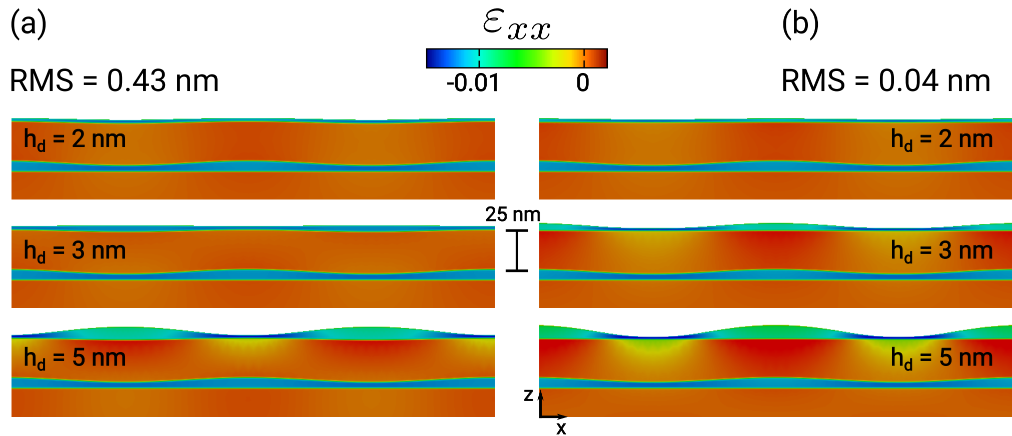

Figure 6.12: Phase-field simulations of island stacking. Growth of SiGe nanodots with 30% Ge content on a 25 nm thick Si cap layer, which is covering the first layer of buried SiGe nanodots. Three stages are shown for different amounts of deposited material (h_d). In panel (a), the surface root-mean-square roughness (RMS) of the Si capping layer is set to 0.43 nm. In the intermediate stage, the strain in the film is lower in the valley regions. This leads to an anti-aligned ordering of islands. In panel (b), the surface roughness of the Si capping is reduced by ten times. In the intermediate stage, the strain in the film is lower upon the buried islands. This finally leads to a vertically aligned stacking. The color map represents the in-plane strain component (ε_{xx}). (from Ref. [38])

The initial state of the simulation has to be chosen with particular attention, as small differences in the slope of the surface roughness could lead to different final behaviors. To save on simulation time, we focus on the alignment of a single SiGe layer on top of the

existing first layer of islands, already capped with Si. We reasonably assume that the growth of the following SiGe layers will follow the same dynamics of this first stacking module. The system is prepared by setting a cosine-like morphology for the buried layer. This is reasonable since the first growth occurs on a flat substrate, in the typical conditions of an ATG growth. The roughness (1 nm), periodicity (150 nm), and Ge composition (30%) are set to match the data measured experimentally for this system [38]. But the most important parameters are the one of the Si capping layer, in particular the average roughness (0.43 nm) and the thickness of Si (25 nm). This system is reported on the left side on Fig. 6.12, where it can be noticed that, during the deposition of the first SiGe layers, the free surface morphology matches the one of the Si capping layer. Indeed, at this stage the wetting energy term dominates the growth, favoring the thickening of the WL rather than a redistribution of material. When its effect becomes lower, thanks to the increased thickness of the WL, a capillarity dynamics is activated. The SiGe tends to flow toward the valleys present on the surface in order to make it flat, reducing the surface curvature. In these valley regions, similarly to what happens in a pit, the elastic relaxation of the film is enhanced thanks to the partial partitioning of the strain from the SiGe to the Si capping layer, through the sidewalls of these small pits. As a consequence, the chemical potential on the surface becomes lower in these regions. Since the surface energy contribution is constant on the surface as soon as the flat profile is reached, additional material accumulation is driven on top of the valleys, leading to the growth of an island. The final structure presents the opposite of a vertical alignment, which corresponds to the condition observed experimental. It is worth to notice that this alternated alignment occurs even if the initial strain distribution on the surface, induced by the buried layer, would favor a vertical stacking [270, 271]

The possibility to prevent a vertically aligned stacking seems related to the existence of the surface roughness. To confirm this hypothesis, we apply our model to try to assess the role of the surface roughness by reducing its magnitude. Indeed, the case where the slope of the valleys on the Si layer is increased would give the same evolution predicted for the pit patterned substrate, since it would mean that the impact of capillarity on the energy balance is increased. On the right column of Fig. 6.12 the surface roughness is decreased by one order of magnitude with respect to the case on the left. This means that the surface energy reduction provided by the filling of the valleys is lower than before, since the free surface profile is already closer to the flat case. In this case, the elastic relaxation on the top layer which is provided by the buried islands can play a major role. Indeed, at later deposition stages, a material accumulation outside of the valleys is observed, as driven by the lower elastic chemical potential on top of the buried dots. This promotes the formation of islands, which then collect most of the deposited material, preventing any island formation on the alternated positions. An additional result of the comparison between the two stacking systems, is that the vertically aligned islands result to be the most relaxed ones, thanks to the enhanced deformation induced by the buried ones. This is an additional indication that it is crucial to be able to follow the full growth pathway to asses the final alignment of the system, while a pure static analysis of the final elastic relaxation does not provide a complete picture of the system.

The surface roughness could in principle be reduced via two main ways. First, a longer anneling time for the Si capping layer, or alternativeley an higher deposition temperature, tends to flattend the top Si surface. Indeed, the elastic deformation induced by the buried SiGe islands would not favor the accumulation of tensile Si above, while capillarity is even more effective than for SiGe due to the higher surface energy density of Si. The alternative way to achieve the same result is to deposit Si for a longer time, producing a thicker capping layer. This elongates the time that the surface has to flatten the profile, producing a more flat capping layer as observed in experiments [38].

The role played by the surface roughness in determining a vertical anti-alignment was recently discussed also when considering the ordering of Ge quantum dots in an amorphous matrix [272]. Moreover, we have to point out that Liu et al. [273] reported that anti-alignment could arise also without surface roughness, due to a peculiar distribution of the strain field at the surface, as also drawn by Latini et al. for III/V systems [274]. While not ruling out the importance of such results under specific growth conditions, here we have demonstrated that, for the present system and growth parameters, a decisive role is played by surface roughness, while no anti-aligned ordering was found for a perfectly flat capping layer.

6.5 Conclusions

In this Chapter, we have exploited a phase-field approach to simulate the growth of islands on a pit-patterned substrate. Despite the system has been already widely studied in the literature by experiments, here we have provided a novel numerical approach that can couple an accurate calculation by finite element method of the strain relaxation to the surface diffusion dynamics, still solved exactly by finite element.

The model has enabled the study of the role of growth parameters on the ordered growth of island. In particular, it has been shown that in close-to-equilibrium conditions, when no kinetic incorporation effect plays a role, the localization of an island inside the pit is the most favorable configuration for the energetics of the system. This has been explained in terms of capillarity, which drives the filling of the pit, and by the enhanced strain relaxation of the island in the pit. The results predicted by the simulations qualitatively capture the main trends observed in the experiment. The model can then be proposed as a predictive tool for the heteroepitaxial growth of islands on patterned substrates, particularly for the possibility to perform real 3D simulations, that improve the accuracy of the numerical results both for the material transport dynamics and for the elastic relaxation calculation.

One of the main advantages of the phase-field approach is that the present model is not limited to pit morphologies. Indeed, thanks to the high flexibility provided by the implicit description of the film surface and of the substrate geometry, it is possible to handle any arbitrary pattern geometry. Our approach could be, for instance, applied to the study of other heteroepitaxial systems, based on curved substrates such as stripes or mesas [57], pillared structures [267], membranes [251]. As an example, here we have presented the application of island stacking, where the substrate is patterned in a sense that the growing

film is affected by the presence of buried layers underneath. In particularly, the model proved the capability of capturing both the localizing effect provide by strain and the capillarity driving force. The results of simulations have provided a theoretical explanation of the results observed experimentally in Ref. [38].

Finally, the flexibility of the finite element method can open future developments, including additional realistic effects such as elastic and surface anisotropy [127, 221] or intermixing [248, 275] within the same numerical approach.

Conclusions

In this Thesis, we have presented three theoretical approaches that, by considering a continuum description, can be exploited for the study of the epitaxial growth of semiconductors. The models have been applied to study four main experimental systems, with the aim of both reproducing the experimental observation and inferring about the main material properties which control the growth. This analysis has been particularly oriented toward the study of vertical nanostructures, which are of active scientific and technological interest for the development of new electronic and optoelectronic applications.

The growth of GaAs nanomembranes by selective area epitaxy has revealed a peculiar tendency of the system, in particular growth conditions, to grow vertically. A simple geometrical analysis of the experimental evidences, as acquired by SEM, revealed that the growth velocity of the top $(1\,1\,1)$B facet was more than one order of magnitude faster than the one for the lateral $\{1\,1\,0\}$. The standard thermodynamic approach for the faceted growth of nanostructures, driven by the minimization of the surface energy, has been applied with the aim of reproducing the growth of the nanomembranes. By this analysis we have demonstrated that standard thermodynamic arguments are not sufficient to justify such a peculiar vertical growth. Therefore, following the approach proposed by Cahn and Taylor [15], a kinetic growth model has been formulated. This has been implemented by the phase-field description of the system, which has allowed to reproduce the complex 3D morphologies observed in the experiments. The development of the simulation code has required a strong effort also on the numerical implementation, which has been performed with the fundamental collaboration of the group of Prof. Axel Voigt, director of the Institute of Scientific Computing at the Technische Universität Dresden. The model has been initially characterized with respect to the general faceting dynamics of semiconductor nanostructures. This has revealed an intermediate growth regime in between the well known Wulff's thermodynamic construction and the kinetic crystal shape. In particular, the novelty of the kinetic model here proposed is the capability of considering both material redistribution on the surface among the different crystal facets and material incorporation from the mobile adatom phase on the surface to the bulk crystal structure. Once the model has been fully characterized, it has been applied to simulate the selective area growth of GaAs 3D fins in homoepitaxial conditions [142].

As a first result, the model was able to capture the strong tendency of the crystal to grow vertically, along the $[1\,1\,1]$B direction, out of the $\langle 1\,1\,\overline{2} \rangle$-elongated oxide window. This proved that the kinetic dynamics of adatom incorporation is a fundamental element for the vertical growth of GaAs. Moreover, the model allowed us to characterize the growth in height of the

nanomembranes with respect to the length of the oxide windows, showing that a sudden change in the growth velocity is found when the (1 1 1)B growth front disappears from the crystal shape. The analysis of the system has then been extended to any oxide window orientation by performing dedicated experiments on a circular array. The phase-field model has been successfully applied also to the characterization of the complex fin morphologies that arise for the intermediate fin orientations, allowing for a better identification of the growing facets. Most importantly, the analysis of the morphological evolution of the GaAs crystal, in good agreement with the experiments, has allowed us to estimate the incorporation times of the {1 1 0} and {1 1 3} facets, which resulted to be respectively 10 and 2 times longer than the one for the (1 1 1)B fast growth front. This result represents a major advantage of the continuum approach used here, which has enabled the study of a property of the GaAs system which is still unaccessible by ab-initio atomistic calculations. Moreover, the simulation analysis has proven that a thermodynamic description based on the orientation-dependent surface energy densities is not sufficient to justify the vertical growth of GaAs nanomembranes.

Among all the vertical nanostructures, nanowires are the most studied nowadays in the literature. Since in this case the growth dynamics has been already widely characterized, particularly for the VLS growth techniques, in this Thesis we have focused on the characterization of the elastic properties of core/shell nanowires. These structures enable the heteroepitaxial growth on a substrate, which is represented by the core, which has remarkable compliance properties, similarly to the case of thin planar substrates. We have adopted a continuum elasticity approach, based on finite element method, which allows to simulate the whole 3D structure of the nanowire, despite the nearly one-dimensional geometry and the length which is of the order of microns. This theoretical activity has been performed in close comparison with the experimental results, achieved by the Advanced Nanomaterials & Devices group of Prof. Erik P.A.M. Bakkers, at the Technische Universiteit Eindhoven.

The first nanowire system that we have studied is the core/shell GaP/InGaP [175]. These nanowires are grown with the aim of obtaining a wurtzite InGaP alloy that can exhibit a direct band gap for applications as green light emitter. However, in the experiments, it was found that the nanowires tend to bend in random directions, a behavior which has to be avoided for the applications in ordered arrays. By finite element calculations, we have characterized the strain relaxation in the nanostructure, originated by the lattice parameter difference between the core and the shell. In particular, it has been shown as the composition and thickness asymmetries that are found in the shell by TEM and EDX analysis can be responsible of the bending. The curvature predicted by simulations proved to be in good agreement with the one measured from the TEM images. This allowed us to apply the finite element model as a predictive tool for the curvature of these nanowires, as a function of composition and shell thickness asymmetries.

The second core/shell system presented in this Thesis is made of Ge/GeSn nanowires [208]. Also in this case the interest is to grow a GeSn layer with a sufficiently high Sn content to achieve a direct band gap for the development of IR detectors. From the experimental

TEM analysis, it was found that the Sn composition in the shell is not uniform, but follows a gradient which increases with the shell thickness. By exploiting the finite element method, we have provided a detailed picture of the strain relaxation in the core/shell structure. This theoretical analysis is particularly useful in this system as the non-uniform composition and in general the low values of the residual strain make the experimental measurement of the lattice deformation extremely challenging. Moreover, the simulations has allowed to study the evolution of the strain at the surface for different shell thicknesses, mimicking the condition that occurs during the shell growth. This has identified a link between the strain relaxation and the Sn incorporation, showing a possible threshold for the strain at the surface which enables further Sn incorporation. Then, the role of the core in the strain relaxation mechanisms has been investigated, to provide a suggestion to experimentalist to design the optimal Ge core to maximize the Sn content in the GeSn alloy.

Finally, the phase-field model has been extended to the most complex case which includes both the surface diffusion dynamics and the continuum elasticity characterization. This is particularly challenging for the model implementation as the elastic contributions to the surface diffusion generally lead to unstable dynamics, which are complex to be handled numerically. This model has been applied to the study of the prototypical heteroepitaxial system where Ge islands are obtained by self-assembly on a Si substrate. In particular, we have focused on one the most relevant cases for applications which is the ordered growth on pit-patterned substrates [245]. The model here proposed allowed to properly account for the surface energy contributions driving the initial pit filling dynamics, due to capillarity. The coupling with the elastic calculations for the strain relaxation has correctly modeled the growth of an island inside the pit. The advantage provided by numerical simulations is the possibility to investigate the role of the growth parameters and of the geometry of the pattern in localizing the growth of a single island into the pit. The result of this analysis is that the optimal ordering is achieved in quasi-equilibrium conditions, which are favored for instance by a low deposition flux, or a high growth temperature, in agreement with the experimental observations already discussed in the literature. The flexibility of the phase-field approach has then allowed us to study the stacking of island, providing a theoretical explanation, related to the surface roughness of the intermediate Si capping layers, for the ordering observed experimentally [38].

The model which presents the most promising future perspective is the one devoted to the simulations of the vertical growth of GaAs fins. Indeed, this novel approach can be extended to other heteroepitaxial growths of vertical structures, a topic which is particularly active nowadays, by combining the kinetic description with the elasticity contributions to the growth. For instance, the growth of GaAs nanomembranes on Ge or Si substrates is of great interest for the integration of these nanostructures in the current Si technology, and the phase-field model here proposed could be useful to estimate the effect of strain in the morphological evolution of the nanostructures. The kinetic approach could be also extended to simulate the 3D growth of nano- and micro-pillars, correlating the crystal shape both with the incorporation time of the semiconductors involved in the growth process and with the growth parameters, such as the rate of material supply and the growth temperature. For

a more complete description of the growth of vertical structures in close-packed arrays, flux shielding effects should be included in the model [131]. Finally, for a more comprehensive description of the vertical growth processes, the modeling of a liquid phase should be developed, together with the description of the solid and vapor phases, to reproduce the VLS growth dynamics. An extensive application of the kinetic modeling would require an improvement of the ab-initio characterization of the incorporation times. This would finally enabled a complete multi-scale approach for the simulation of the growth of nanostructures, which would extend the actual continuum approaches which rely mainly on ab-initio results for the surface energy of the growing crystals.

List of publications

- **Albani, M.**, Bergamaschini, R., Montalenti, F. "Dynamics of pit filling in heteroepitaxy via phase-field simulations". Physical Review B 94, 75303 (2016).
- Gagliano, L; Belabbes, A.; **Albani, M.**; Assali, S. ; Verheijen, M. A.; Miglio, L.; Bechstedt, F.; Haverkort, J. E. M.; Bakkers, E. P. A. M. "Pseudodirect to Direct Compositional Crossover in Wurtzite GaP/$In_xGa_{1-x}P$ Core–Shell Nanowires". Nano Letters 16, 7930 (2016).
- Yamamoto, Y.; Zaumseil, P.; Capellini, G.; Andreas Schubert, M.; Hesse, A.; **Albani, M.**; Bergamaschini, R.; Montalenti, F.; Schroeder, T.; Tillack, B. "A self-ordered, body-centered tetragonal superlattice of SiGe nanodot growth by reduced pressure CVD". Nanotechnology 28, 485303 (2017).
- **Albani, M.**; Marzegalli, A.; Bergamaschini, R.; Mauceri, M.; Crippa, D.; La Via, F.; von Kanel, H.; Miglio, L. "Solving the critical thermal bowing in 3C-SiC/Si(1 1 1) by a tilting Si pillar architecture". Journal Applied Physics 123, 185703 (2018).
- Meduňa, M.; Isa, F.; Jung, A.; Marzegalli, A.; **Albani, M.**; Isella, G.; Zweiacker, K.; Miglio, L.; von Känel, H. "Lattice tilt and strain mapped by X-ray scanning nanodiffraction in compositionally graded SiGe/Si microcrystals". Journal of Applied Crystallography 51, 368 (2018).
- **Albani, M.**; Assali, S.; Verheijen, M. A.; Koelling, S.; Bergamaschini, R.; Pezzoli, F.; Bakkers, E. P. A. M.; Miglio, L. "Critical strain for Sn incorporation into spontaneously graded Ge/GeSn core/shell nanowires". Nanoscale 10, 7250 (2018).
- Gagliano, L.; **Albani, M.**; Verheijen, M. A.; Bakkers, E. P. A. M.; Miglio, L. "Twofold origin of strain-induced bending in core–shell nanowires: the GaP/InGaP case". Nanotechnology 29, 315703 (2018).
- **Albani, M.**; Ghisalberti, L.; Bergamaschini, R.; Friedl, M.; Salvalaglio, M.; Voigt, A.; Montalenti, F.; Tütüncuoglu, G.; Fontcuberta i Morral, A.; Miglio, L. "Growth kinetics and morphological analysis of homoepitaxial GaAs fins by theory and experiment". Physical Review Materials 2, 093404 (2018).
- **Albani, M.**; Bergamaschini, R; Salvalaglio, M; Voigt, A; Miglio, L; Montalenti, F "Competition between kinetics and thermodynamics during the growth of faceted crystal by phase field modeling". Physica Status Solidi B, 1800518 (2019).

Acronyms

- ECS equilibrium crystal shape
- KCS kinetic crystal shape
- PF phase-field
- SEM scanning electron microscope
- SAE selective area epitaxy
- NW nanowire
- NM nanomembrane
- LED light-emitting diodes
- TEM transmission electron microscopy
- EDX energy-dispersive X-ray diffraction
- VLS vapor-liquid-solid
- ATG Asaro-Tiller-Grinfeld
- MBE molecular beam epitaxy
- CVD chemical vapor deposition
- PECVD plasma enhanced chemical vapor deposition
- FEM finite element method
- ML monolayer
- RMS root mean square
- FIB focused ion beam
- ED electron diffraction
- HAADF high-angle annular dark-field scanning transmission electron microscopy
- WZ wurtzite
- SK Stranski-Krastanov
- AR aspect ratio
- WL wetting layer

Acknowledgements

First of all, I would like to thank my supervisor, Prof. Leo Miglio, who guided my Ph.D. activity in his group and gave me the opportunity to work on different and active research topics, in collaboration with other European groups.

Special thanks also to Prof. Francesco Montalenti, who guided me during the first year, continuing the work that I had started during my master thesis under his supervision. Moreover, I thank him also for the continuous and profitable discussions about models implementation and physical interpretation, shedding a light on apparently pure-mathematical concepts.

I am grateful to Prof. Axel Voigt for hosting me for five months in Dresden. He introduced me to the development of models for the kinetic growth, providing free access to HPC resources and teaching me how to profitably use them. This work was made possible also by the great help by Marco Salvalaglio, who supported me day by day at work and that introduced me to the Dresden life.

I thank also Prof. Erik P.A.M. Bakkers, for hosting me for one month in Eindhoven, offering the possibility to work in an experimental group. This both allowed me to learn a different way of organizing the work and offered me the possibility to apply some of my models to experimental cases. This was made possible also by the collaboration with Luca Gagliano and Simone Assali, who led the works on InGaP and GeSn nanowires. I am particularly grateful for Marcel A. Verheijen, who provided us a lot of TEM analysis, and gave a strong contribution to the interpretation of the experimental evidences.

The other extensive comparison with experiments was made possible thanks to the group of Prof. Anna Fontcuberta i Morral, who allowed us to study the details of the nanomembrane growth, performing dedicated experiments which enabled a better understanding of the growth dynamics. A very helpful support on this topic, and more in general on the III-V systems, was given by Prof. Stefano Sanguinetti and by Sergio Bietti, introducing us to the modeling of other systems than Si/Ge ones.

Infinite thanks to Roberto, who supported me from the bachelor thesis to nowadays, both in code developing, article writing, figure editing and discussing about all the scientific work that I have done. Thanks to Anna, who introduced me to elastic FEM calculations, opening the possibility to work on nanowires structures. I thank also all the other people that are part of the group, Fabrizio, Emilio, Andrey and Luca, for sharing the life in the department.

At the end of this long study season of my life, I want to thank my family who made this possible. First my parents, Luigi and Gemma, for the support for the studies and for

the abroad periods. Then to my brother and sisters Maria, Silvia and Flavio, for sharing the difficulties under the same roof. A special thanks to my class mates and friends, who where always interested in the progress of my studies, often asking me what sort of islands or fins I was simulating.

But the last and most important thanks are for Giulia, who is sharing ordinary and special moments of my life.

Marco

Bibliography

1. Moore, G. “Cramming More Components Onto Integrated Circuits”. *Proc. IEEE* **86,** p. 82 (1998).
2. Collaert, N. *et al.* “Ultimate nano-electronics: New materials and device concepts for scaling nano-electronics beyond the Si roadmap”. *Microelectron. Eng.* **132,** p. 218 (2015).
3. Fuechsle, M., Miwa, J. A., Mahapatra, S., Ryu, H., Lee, S., Warschkow, O., Hollenberg, L. C., Klimeck, G. & Simmons, M. Y. “A single-atom transistor”. *Nat. Nanotechnol.* **7,** p. 242 (2012).
4. Loo, R. *et al.* “(Invited) Processing Technologies for Advanced Ge Devices”. *ECS Trans.* **75,** p. 491 (2016).
5. Xuejue Huang *et al.* “Sub-50 nm P-channel FinFET”. *IEEE Trans. Electron Devices* **48,** p. 880 (2001).
6. Singh, N *et al.* “High-performance fully depleted silicon nanowire (diameter < 5 nm) gate-all-around CMOS devices”. *IEEE Electron Device Lett.* **27,** p. 383 (2006).
7. Yang, P., Yan, R. & Fardy, M. “Semiconductor Nanowire: What’s Next?” *Nano Lett.* **10,** p. 1529 (2010).
8. Li, D., Wu, Y., Kim, P., Shi, L., Yang, P. & Majumdar, A. “Thermal conductivity of individual silicon nanowires”. *Appl. Phys. Lett.* **83,** p. 2934 (2003).
9. Yip, S. “Synergistic science”. *Nat. Mater.* **2,** p. 3 (2003).
10. Li, B., Lowengrub, J., Rätz, A. & Voigt, A. “Review article: Geometric evolution laws for thin crystalline films: modeling and numerics”. *Commun. Comput. Phys.* **6,** p. 433 (2009).
11. Fried, E. & Gurtin, M. E. “A unified treatment of evolving interfaces accounting for small deformations and atomic transport with emphasis on grain-boundaries and epitaxy”. *Adv. Appl. Mech.* **40,** p. 1 (2004).
12. Cahn, J. W. & Carter, W. C. “Crystal Shapes and Phase Equilibria: A Common Mathematical Basis”. *Metall. Mater. Trans. A* **27A,** p. 1431 (1996).
13. Cahn, J. W. & Hoffman, D. W. “A vector thermodynamics for anisotropic surfaces - II. curved and faceted surfaces”. *Acta Metall.* **22** (1974).
14. Wulff, G. “XXV. Zur Frage der Geschwindigkeit des Wachsthums und der Auflösung der Krystallflächen”. *Zeitschrift fur Kryst. und Mineral.* **34,** p. 449 (1901).

15. Cahn, J. W. & Taylor, J. E. "Overview no. 113 surface motion by surface diffusion". *Acta Metall. Mater.* **42,** p. 1045 (1994).
16. Aagesen, L. K., Coltrin, M. E., Han, J. & Thornton, K. "Phase-field simulations of GaN growth by selective area epitaxy from complex mask geometries". *J. Appl. Phys.* **117** (2015).
17. Vey, S. & Voigt, A. "AMDiS: adaptive multidimensional simulations". *Comput. Vis. Sci.* **10,** p. 57 (2007).
18. Witkowski, T., Ling, S., Praetorius, S. & Voigt, A. "Software concepts and numerical algorithms for a scalable adaptive parallel finite element method". *Adv. Comput. Math.* **41,** p. 1145 (2015).
19. Garnett, E. & Yang, P. "Light Trapping in Silicon Nanowire Solar Cells". *Nano Lett.* **10,** p. 1082 (2010).
20. Algra, R. E., Hocevar, M., Verheijen, M. a., Zardo, I., Immink, G. G. W., van Enckevort, W. J. P., Abstreiter, G., Kouwenhoven, L. P., Vlieg, E. & Bakkers, E. P. A. M. "Crystal Structure Transfer in Core/Shell Nanowires". *Nano Lett.* **11,** p. 1690 (2011).
21. Fontcuberta i Morral, A. "Gold-Free GaAs Nanowire Synthesis and Optical Properties". *IEEE J. Sel. Top. Quantum Electron.* **17,** p. 819 (2011).
22. Boxberg, F., Søndergaard, N. & Xu, H. Q. "Elastic and Piezoelectric Properties of Zincblende and Wurtzite Crystalline Nanowire Heterostructures". *Adv. Mater.* **24,** p. 4692 (2012).
23. Stangl, J, Holý, V. & Bauer, G. "Structural properties of self-organized semiconductor nanostructures". *Rev. Mod. Phys.* **76,** p. 725 (2004).
24. Berbezier, I & Ronda, A. "Surface Science Reports SiGe nanostructures". *Surf. Sci. Rep.* **64,** p. 47 (2009).
25. Asaro, R. J. & Tiller, W. A. "Interface morphology development during stress corrosion cracking: Part I. Via surface diffusion". *Metall. Trans.* **3,** p. 1789 (1972).
26. Grinfeld, M. A. "The stress driven instability in elastic crystals: Mathematical models and physical manifestations". *J. Nonlinear Sci.* **3,** p. 35 (1993).
27. Srolovitz, D. "On the stability of surfaces of stressed solids". *Acta Metall.* **37,** p. 621 (1989).
28. Brehm, M. & Grydlik, M. "Site-controlled and advanced epitaxial Ge/Si quantum dots: fabrication, properties, and applications". *Nanotechnology* **28,** p. 392001 (2017).
29. Grydlik, M., Langer, G., Fromherz, T., Schäffler, F. & Brehm, M. "Recipes for the fabrication of strictly ordered Ge islands on pit-patterned Si(001) substrates." *Nanotechnology* **24,** p. 105601 (2013).
30. Amatya, J. M. & Floro, J. A. "Site-selection of Si 1-x Ge x quantum dots on patterned Si(001) substrates". *Appl. Phys. Lett.* **109,** p. 193112 (2016).
31. Aqua, J.-N. & Xu, X. "Directed self-organization of quantum dots". *Phys. Rev. E* **90,** p. 030402 (2014).

32. Rätz, A., Ribalta, A. & Voigt, A. “Surface evolution of elastically stressed films under deposition by a diffuse interface model”. *J. Comput. Phys.* **214,** p. 187 (2006).

33. Grabow, M. H. & Gilmer, G. H. “Thin film growth modes, wetting and cluster nucleation”. *Surf. Sci.* **194,** p. 333 (1988).

34. Ayers, J. E. *Heteroepitaxy of Semiconductors: Theory, Growth, and Characterization* (CRC Press).

35. Weeks, J. D. & Gilmer, G. H. in *Adv. Chem. Phys.* p. 157 (2007).

36. Bauer, E. & Poppa, H. “Recent advances in epitaxy”. *Thin Solid Films* **12,** p. 167 (1972).

37. Ratsch, C. & Venables, J. A. “Nucleation theory and the early stages of thin film growth”. *J. Vac. Sci. Technol. A Vacuum, Surfaces, Film.* **21,** S96 (2003).

38. Yamamoto, Y., Zaumseil, P., Capellini, G., Andreas Schubert, M., Hesse, A., Albani, M., Bergamaschini, R., Montalenti, F., Schroeder, T. & Tillack, B. “A self-ordered, body-centered tetragonal superlattice of SiGe nanodot growth by reduced pressure CVD”. *Nanotechnology* **28,** p. 485303 (2017).

39. Rosenblad, C., Deller, H. R., Dommann, A., Meyer, T., Schroeter, P. & von Känel, H. “Silicon epitaxy by low-energy plasma enhanced chemical vapor deposition”. *J. Vac. Sci. Technol. A Vacuum, Surfaces, Film.* **16,** p. 2785 (1998).

40. Zehe, A. *M. A. Herman, H. Sitter. Molecular beam epitaxy—fundamentals and current status. Springer-Verlag Berlin-Heidelberg-New York-London-Paris-Tokyo 1989, 382 pages, 249 figures, hard cover, DM 128. –, ISBN 3-540-19075-9.* **11,** p. 1186 (1989).

41. Stekolnikov, a. A., Furthmüller, J. & Bechstedt, F. “Absolute surface energies of group-IV semiconductors: Dependence on orientation and reconstruction”. *Phys. Rev. B - Condens. Matter Mater. Phys.* **65,** p. 1 (2002).

42. Beck, M. J., van de Walle, A & Asta, M. “Surface energetics and structure of the Ge wetting layer on Si(100)”. *Phys. Rev. B* **70,** p. 205337 (2004).

43. Müller, P. & Kern, R. “The physical origin of the two-dimensional towards three-dimensional coherent epitaxial Stranski-Krastanov transition”. *Appl. Surf. Sci.* **102,** p. 6 (1996).

44. Spencer, B. J., Voorhees, P. W. & Tersoff, J. “Morphological instability theory for strained alloy film growth: The effect of compositional stresses and species-dependent surface mobilities on ripple formation during epitaxial film deposition”. *Phys. Rev. B* **64,** p. 235318 (2001).

45. Ozkan, C. S., Nix, W. D. & Gao, H. “Strain relaxation and defect formation in heteroepitaxial Si1-xGex films via surface roughening induced by controlled annealing experiments”. *Appl. Phys. Lett.* **70,** p. 2247 (1997).

46. Nötzel, R. & Ploog, K. H. “Direct synthesis of semiconductor quantum-wire and quantum-dot structures”. *Adv. Mater.* **5,** p. 22 (1993).

47. Wang, K. L., Cha, D., Liu, J. & Chen, C. “Ge/Si self-assembled quantum dots and their optoelectronic device applications”. *Proc. IEEE* **95,** p. 1866 (2007).

48. Basso Basset, F., Bietti, S., Reindl, M., Esposito, L., Fedorov, A., Huber, D., Rastelli, A., Bonera, E., Trotta, R. & Sanguinetti, S. “High-Yield Fabrication of Entangled Photon Emitters for Hybrid Quantum Networking Using High-Temperature Droplet Epitaxy”. *Nano Lett.* **18,** p. 505 (2018).

49. Linder, K. K., Phillips, J., Qasaimeh, O., Liu, X. F., Krishna, S., Bhattacharya, P. & Jiang, J. C. “Self-organized In[0.4]Ga[0.6]As quantum-dot lasers grown on Si substrates”. *Appl. Phys. Lett.* **74,** p. 1355 (1999).

50. Kiravittaya, S., Rastelli, A. & Schmidt, O. G. “Advanced quantum dot configurations”. *Reports Prog. Phys.* **72,** p. 046502 (2009).

51. Schmidt, O. G. & Eberl, K. “Self-assembled Ge/Si dots for faster field-effect transistors”. *IEEE Trans. Electron. devices* **48,** p. 1175 (2001).

52. Nassiopoulou, A. G., Olzierski, A, Tsoi, E, Berbezier, I & Karmous, A. “Ge quantum dot memory structure with laterally ordered highly dense arrays of Ge dots”. *J. Nanosci. Nanotechnol.* **7,** p. 316 (2007).

53. Wang, S., Zhang, N., Chen, P., Wang, L., Yang, X., Jiang, Z. & Zhong, Z. “Toward precise site-controlling of self-assembled Ge quantum dots on Si microdisks”. *Nanotechnology* **29,** p. 345606 (2018).

54. Michler, P, Kiraz, A, Becher, C & Schoenfeld, W. V. “A Quantum Dot Single-Photon Turnstile Device”. *Science (80-.).* **290** (1999).

55. Sandorfy, C *et al.* “Electrically Driven Single-Photon Source”. **295** (2002).

56. Zhong, Z. & Bauer, G. “Site-controlled and size-homogeneous Ge islands on prepatterned Si (001) substrates”. *Appl. Phys. Lett.* **84,** p. 1922 (2004).

57. Yang, B., Liu, F. & Lagally, M. G. “Local Strain-Mediated Chemical Potential Control of Quantum Dot Self-Organization in Heteroepitaxy”. *Phys. Rev. Lett.* **92,** p. 025502 (2004).

58. Dasgupta, N. P., Sun, J., Liu, C., Brittman, S., Andrews, S. C., Lim, J., Gao, H., Yan, R. & Yang, P. “25th Anniversary Article: Semiconductor Nanowires - Synthesis, Characterization, and Applications”. *Adv. Mater.* **26,** p. 2137 (2014).

59. Johansson, J. & Dick, K. A. “Recent advances in semiconductor nanowire heterostructures”. *CrystEngComm* **13,** p. 7175 (2011).

60. Wagner, R. S. & Ellis, W. C. “VAPOR-LIQUID-SOLID MECHANISM OF SINGLE CRYSTAL GROWTH”. *Appl. Phys. Lett.* **4,** p. 89 (1964).

61. Yazawa, M., Koguchi, M., Muto, A., Ozawa, M. & Hiruma, K. “Effect of one monolayer of surface gold atoms on the epitaxial growth of InAs nanowhiskers”. *Appl. Phys. Lett.* **61,** p. 2051 (1992).

62. Yazawa, M., Koguchi, M., Muto, A. & Hiruma, K. “Semiconductor nanowhiskers”. *Adv. Mater.* **5,** p. 577 (1993).

63. Xia, Y., Yang, P., Sun, Y., Wu, Y., Mayers, B., Gates, B., Yin, Y., Kim, F. & Yan, H. "One-Dimensional Nanostructures: Synthesis, Characterization, and Applications". *Adv. Mater.* **15,** p. 353 (2003).

64. Huang, M. H. "Room-Temperature Ultraviolet Nanowire Nanolasers". *Science (80-.).* **292,** p. 1897 (2001).

65. Duan, X., Huang, Y., Agarwal, R. & Lieber, C. M. "Single-nanowire electrically driven lasers". *Nature* **421,** p. 241 (2003).

66. Kim, W., Ng, J. K., Kunitake, M. E., Conklin, B. R. & Yang, P. "Interfacing Silicon Nanowires with Mammalian Cells". *J. Am. Chem. Soc.* **129,** p. 7228 (2007).

67. Hällström, W., Mårtensson, T., Prinz, C., Gustavsson, P., Montelius, L., Samuelson, L. & Kanje, M. "Gallium Phosphide Nanowires as a Substrate for Cultured Neurons". *Nano Lett.* **7,** p. 2960 (2007).

68. Shalek, A. K. *et al.* "Vertical silicon nanowires as a universal platform for delivering biomolecules into living cells". *Proc. Natl. Acad. Sci.* **107,** p. 1870 (2010).

69. Patolsky, F. "Detection, Stimulation, and Inhibition of Neuronal Signals with High-Density Nanowire Transistor Arrays". *Science (80-.).* **313,** p. 1100 (2006).

70. Ponce, F. A. & Bour, D. P. "Nitride-based semiconductors for blue and green light-emitting devices". *Nature* **386,** p. 351 (1997).

71. Minot, E. D., Kelkensberg, F., van Kouwen, M., van Dam, J. A., Kouwenhoven, L. P., Zwiller, V., Borgström, M. T., Wunnicke, O., Verheijen, M. A. & Bakkers, E. P. A. M. "Single Quantum Dot Nanowire LEDs". *Nano Lett.* **7,** p. 367 (2007).

72. Qian, F., Li, Y., Gradečak, S., Wang, D., Barrelet, C. J. & Lieber, C. M. "Gallium Nitride-Based Nanowire Radial Heterostructures for Nanophotonics". *Nano Lett.* **4,** p. 1975 (2004).

73. Huang, Y., Duan, X. & Lieber, C. M. "Nanowires for Integrated Multicolor Nanophotonics". *Small* **1,** p. 142 (2004).

74. Chan, C. K., Peng, H., Liu, G., McIlwrath, K., Zhang, X. F., Huggins, R. A. & Cui, Y. "High-performance lithium battery anodes using silicon nanowires". *Nat. Nanotechnol.* **3,** p. 31 (2008).

75. Kim, B. J., Tersoff, J., Wen, C.-Y., Reuter, M. C., Stach, E. A. & Ross, F. M. "Determination of Size Effects during the Phase Transition of a Nanoscale Au-Si Eutectic". *Phys. Rev. Lett.* **103,** p. 155701 (2009).

76. Jacobsson, D., Panciera, F., Tersoff, J., Reuter, M. C., Lehmann, S., Hofmann, S., Dick, K. A. & Ross, F. M. "Interface dynamics and crystal phase switching in GaAs nanowires". *Nature* **531,** p. 317 (2016).

77. Shin, N. & Filler, M. A. "Controlling Silicon Nanowire Growth Direction via Surface Chemistry". *Nano Lett.* **12,** p. 2865 (2012).

78. Kuykendall, T., Pauzauskie, P. J., Zhang, Y., Goldberger, J., Sirbuly, D., Denlinger, J. & Yang, P. "Crystallographic alignment of high-density gallium nitride nanowire arrays". *Nat. Mater.* **3,** p. 524 (2004).

79. Assali, S., Gagliano, L., Oliveira, D. S., Verheijen, M. A., Plissard, S. R., Feiner, L. F. & Bakkers, E. P. A. M. "Exploring Crystal Phase Switching in GaP Nanowires". *Nano Lett.* **15,** p. 8062 (2015).

80. Glas, F., Harmand, J. C. & Patriarche, G. "Why does wurtzite form in nanowires of III-V zinc blende semiconductors?" *Phys. Rev. Lett.* **99,** p. 3 (2007).

81. Allen, J. E. *et al.* "High-resolution detection of Au catalyst atoms in Si nanowires". *Nat. Nanotechnol.* **3,** p. 168 (2008).

82. Dayeh, S. A., Yu, E. T. & Wang, D. "III-V Nanowire Growth Mechanism: V/III Ratio and Temperature Effects". *Nano Lett.* **7,** p. 2486 (2007).

83. Gagliano, L., Belabbes, A., Albani, M., Assali, S., Verheijen, M. A., Miglio, L., Bechstedt, F., Haverkort, J. E. M. & Bakkers, E. P. A. M. "Pseudodirect to Direct Compositional Crossover in Wurtzite GaP/In x Ga 1– x P Core–Shell Nanowires". *Nano Lett.* **16,** p. 7930 (2016).

84. Krogstrup, P., Jørgensen, H. I., Heiss, M., Demichel, O., Holm, J. V., Aagesen, M., Nygard, J. & Fontcuberta i Morral, A. "Single-nanowire solar cells beyond the Shockley–Queisser limit". *Nat. Photonics* **7,** p. 306 (2013).

85. Hauge, H. I. T., Conesa-Boj, S., Verheijen, M. A., Koelling, S. & Bakkers, E. P. A. M. "Single-Crystalline Hexagonal Silicon–Germanium". *Nano Lett.* **17,** p. 85 (2017).

86. Heinecke, H., Brauers, A., Grafahrend, F., Plass, C., Pütz, N., Werner, K., Weyers, M., Lüth, H. & Balk, P. "Selective growth of GaAs in the MOMBE and MOCVD systems". *J. Cryst. Growth* **77,** p. 303 (1986).

87. Tomioka, K., Ikejiri, K., Tanaka, T., Motohisa, J., Hara, S., Hiruma, K. & Fukui, T. "Selective-area growth of III-V nanowires and their applications". *J. Mater. Res.* **26,** p. 2127 (2011).

88. Ikejiri, K., Noborisaka, J., Hara, S., Motohisa, J. & Fukui, T. "Mechanism of catalyst-free growth of GaAs nanowires by selective area MOVPE". *J. Cryst. Growth* **298,** p. 616 (2007).

89. Chatillon, C. & Chatain, D. "Congruent vaporization of GaAs(s) and stability of Ga(l) droplets at the GaAs(s) surface". *J. Cryst. Growth* **151,** p. 91 (1995).

90. Aagesen, L. K., Lee, L. K., Ku, P.-C. & Thornton, K. "Phase-field simulations of GaN/InGaN quantum dot growth by selective area epitaxy". *J. Cryst. Growth* **361,** p. 57 (2012).

91. Greenaway, A. L., Sharps, M. C., Boucher, J. W., Strange, L. E., Kast, M. G., Aloni, S. & Boettcher, S. W. "Selective Area Epitaxy of GaAs Microstructures by Close-Spaced Vapor Transport for Solar Energy Conversion Applications". *ACS Energy Lett.* **1,** p. 402 (2016).

92. Niu, G. *et al.* “Dislocation-free Ge Nano-crystals via Pattern Independent Selective Ge Heteroepitaxy on Si Nano-Tip Wafers”. *Sci. Rep.* **6,** p. 22709 (2016).

93. Merckling, C. *et al.* “Selective area growth of InP in shallow trench isolation on large scale Si(001) wafer using defect confinement technique”. *J. Appl. Phys.* **114,** p. 033708 (2013).

94. Wang, G. *et al.* “Integration of highly-strained SiGe materials in 14nm and beyond nodes FinFET technology”. *Solid. State. Electron.* **103,** p. 222 (2015).

95. Merckling, C. *et al.* “Heteroepitaxy of InP on Si(001) by selective-area metal organic vapor-phase epitaxy in sub-50 nm width trenches: The role of the nucleation layer and the recess engineering”. *J. Appl. Phys.* **115,** p. 023710 (2014).

96. Tian, B., Wang, Z., Pantouvaki, M., Absil, P., Van Campenhout, J., Merckling, C. & Van Thourhout, D. “Room Temperature O-band DFB Laser Array Directly Grown on (001) Silicon”. *Nano Lett.* **17,** p. 559 (2017).

97. Wang, Z., Tian, B., Pantouvaki, M., Guo, W., Absil, P., Van Campenhout, J., Merckling, C. & Van Thourhout, D. “Room-temperature InP distributed feedback laser array directly grown on silicon”. *Nat. Photonics* **9,** p. 837 (2015).

98. Tutuncuoglu, G., De la Mata, M, Deiana, D, Potts, H, Matteini, F, Arbiol, J & Fontcuberta i Morral, A. “Towards defect-free 1-D GaAs/AlGaAs heterostructures based on GaAs nanomembranes”. *Nanoscale* **7,** p. 19453 (2015).

99. Arab, S., Chi, C. Y., Shi, T., Wang, Y., Dapkus, D. P., Jackson, H. E., Smith, L. M. & Cronin, S. B. “Effects of surface passivation on twin-free GaAs nanosheets”. *ACS Nano* **9,** p. 1336 (2015).

100. Huang, C. *et al.* “Template-Assisted Scalable Nanowire Networks”. *Nano Lett.* **18,** p. 2666 (2018).

101. Hartmann, J. *et al.* “High Aspect Ratio GaN Fin Microstructures with Nonpolar Sidewalls by Continuous Mode Metalorganic Vapor Phase Epitaxy”. *Cryst. Growth Des.* **16,** p. 1458 (2016).

102. Yeh, T.-W. W., Lin, Y.-T. T., Ahn, B., Stewart, L. S., Daniel Dapkus, P. & Nutt, S. R. “Vertical nonpolar growth templates for light emitting diodes formed with GaN nanosheets”. *Appl. Phys. Lett.* **100,** p. 033119 (2012).

103. Chi, C. Y., Chang, C. C., Hu, S., Yeh, T. W., Cronin, S. B. & Dapkus, P. D. “Twin-free GaAs nanosheets by selective area growth: Implications for defect-free nanostructures”. *Nano Lett.* **13,** p. 2506 (2013).

104. Marks, L. D. & Peng, L. “Nanoparticle shape, thermodynamics and kinetics”. *J. Phys. Condens. Matter* **28,** p. 053001 (2016).

105. Herring, C. “Konferenz über Struktur und Eigenschaften fester Oberflächen Lake. Geneva (Wisconsin) USA, 29. September bis 1. Oktober 1952”. *Angew. Chemie* **65,** p. 34 (1953).

106. Taylor, J. E. “Thermodynamic driving forces and anisotropic interface motion”. *JOM* **48,** p. 19 (1996).

107. Carter, W. C., Taylor, J. E. & Cahn, J. W. “Variational methods for microstructural-evolution theories”. *JOM* **49,** p. 30 (1997).

108. Frank, F. C. in *Growth Perfect. Cryst.* (ed Doremus R. H. Roberts B. W., T. D.) (John Wiley & Sons, New York, 1958).

109. Chernov, A. A. “The Kinetics of the Growth Forms of Crystals”. *Sov. Phys. Crystallogr.* **7,** p. 728 (1963).

110. Albani, M., Bergamaschini, R., Salvalaglio, M., Voigt, A., Miglio, L. & Montalenti, F. “Competition Between Kinetics and Thermodynamics During the Growth of Faceted Crystal by Phase Field Modeling”. *Phys. status solidi,* p. 1800518 (2019).

111. Jones, S. H., Siedel, L. K. & Lau, K. M. “Patterned substrate epitaxy surface shapes”. *J. Cryst. Growth* **108,** p. 73 (1991).

112. Stöcker, C & Voigt, A. “The effect of kinetics in the surface evolution of thin crystalline films”. *J. Cryst. Growth* **303,** p. 90 (2007).

113. Rätz, A., Ribalta, A. & Voigt, A. “Surface evolution of elastically stressed films under deposition by a diffuse interface model”. *J. Comput. Phys.* **214,** p. 187 (2006).

114. Bergamaschini, R., Salvalaglio, M., Backofen, R., Voigt, A. & Montalenti, F. “Continuum modelling of semiconductor heteroepitaxy: an applied perspective”. *Adv. Phys. X* **1,** p. 331 (2016).

115. Ohtsuka, M. & Suzuki, A. “Modeling of molecular-beam epitaxy and metalorganic vapor-phase epitaxy on nonplanar surfaces”. *J. Appl. Phys.* **73,** p. 7358 (1993).

116. Bergamaschini, R., Isa, F., Falub, C., Niedermann, P., Müller, E., Isella, G., von Känel, H. & Miglio, L. “Self-aligned Ge and SiGe three-dimensional epitaxy on dense Si pillar arrays”. *Surf. Sci. Rep.* **68,** p. 390 (2013).

117. Cermelli, P. & Jabbour, M. “Multispecies epitaxial growth on vicinal surfaces with chemical reactions and diffusion”. *Proc. R. Soc. A Math. Phys. Eng. Sci.* **461,** p. 3483 (2005).

118. Fried, E. & Gurtin, M. E. “The role of the configurational force balance in the nonequilibrium epitaxy of films”. *J. Mech. Phys. Solids* **51,** p. 487 (2003).

119. Hoffman, D. W. & Cahn, J. W. “A vector thermodynamics for anisotropic surfaces—I Fundamentals and application to plane surface junctions”. *Surf. Sci.* **31,** p. 368 (1972).

120. Cahn, J. W. & Hoffman, D. W. “A vector thermodynamics for anisotropic surface - II. curved and faceted surfaces”. *Acta Metall.* **22,** p. 1205 (1974).

121. Elliott, C. & Stuart, A. “Viscous Cahn–Hilliard Equation II. Analysis”. *J. Differ. Equ.* **128,** p. 387 (1996).

122. Gugenberger, C., Spatschek, R. & Kassner, K. “Comparison of phase-field models for surface diffusion”. *Phys. Rev. E* **78,** p. 016703 (2008).

123. Voigt, A. "Comment on "Degenerate mobilities in phase field models are insufficient to capture surface diffusion" [Appl. Phys. Lett. 107 , 081603 (2015)]". *Appl. Phys. Lett.* **108,** p. 036101 (2016).

124. Backofen, R., Wise, S. M., Salvalaglio, M. & Voigt, A. "Convexity splitting in a phase field model for surface diffusion". *Int. J. Numer. Anal. Model.* **1,** p. 1 (2017).

125. Torabi, S., Lowengrub, J., Voigt, A. & Wise, S. "A new phase-field model for strongly anisotropic systems". *Proc. R. Soc. A* **465,** p. 1337 (2009).

126. Spencer, B. J. "Asymptotic solutions for the equilibrium crystal shape with small corner energy regularization". *Phys. Rev. E* **69,** p. 11603 (2004).

127. Salvalaglio, M., Backofen, R., Bergamaschini, R., Montalenti, F. & Voigt, A. "Faceting of Equilibrium and Metastable Nanostructures: A Phase-Field Model of Surface Diffusion Tackling Realistic Shapes". *Cryst. Growth Des.* **15,** p. 2787 (2015).

128. Salvalaglio, M., Bergamaschini, R., Backofen, R., Voigt, A., Montalenti, F. & Miglio, L. "Phase-field simulations of faceted Ge/Si-crystal arrays, merging into a suspended film". *Appl. Surf. Sci.* **391,** p. 33 (2017).

129. Hawkeye, M. M. & Brett, M. J. "Glancing angle deposition: Fabrication, properties, and applications of micro- and nanostructured thin films". *J. Vac. Sci. Technol. A* **25,** p. 1317 (2007).

130. Barranco, A., Borras, A., Gonzalez-Elipe, A. R. & Palmero, A. "Perspectives on oblique angle deposition of thin films: From fundamentals to devices". *Prog. Mater. Sci.* **76,** p. 59 (2016).

131. Salvalaglio, M., Backofen, R. & Voigt, A. "Thin-film growth dynamics with shadowing effects by a phase-field approach". *Phys. Rev. B* **94,** p. 235432 (2016).

132. Lewis, R. B., Corfdir, P., Küpers, H., Flissikowski, T., Brandt, O. & Geelhaar, L. "Nanowires Bending over Backward from Strain Partitioning in Asymmetric Core–Shell Heterostructures". *Nano Lett.* **18,** p. 2343 (2018).

133. Falub, C. V. *et al.* "3D heteroepitaxy of mismatched semiconductors on silicon". *Thin Solid Films* **557,** p. 42 (2014).

134. Taboada, A. G. *et al.* "GaAs/Ge crystals grown on Si substrates patterned down to the micron scale". *J. Appl. Phys.* **119,** p. 055301 (2016).

135. Bergamaschini, R., Bietti, S., Castellano, A., Frigeri, C., Falub, C. V., Scaccabarozzi, A., Bollani, M., von Känel, H., Miglio, L. & Sanguinetti, S. "Kinetic growth mode of epitaxial GaAs on Si(001) micro-pillars". *J. Appl. Phys.* **120,** p. 245702 (2016).

136. Tomioka, K., Kobayashi, Y., Motohisa, J., Hara, S. & Fukui, T. "Selective-area growth of vertically aligned GaAs and GaAs/AlGaAs core–shell nanowires on Si(111) substrate". *Nanotechnology* **20,** p. 145302 (2009).

137. Bassett, K. P., Mohseni, P. K. & Li, X. "Evolution of GaAs nanowire geometry in selective area epitaxy". *Appl. Phys. Lett.* **106,** p. 133102 (2015).

138. Yang, Z., Surrente, A., Tutuncuoglu, G., Galkowski, K., Cazaban-Carrazé, M., Amaduzzi, F., Leroux, P., Maude, D. K., Fontcuberta i Morral, A. & Plochocka, P. “Revealing Large-Scale Homogeneity and Trace Impurity Sensitivity of GaAs Nanoscale Membranes”. *Nano Lett.* **17,** p. 2979 (2017).

139. Potts, H., van Hees, Y., Tütüncüoglu, G., Friedl, M., Leran, J.-B. & Fontcuberta i Morral, A. “Tilting Catalyst-Free InAs Nanowires by 3D-Twinning and Unusual Growth Directions”. *Cryst. Growth Des.* **17,** p. 3596 (2017).

140. Krizek, F. *et al.* “Field effect enhancement in buffered quantum nanowire networks”. *Phys. Rev. Mater.* **2,** p. 093401 (2018).

141. Moll, N., Kley, A., Pehlke, E. & Scheffler, M. “GaAs equilibrium crystal shape from first principles”. *Phys. Rev. B* **54,** p. 8844 (1996).

142. Albani, M., Ghisalberti, L., Bergamaschini, R., Friedl, M., Salvalaglio, M., Voigt, A., Montalenti, F., Tütüncüoglu, G., Fontcuberta i Morral, A. & Miglio, L. “Growth kinetics and morphological analysis of homoepitaxial GaAs fins by theory and experiment”. *Phys. Rev. Mater.* **2,** p. 093404 (2018).

143. Jiang, W., Bao, W., Thompson, C. V. & Srolovitz, D. J. “Phase field approach for simulating solid-state dewetting problems”. *Acta Mater.* **60,** p. 5578 (2012).

144. Tersoff, J., Johnson, M. D. & Orr, B. G. “Adatom Densities on GaAs: Evidence for Near-Equilibrium Growth”. *Phys. Rev. Lett.* **78,** p. 282 (1997).

145. Knoedler, M., Bologna, N., Schmid, H., Borg, M., Moselund, K. E., Wirths, S., Rossell, M. D. & Riel, H. “Observation of Twin-free GaAs Nanowire Growth Using Template-Assisted Selective Epitaxy”. *Cryst. Growth Des.* **17,** p. 6297 (2017).

146. Platen, J, Kley, A, Setzer, C, Jacobi, K, Ruggerone, P & Scheffler, M. “The importance of high-index surfaces for the morphology of GaAs quantum dots”. *J. Appl. Phys.* **85,** p. 3597 (1999).

147. Kojima, T., Kawai, N. J., Nakagawa, T., Ohta, K., Sakamoto, T. & Kawashima, M. “Layer-by-layer sublimation observed by reflection high-energy electron diffraction intensity oscillation in a molecular beam epitaxy system”. *Appl. Phys. Lett.* **47,** p. 286 (1985).

148. Márquez, J., Kratzer, P., Geelhaar, L., Jacobi, K. & Scheffler, M. “Atomic structure of the stoichiometric GaAs(114) surface”. *Phys. Rev. Lett.* **86,** p. 115 (2001).

149. Conesa-Boj, S., Boioli, F., Russo-Averchi, E., Dunand, S., Heiss, M., Rüffer, D., Wyrsch, N., Ballif, C., Miglio, L. & Morral, A. F. i. “Plastic and Elastic Strain Fields in GaAs/Si Core–Shell Nanowires”. *Nano Lett.* **14,** p. 1859 (2014).

150. Dayeh, S. A. *et al.* “Direct Measurement of Coherency Limits for Strain Relaxation in Heteroepitaxial Core/Shell Nanowires”. *Nano Lett.* **13,** p. 1869 (2013).

151. Liang, Y., Nix, W. D., Griffin, P. B. & Plummer, J. D. “Critical thickness enhancement of epitaxial SiGe films grown on small structures”. *J. Appl. Phys.* **97,** p. 043519 (2005).

152. Landau, L. D. & Lifshitz, E. M. *Theory of Elasticity* (Elsevier, 1986).

153. Eshelby, J. D. “The Determination of the Elastic Field of an Ellipsoidal Inclusion, and Related Problems”. *Proc. R. Soc. A Math. Phys. Eng. Sci.* **241,** p. 376 (1957).

154. Kittel, C. in *Introd. to Solid State Phys.* (ed John Wiley and Sons) 2005th ed., p. 73 (2005).

155. Martin, R. M. “Relation between Elastic Tensors of Wurtzite and Zinc-Blende Structure Materials”. *Phys. Rev. B* **6,** p. 4546 (1972).

156. Shih, H.-Y., Shiojiri, M., Chen, C.-H., Yu, S.-F., Ko, C.-T., Yang, J.-R., Lin, R.-M. & Chen, M.-J. “Ultralow threading dislocation density in GaN epilayer on near-strain-free GaN compliant buffer layer and its applications in hetero-epitaxial LEDs”. *Sci. Rep.* **5,** p. 13671 (2015).

157. Vainorius, N., Lehmann, S., Gustafsson, A., Samuelson, L., Dick, K. A. & Pistol, M.-E. “Wurtzite GaAs Quantum Wires: One-Dimensional Subband Formation”. *Nano Lett.* **16,** p. 2774 (2016).

158. Tatebayashi, J., Kako, S., Ho, J., Ota, Y., Iwamoto, S. & Arakawa, Y. “Room-temperature lasing in a single nanowire with quantum dots”. *Nat. Photonics* **9,** p. 501 (2015).

159. Yan, X., Fan, S., Zhang, X. & Ren, X. “Analysis of Critical Dimensions for Nanowire Core-Multishell Heterostructures”. *Nanoscale Res. Lett.* **10,** p. 389 (2015).

160. Gao, Q. *et al.* “Selective-area epitaxy of pure wurtzite InP nanowires: High quantum efficiency and room-temperature lasing”. *Nano Lett.* **14,** p. 5206 (2014).

161. Berg, A., Yazdi, S., Nowzari, A., Storm, K., Jain, V., Vainorius, N., Samuelson, L., Wagner, J. B. & Borgström, M. T. “Radial Nanowire Light-Emitting Diodes in the (Al x Ga 1– x) y In 1– y P Material System”. *Nano Lett.* **16,** p. 656 (2016).

162. Tomioka, K., Yoshimura, M. & Fukui, T. “A III-V nanowire channel on silicon for high-performance vertical transistors”. *Nature* **488,** p. 189 (2012).

163. Cui, Y., van Dam, D., Mann, S. A., van Hoof, N. J. J., van Veldhoven, P. J., Garnett, E. C., Bakkers, E. P. A. M. & Haverkort, J. E. M. “Boosting Solar Cell Photovoltage via Nanophotonic Engineering”. *Nano Lett.* **16,** p. 6467 (2016).

164. Van Dam, D., van Hoof, N. J. J. J., Cui, Y., Van Veldhoven, P. J., Bakkers, E. P. A. M. A. M., Gómez Rivas, J. & Haverkort, J. E. M. M. “High-Efficiency Nanowire Solar Cells with Omnidirectionally Enhanced Absorption Due to Self-Aligned Indium-Tin-Oxide Mie Scatterers”. *ACS Nano* **10,** p. 11414 (2016).

165. Mann, S. A., Oener, S. Z., Cavalli, A., Haverkort, J. E. M., Bakkers, E. P. A. M. & Garnett, E. C. “Quantifying losses and thermodynamic limits in nanophotonic solar cells”. *Nat. Nanotechnol.* **11,** p. 1071 (2016).

166. Standing, A., Assali, S., Gao, L., Verheijen, M. A., van Dam, D., Cui, Y., Notten, P. H. L., Haverkort, J. E. M. & Bakkers, E. P. A. M. “Efficient water reduction with gallium phosphide nanowires”. *Nat. Commun.* **6,** p. 7824 (2015).

167. Gazibegovic, S. *et al.* “Epitaxy of advanced nanowire quantum devices”. *Nature* **548,** p. 434 (2017).

168. Lewis, R. B., Nicolai, L., Küpers, H., Ramsteiner, M., Trampert, A. & Geelhaar, L. “Anomalous Strain Relaxation in Core–Shell Nanowire Heterostructures via Simultaneous Coherent and Incoherent Growth”. *Nano Lett.* **17,** p. 136 (2017).

169. Heiss, M. *et al.* “Self-assembled quantum dots in a nanowire system for quantum photonics”. *Nat. Mater.* **12,** p. 439 (2013).

170. Zhu, T. & Ertekin, E. “Generalized Debye-Peierls/Allen-Feldman model for the lattice thermal conductivity of low-dimensional and disordered materials”. *Phys. Rev. B* **93,** p. 155414 (2016).

171. Karbaschi, H., Lovén, J., Courteaut, K., Wacker, A. & Leijnse, M. “Nonlinear thermoelectric efficiency of superlattice-structured nanowires”. *Phys. Rev. B* **94,** p. 115414 (2016).

172. Wallentin, J., Jacobsson, D., Osterhoff, M., Borgström, M. T. & Salditt, T. “Bending and Twisting Lattice Tilt in Strained Core–Shell Nanowires Revealed by Nanofocused X-ray Diffraction”. *Nano Lett.* **17,** p. 4143 (2017).

173. Keplinger, M. *et al.* “Core–shell nanowires: From the ensemble to single-wire characterization”. *Nucl. Instruments Methods Phys. Res. Sect. B Beam Interact. with Mater. Atoms* **268,** p. 316 (2010).

174. Assali, S *et al.* “Direct Band Gap Wurtzite Gallium Phosphide Nanowires”. *Nano Lett.* **13,** p. 1559 (2013).

175. Gagliano, L., Albani, M., Verheijen, M. A., Bakkers, E. P. A. M. & Miglio, L. “Twofold origin of strain-induced bending in core–shell nanowires: the GaP/InGaP case”. *Nanotechnology* **29,** p. 315703 (2018).

176. Timoshenko, S. “LXVI. On the correction for shear of the differential equation for transverse vibrations of prismatic bars”. *London, Edinburgh, Dublin Philos. Mag. J. Sci.* **41,** p. 744 (1921).

177. Karparvarfard, S., Asghari, M. & Vatankhah, R. “A geometrically nonlinear beam model based on the second strain gradient theory”. *Int. J. Eng. Sci.* **91,** p. 63 (2015).

178. Mindlin, R. D. & Tiersten, H. F. “Effects of couple-stresses in linear elasticity”. *Arch. Ration. Mech. Anal.* **11,** p. 415 (1962).

179. Mindlin, R. “Second gradient of strain and surface-tension in linear elasticity”. *Int. J. Solids Struct.* **1,** p. 417 (1965).

180. Ferrand, D. & Cibert, J. “Strain in crystalline core-shell nanowires”. *Eur. Phys. J. Appl. Phys.* **67,** p. 30403 (2014).

181. Maranganti, R. & Sharma, P. “Length Scales at which Classical Elasticity Breaks Down for Various Materials”. *Phys. Rev. Lett.* **98,** p. 195504 (2007).

182. Denton, A. R. & Ashcroft, N. W. “Vegard’s law”. *Phys. Rev. A* **43,** p. 3161 (1991).

183. Kriegner, D, Wintersberger, E, Kawaguchi, K, Wallentin, J, Borgström, M. T. & Stangl, J. "Unit cell parameters of wurtzite InP nanowires determined by x-ray diffraction". *Nanotechnology* **22,** p. 425704 (2011).

184. Kriegner, D., Assali, S., Belabbes, A., Etzelstorfer, T., Holý, V., Schülli, T., Bechstedt, F., Bakkers, E. P. A. M., Bauer, G. & Stangl, J. "Unit cell structure of the wurtzite phase of GaP nanowires: X-ray diffraction studies and density functional theory calculations". *Phys. Rev. B* **88,** p. 115315 (2013).

185. Wang, S. Q. & Ye, H. Q. "First-principles study on elastic properties and phase stability of III–V compounds". *Phys. status solidi* **240,** p. 45 (2003).

186. Wirths, S., Buca, D. & Mantl, S. "Si–Ge–Sn alloys: From growth to applications". *Prog. Cryst. Growth Charact. Mater.* **62,** p. 1 (2016).

187. Wirths, S. *et al.* "Lasing in direct-bandgap GeSn alloy grown on Si". *Nat. Photonics* **9,** p. 88 (2015).

188. Soref, R., Buca, D. & Yu, S.-Q. "Group IV Photonics: Driving Integrated Optoelectronics". *Opt. Photonics News* **27,** p. 32 (2016).

189. Paniccia, M. "Integrating silicon photonics". *Nat. Photonics* **4,** p. 498 (2010).

190. Moontragoon, P., Soref, R. A. & Ikonic, Z. "The direct and indirect bandgaps of unstrained Si x Ge 1-x-y Sn y and their photonic device applications". *J. Appl. Phys.* **112,** p. 073106 (2012).

191. Von den Driesch, N. *et al.* "Direct Bandgap Group IV Epitaxy on Si for Laser Applications". *Chem. Mater.* **27,** p. 4693 (2015).

192. Takeuchi, S., Sakai, A., Yamamoto, K., Nakatsuka, O., Ogawa, M. & Zaima, S. "Growth and structure evaluation of strain-relaxed Ge 1- x Sn x buffer layers grown on various types of substrates". *Semicond. Sci. Technol.* **22,** S231 (2007).

193. Attiaoui, A. & Moutanabbir, O. "Indirect-to-direct band gap transition in relaxed and strained Ge 1-x-y Si x Sn y ternary alloys". *J. Appl. Phys.* **116,** p. 063712 (2014).

194. Soref, R. "Mid-infrared photonics in silicon and germanium". *Nat. Photonics* **4,** p. 495 (2010).

195. Olesinski, R. W. & Abbaschian, G. J. "The Ge-Sn (Germanium-Tin) system". *Bull. Alloy Phase Diagrams* **5,** p. 265 (1984).

196. He, G. & Atwater, H. A. "Synthesis of epitaxial Sn x Ge 1- x alloy films by ion-assisted molecular beam epitaxy". *Appl. Phys. Lett.* **68,** p. 664 (1996).

197. Takeuchi, S., Sakai, A., Nakatsuka, O., Ogawa, M. & Zaima, S. "Tensile strained Ge layers on strain-relaxed Ge1-xSnx/virtual Ge substrates". *Thin Solid Films* **517,** p. 159 (2008).

198. Wirths, S., Buca, D., Mussler, G., Tiedemann, A. T., Hollander, B., Bernardy, P., Stoica, T., Grutzmacher, D. & Mantl, S. "Reduced Pressure CVD Growth of Ge and Ge1-xSnx Alloys". *ECS J. Solid State Sci. Technol.* **2,** N99 (2013).

199. Biswas, S., Doherty, J., Saladukha, D., Ramasse, Q., Majumdar, D., Upmanyu, M., Singha, A., Ochalski, T., Morris, M. A. & Holmes, J. D. "Non-equilibrium induction of tin in germanium: towards direct bandgap Ge1-xSnx nanowires". *Nat. Commun.* **7,** p. 11405 (2016).

200. Aubin, J., Hartmann, J. M., Gassenq, A., Milord, L., Pauc, N., Reboud, V. & Calvo, V. "Impact of thickness on the structural properties of high tin content GeSn layers". *J. Cryst. Growth* **473,** p. 20 (2017).

201. Lin, H. Y., Chen, Y. F., Lin, T. Y., Shih, C. F., Liu, K. S. & Chen, N. C. "Direct evidence of compositional pulling effect in AlxGa1-xN epilayers". *J. Cryst. Growth* **290,** p. 225 (2006).

202. Margetis, J. *et al.* "Study of low-defect and strain-relaxed GeSn growth via reduced pressure CVD in H 2 and N 2 carrier gas". *J. Cryst. Growth* **463,** p. 128 (2017).

203. Aubin, J., Hartmann, J. M., Gassenq, A, Rouviere, J. L., Robin, E, Delaye, V, Cooper, D, Mollard, N, Reboud, V & Calvo, V. "Growth and structural properties of step-graded, high Sn content GeSn layers on Ge". *Semicond. Sci. Technol.* **32,** p. 94006 (2017).

204. Assali, S. *et al.* "Growth and Optical Properties of Direct Band Gap Ge/Ge 0.87 Sn 0.13 Core/Shell Nanowire Arrays". *Nano Lett.* **17,** p. 1538 (2017).

205. Meng, A. C., Fenrich, C. S., Braun, M. R., McVittie, J. P., Marshall, A. F., Harris, J. S. & McIntyre, P. C. "Core-Shell Germanium/Germanium–Tin Nanowires Exhibiting Room-Temperature Direct- and Indirect-Gap Photoluminescence". *Nano Lett.* **16,** p. 7521 (2016).

206. Margetis, J., Yu, S.-Q., Bhargava, N., Li, B., Du, W. & Tolle, J. "Strain engineering in epitaxial Ge 1- x Sn x : a path towards low-defect and high Sn-content layers". *Semicond. Sci. Technol.* **32,** p. 124006 (2017).

207. Fleurial, J. P. "Si-Ge-Metal Ternary Phase Diagram Calculations". *J. Electrochem. Soc.* **137,** p. 2928 (1990).

208. Albani, M., Assali, S., Verheijen, M. A., Koelling, S., Bergamaschini, R., Pezzoli, F., Bakkers, E. P. A. M. & Miglio, L. "Critical strain for Sn incorporation into spontaneously graded Ge/GeSn core/shell nanowires". *Nanoscale* **10,** p. 7250 (2018).

209. Takeda, M. & Suzuki, J. "Crystallographic heterodyne phase detection for highly sensitive lattice-distortion measurements". *J. Opt. Soc. Am. A* **13,** p. 1495 (1996).

210. Hÿtch, M. J., Snoeck, E. & Kilaas, R. "Quantitative measurement of displacement and strain fields from HREM micrographs". *Ultramicroscopy* **74,** p. 131 (1998).

211. Gencarelli, F. *et al.* "Crystalline Properties and Strain Relaxation Mechanism of CVD Grown GeSn". *ECS J. Solid State Sci. Technol.* **2,** P134 (2013).

212. Dou, W. *et al.* "Investigation of GeSn Strain Relaxation and Spontaneous Composition Gradient for Low-Defect and High-Sn Alloy Growth". *Sci. Rep.* **8,** p. 5640 (2018).

213. Mo, Y.-W., Savage, D. E., Swartzentruber, B. S. & Lagally, M. G. "Kinetic pathway in Stranski-Krastanov growth of Ge on Si(001)". *Phys. Rev. Lett.* **65,** p. 1020 (1990).

214. Eaglesham, D. J. & Cerullo, M. "Dislocation-free Stranski-Krastanow growth of Ge on Si(100)". *Phys. Rev. Lett.* **64,** p. 1943 (1990).

215. Leonard, D, Pond, K. & Petroff, P. M. "Critical layer thickness for self-assembled InAs islands on GaAs". *Phys. Rev. B* **50,** p. 11687 (1994).

216. Tersoff, J., Spencer, B. J., Rastelli, A. & von Känel, H. "Barrierless Formation and Faceting of SiGe Islands on Si(001)". *Phys. Rev. Lett.* **89,** p. 196104 (2002).

217. Chiu, C. H. & Gao, H. J. "A numerical study of stress controlled surface diffusion during epitaxial film growth". *Mater. Res. Soc. Symp. Proc.* **356** (ed Baker, SP and Ross, CA and Townsend, PH and Volkert, CA and Borgesen, P) p. 33 (1995).

218. Spencer, B. J. "Asymptotic derivation of the glued-wetting-layer model and contact-angle condition for Stranski-Krastanow islands". *Phys. Rev. B* **59,** p. 2011 (1999).

219. Levine, M. S., Golovin, A. A., Davis, S. H. & Voorhees, P. W. "Self-assembly of quantum dots in a thin epitaxial film wetting an elastic substrate". *Phys. Rev. B* **75,** p. 205312 (2007).

220. Aqua, J.-N., Frisch, T. & Verga, A. "Nonlinear evolution of a morphological instability in a strained epitaxial film". *Phys. Rev. B* **76,** p. 165319 (2007).

221. Takaki, T., Hasebe, T. & Tomita, Y. "Two-dimensional phase-field simulation of self-assembled quantum dot formation". *J. Cryst. Growth* **287,** p. 495 (2006).

222. Spencer, B. J., Voorhees, P. W. & Tersoff, J. "Enhanced Instability of Strained Alloy Films due to Compositional Stresses". *Phys. Rev. Lett.* **84,** p. 2449 (2000).

223. Tu, Y. & Tersoff, J. "Origin of Apparent Critical Thickness for Island Formation in Heteroepitaxy". *Phys. Rev. Lett.* **93,** p. 216101 (2004).

224. Tu, Y. & Tersoff, J. "Coarsening, Mixing, and Motion: The Complex Evolution of Epitaxial Islands". *Phys. Rev. Lett.* **98,** p. 096103 (2007).

225. Bergamaschini, R, Tersoff, J, Tu, Y, Zhang, J. J., Bauer, G & Montalenti, F. "Anomalous Smoothing Preceding Island Formation During Growth on Patterned Substrates". *Phys. Rev. Lett.* **109,** p. 156101 (2012).

226. Jonsdottir, F & Freund, L. "Equilibrium surface roughness of a strained epitaxial film due to surface diffusion induced by interface misfit dislocations". *Mech. Mater.* **20,** p. 337 (1995).

227. Zhang, J. J., Rastelli, A., Groiss, H., Tersoff, J., Schaffler, F., Schmidt, O. G. & Bauer, G. "Shaping site-controlled uniform arrays of SiGe/Si(001) islands by in situ annealing". *Appl. Phys. Lett.* **95,** p. 183102 (2009).

228. Lausecker, E, Brehm, M., Grydlik, M., Hackl, F., Bergmair, I, Muhlberger, M., Fromherz, T., Schaffler, F. & Bauer, G. "UV nanoimprint lithography for the realization of large-area ordered SiGe/Si(001) island arrays". *Appl. Phys. Lett.* **98,** p. 143101 (2011).

229. Biasiol, G. & Kapon, E. “Mechanisms of Self-Ordering of Quantum Nanostructures Grown on Nonplanar Surfaces”. *Phys. Rev. Lett.* **81,** p. 2962 (1998).

230. Zhong, Z., Halilovic, A, Mühlberger, M, Schäffler, F. & Bauer, G. “Ge island formation on stripe-patterned Si(001) substrates”. *Appl. Phys. Lett.* **82,** p. 445 (2003).

231. Pascale, A, Berbezier, I, Ronda, A & Kelires, P. C. “Self-assembly and ordering mechanisms of Ge islands on prepatterned Si(001)”. *Phys. Rev. B* **77,** p. 075311 (2008).

232. Grydlik, M., Brehm, M., Hackl, F., Groiss, H., Fromherz, T., Schäffler, F. & Bauer, G. “Inverted Ge islands in (111) faceted Si pits—a novel approach towards SiGe islands with higher aspect ratio”. *New J. Phys.* **12,** p. 063002 (2010).

233. Grydlik, M., Brehm, M., Hackl, F., Schäffler, F., Bauer, G. & Fromherz, T. “Unrolling the evolution kinetics of ordered SiGe islands via Ge surface diffusion”. *Phys. Rev. B* **88,** p. 115311 (2013).

234. Bergamaschini, R., Montalenti, F. & Miglio, L. “Optimal Growth Conditions for Selective Ge Islands Positioning on Pit-Patterned Si(001)”. *Nanoscale Res. Lett.* **5,** p. 1873 (2010).

235. Vastola, G., Shenoy, V. B., Guo, J & Zhang, Y.-W. “Coupled evolution of composition and morphology in a faceted three-dimensional quantum dot”. *Phys. Rev. B* **84,** p. 035432 (2011).

236. Liu, P, Lu, C & Zhang, Y.-W. “Formation of surface structures during heteroepitaxial thin film growth on prepatterned substrates”. *Phys. Rev. B* **76,** p. 085336 (2007).

237. Wang, H., Zhang, Y. & Liu, F. “Enhanced growth instability of strained film on wavy substrate”. *J. Appl. Phys.* **104,** p. 054301 (2008).

238. Kassner, K., Misbah, C., Müller, J., Kappey, J. & Kohlert, P. “Phase-field modeling of stress-induced instabilities”. *Phys. Rev. E* **63,** p. 036117 (2001).

239. Wang, Y. U., Jin, Y. M. & Khachaturyan, A. G. “Phase field microelasticity modeling of surface instability of heteroepitaxial thin films”. *Acta Mater.* **52,** p. 81 (2004).

240. Rodney, D., Le Bouar, Y. & Finel, A. “Phase field methods and dislocations”. *Acta Mater.* **51,** p. 17 (2003).

241. Le Bouar, Y., Loiseau, A. & Khachaturyan, A. “Origin of chessboard-like structures in decomposing alloys. Theoretical model and computer simulation”. *Acta Mater.* **46,** p. 2777 (1998).

242. Wang, L. G., Kratzer, P, Scheffler, M & Moll, N. “Formation and Stability of Self-Assembled Coherent Islands in Highly Mismatched Heteroepitaxy”. *Phys. Rev. Lett.* **82,** p. 4042 (1999).

243. Eggleston, J. J. & Voorhees, P. W. “Ordered growth of nanocrystals via a morphological instability”. *Appl. Phys. Lett.* **80,** p. 306 (2002).

244. Seol, D. J., Hu, S. Y., Liu, Z. K., Chen, L. Q., Kim, S. G. & Oh, K. H. "Phase-field modeling of stress-induced surface instabilities in heteroepitaxial thin films". *J. Appl. Phys.* **98,** p. 044910 (2005).

245. Albani, M., Bergamaschini, R. & Montalenti, F. "Dynamics of pit filling in heteroepitaxy via phase-field simulations". *Phys. Rev. B* **94,** p. 075303 (2016).

246. Huang, L., Liu, F., Lu, G.-H. & Gong, X. G. "Surface Mobility Difference between Si and Ge and Its Effect on Growth of SiGe Alloy Films and Islands". *Phys. Rev. Lett.* **96,** p. 016103 (2006).

247. Capellini, G., De Seta, M. & Evangelisti, F. "SiGe intermixing in Ge/Si(100) islands". *Appl. Phys. Lett.* **78,** p. 303 (2001).

248. Backofen, R., Bergamaschini, R. & Voigt, A. "The interplay of morphological and compositional evolution in crystal growth: a phase-field model". *Philos. Mag.* **94,** p. 2162 (2014).

249. Onsager, L. "Reciprocal Relations in Irreversible Processes I." *Phys. Rev.* **37,** p. 405 (1931).

250. Onsager, L. "Reciprocal Relations in Irreversible processes. II". *Phys. Rev.* **38,** p. 2265 (1931).

251. Aqua, J.-N., Favre, L., Ronda, A., Benkouider, A. & Berbezier, I. "Configurable Compliant Substrates for SiGe Nanomembrane Fabrication". *Cryst. Growth Des.* **15,** p. 3399 (2015).

252. Lu, G.-H., Cuma, M. & Liu, F. "First-principles study of strain stabilization of Ge(105) facet on Si(001)". *Phys. Rev. B* **72,** p. 125415 (2005).

253. Lu, G.-H. & Liu, F. "Towards Quantitative Understanding of Formation and Stability of Ge Hut Islands on Si(001)". *Phys. Rev. Lett.* **94,** p. 176103 (2005).

254. Pang, Y. & Huang, R. "Nonlinear effect of stress and wetting on surface evolution of epitaxial thin films". *Phys. Rev. B* **74,** p. 075413 (2006).

255. Jesson, D. E., Pennycook, S. J., Baribeau, J. M. & Houghton, D. C. "Direct imaging of surface cusp evolution during strained-layer epitaxy and implications for strain relaxation". *Phys. Rev. Lett.* **71,** p. 1744 (1993).

256. Brehm, M. *et al.* "Key role of the wetting layer in revealing the hidden path of Ge/Si(001) Stranski-Krastanow growth onset". *Phys. Rev. B* **80,** p. 205321 (2009).

257. Aqua, J.-N., Frisch, T. & Verga, A. "Ordering of strained islands during surface growth". *Phys. Rev. E* **81,** p. 021605 (2010).

258. Spencer, B. J., Voorhees, P. W. & Davis, S. H. "Morphological Instability in Epitaxially Strained Dislocation-Free Solid Films". *Phys. Rev. Lett.* **67,** p. 3696 (1991).

259. Godbey, D. J., Lill, J. V., Deppe, J. & Hobart, K. D. "Ge surface segregation at low temperature during SiGe growth by molecular beam epitaxy". *Appl. Phys. Lett.* **65,** p. 711 (1994).

260. Kukta, R. & Freund, L. "Minimum energy configuration of epitaxial material clusters on a lattice-mismatched substrate". *J. Mech. Phys. Solids* **45,** p. 1835 (1997).

261. Asai, M., Ueba, H. & Tatsuyama, C. "Heteroepitaxial growth of Ge films on the Si(100)-2×1 surface". *J. Appl. Phys.* **58,** p. 2577 (1985).

262. Kukta, R. V. & Kouris, D. "On the mechanisms of epitaxial island alignment on patterned substrates". *J. Appl. Phys.* **97,** p. 033527 (2005).

263. Cheng-Hsin, C. & Huajian, G. "Stress singularities along a cycloid rough surface". *Int. J. Solids Struct.* **30,** p. 2983 (1993).

264. Gao, H. & Nix, W. D. "SURFACE ROUGHENING OF HETEROEPITAXIAL THIN FILMS". *Annu. Rev. Mater. Sci.* **29,** p. 173 (1999).

265. Aqua, J.-N. & Xu, X. "Growth of quantum dots on pit-patterns". *Surf. Sci.* **639,** p. 20 (2015).

266. Hu, H., Gao, H. & Liu, F. "Quantitative Model of Heterogeneous Nucleation and Growth of SiGe Quantum Dot Molecules". *Phys. Rev. Lett.* **109,** p. 106103 (2012).

267. Wang, S., Zhou, T., Li, D. & Zhong, Z. "Evolution and Engineering of Precisely Controlled Ge Nanostructures on Scalable Array of Ordered Si Nano-pillars". *Sci. Rep.* **6,** p. 28872 (2016).

268. Liu, F., Huang, M., Rugheimer, P. P., Savage, D. E. & Lagally, M. G. "Nanostressors and the Nanomechanical Response of a Thin Silicon Film on an Insulator". *Phys. Rev. Lett.* **89,** p. 136101 (2002).

269. Hartmann, A., Dieker, C., Loo, R., Vescan, L., Lüth, H. & Bangert, U. "Photoluminescence and microstructure of self-ordered grown SiGe/Si quantum wires". *Appl. Phys. Lett.* **67,** p. 1888 (1995).

270. Xie, Y. H., Samavedam, S. B., Bulsara, M., Langdo, T. A. & Fitzgerald, E. A. "Relaxed template for fabricating regularly distributed quantum dot arrays". *Appl. Phys. Lett.* **71,** p. 3567 (1997).

271. Capellini, G., De Seta, M., Spinella, C. & Evangelisti, F. "Ordering self-assembled islands without substrate patterning". *Appl. Phys. Lett.* **82,** p. 1772 (2003).

272. Endres, J., Holý, V., Daniš, S. & Buljan, M. "Kinetic Monte Carlo simulation of growth of Ge quantum dot multilayers with amorphous matrix". *J. Nanoparticle Res.* **19,** p. 135 (2017).

273. Liu, P, Zhang, Y.-W. & Lu, C. "Coarsening kinetics of heteroepitaxial islands in nucleationless Stranski-Krastanov growth". *Phys. Rev. B* **68,** p. 035402 (2003).

274. Latini, V., Placidi, E., Arciprete, F., Tisbi, E., Patella, F. & Magri, R. "Stress-determined nucleation sites above GaAs-capped arrays of InAs quantum dots". *J. Appl. Phys.* **120,** p. 125704 (2016).

275. Liang, X. D., Ni, Y & He, L. H. "Shape-dependent composition profile in epitaxial alloy quantum dots: A phase-field simulation". *Comput. Mater. Sci.* **48,** p. 871 (2010).